

# Investigations on Transport and Storage of High Ion Beam Intensities

Dissertation zur Erlangung des Doktorgrades der  
Naturwissenschaften

vorgelegt beim Fachbereich Physik  
der Johann Wolfgang Goethe-Universität  
in Frankfurt am Main von

Ninad Shrikrishna Joshi  
geboren in Mumbai, Indien

Frankfurt am Main, 2009  
D30

Vom Fachbereich Physik der  
Johann Wolfgang Goethe-Universität als Dissertationen angenommen

Dekan: Prof. Dr. D.-H. Rischke  
Erster Gutachter: Prof. Dr. U. Ratzinger  
Zweiter Gutachter: Prof. Dr. A. Schempp

# Zusammenfassung

Gegenstand der vorliegenden Arbeit war die Untersuchung des Transports intensiver Ionenstrahlen in toroidalen Magnetfeldern und die Injektion von geladenen Teilchenstrahlen in stellaratorähnliche Ringe.

Ein Speicherring mit einem toroidalen Magnetfeld wurde für die Akkumulation von intensiven Ionenstrahlen vorgeschlagen. Die Konfiguration ist ähnlich, wie bei den klassischen Stellaratoren, bei denen Toroidsegmente zu einem Torus angeordnet werden, um geladene Teilchen einzuschließen. Die sich daraus ergebenden longitudinalen Magnetfelder ermöglichen aber auch die Fokussierung eines in solch einer Apparatur eingeschlossenen Ionenstrahls. Die magnetischen Feldlinien in diesem System sind nicht einfach geschlossen, sondern bilden magnetische Flächen. Der Transport von Ionenstrahlen ist stark durch die transversalen Driften aufgrund der gebogenen Feldlinien beeinflusst, den diese führen zu einer Änderung der Strahlablage und können zu Verlusten an der Wand der Vakuumkammer führen. Die Ursache für die genannte Drift ist die Zentrifugalkraft, das bedeutet, dass die Drift in Abhängigkeit vom Kreuzprodukt  $\mathbf{R} \times \mathbf{B}$  von der Richtung des magnetischen Feldes bestimmt ist. Durch eine Verdrillung des magnetischen Torus zu einer so genannten *Figure – 8*-Geometrie, wie sie in Abbildung 1 dargestellt ist, wird eine Kompensation dieser Drift erreicht.

Durch diese Konfiguration ergibt sich auch eine Rotationstransformation der Magnetfeldlinien in poloidaler Richtung, die für einen stabilen Einschluss eines quasineutralen Plasmas essentiell ist. Deshalb wurde diese Konfiguration bei den Stellaratoren der frühen 60iger Jahre untersucht. Der Unterschied zwischen einem klassischen Stellarator und dem in dieser Arbeit vorgestellten Speicherringkonzept liegt aber vor allem in der gespeicherten Energie. Während beim Einschluss eines Plasmas Elektronenströme von einigen Kilo- bis Megaampere fließen, wird der Ionenstrom beim Einschluss von Ionenstrahlen bei einer Größenordnung von einigen Ampere liegen. Der vorgeschlagene Speicherring wird auf vielfältige Weise Konzepte der Plasmaphysik mit denen der Beschleunigerphysik kombinieren und dabei Beiträge auf dem Gebiet der nichtneutralen Plasmen und der so genannten Moving - Plasmas leisten können. Um den Zusammenhang zwischen diesen verschiedenen Disziplinen zu unterstreichen wurde die Terminologie aus beiden Bereichen verwendet, um die Ergebnisse der numerischen Simulationen und die experimentellen Befunde zu diskutieren.

Für die numerischen Simulationen des Strahltransports wurde ein Computermodell entwickelt, das die Teilchenbewegung in inhomogenen Magnetfeldern berechnet. Dieser "Particle in Cell" - Code (PIC) ermöglicht die Untersuchung einer Multiteilchendynamik und eignet sich dazu, verschiedene Modellverteilungen, z.B. KV - oder Gauß - Verteilungen, als Startverteilung zu generieren. Es ist aber auch möglich, die aus Messungen gewonnenen Teilchenverteilungen in das Programm einzulesen. Die Berechnung des Strahltransports kann auf verschiedenen Arten von numerischen Gittern erfolgen, nämlich auf kartesischen, zylindrischen

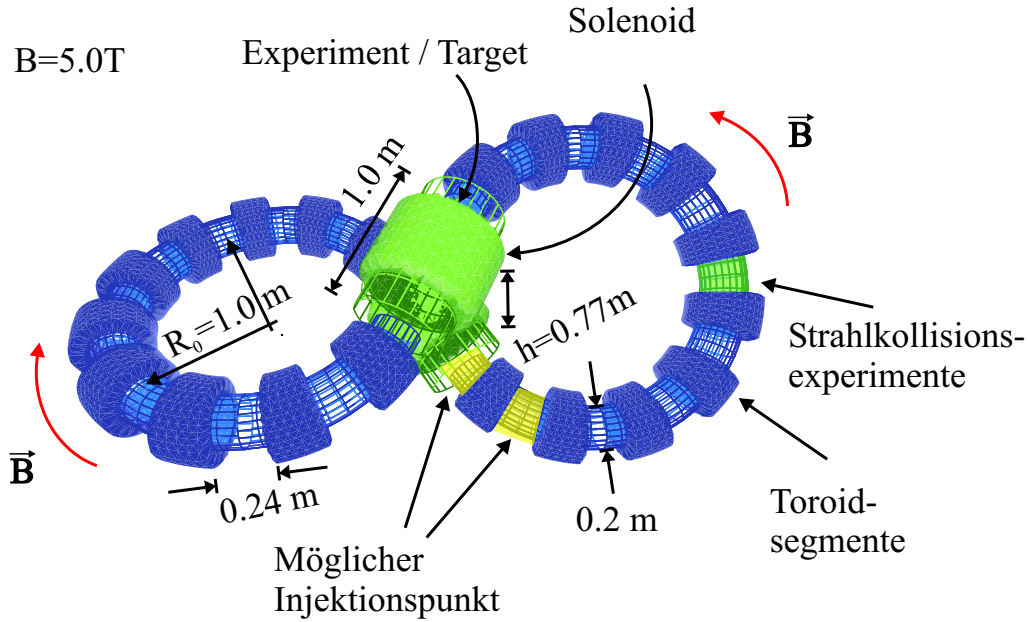


Figure 1: Darstellung des geplanten Hochstromspeicherrings mit toroidalen segmenten. Gelb: Injektion, Grün: Experimental bereich.

und toroidalen Gittern. Für die Berechnung der Raumladungskräfte wurde die Poisson-Gleichung auf dem toroidalen Gitter diskretisiert und die für die Lösung erforderliche Ladungsträgerdichte mit Hilfe der "Cloud in Cell"-Methode zweiter Ordnung an jedem Gitterpunkt bestimmt. Zunächst wurde untersucht, welche Methode sich für die Lösung der Poisson-Gleichung hinsichtlich der Rechenzeit und der Flexibilität gegenüber den zu variierenden Randbedingungen eignet. Im Falle der Berechnungen auf dem kartesischen Gitter wurde die Fast-Fourier-Methode verwendet, bei der die Randbedingungen so gesetzt werden müssen, dass Spiegelladungen an den Strahlrohrwänden berücksichtigt werden. Gerade bei umfangreichen Simulationen in großen Volumina ist die FFT-Methode aber zu ineffizient. Die Explizite-Matrix-Methode hingegen ist sehr flexibel und ermöglicht eine einfache Definition fester Potentiale an gewünschten Punkten. Es erfolgt dann die iterative Lösung einer Matrix, die ein System aus  $N_g$  unbekannt linearen Gleichungen beschreibt.  $N_g$  steht hierbei für die Anzahl der Gitterpunkte, die zwischen 70.000 und einer Million liegen kann. Für diese Methode wurden verschiedene iterative Verfahren untersucht und optimiert. Die externen magnetischen Felder, wie zum Beispiel das Feld der Toroidsegmente, wurden mit Hilfe eines Biot-Savart-Solvers bestimmt, mit dem es möglich ist die realen Feldverteilungen inklusive der in dieser Arbeit nicht zu vernachlässigenden Randfelder zu berechnen. Ein Vergleich der analytisch bestimmten Einzelteilchendynamik mit den numerischen Resultaten ergab eine Abweichung bei der Drift- und Gyrobewegung von  $\pm 0,17\%$ . Für die Charakterisierung des Strahltransports entlang gekrümmter magnetischer Feldlinien wurde der Strahlparameter  $v_\lambda$  (verhältnis von transversalen zu longitudinalen impuls bezugen auf die lage der magnetischer Feldlinie) eingeführt, der ein Indikator für die Transmission des Strahles durch das magnetische System ist. Aus den Ergebnissen der numerischen Simulationen hinsichtlich der Transmission lässt sich

die Akzeptanz der Toroidsegmente bezüglich der Strahlparameter ableiten, insbesondere auch unter Berücksichtigung des durch die Raumladung verursachten Eigenfeldes.

Neben den umfangreichen Arbeiten zur numerischen Simulation des Strahltransportes wurden auch Experimente durchgeführt, um das entwickelte Computermodell zu evaluieren und praktische Erfahrungen bei der Konstruktion und dem Aufbau eines toroidalen Speicherringes zu sammeln. Das für die Experimente verwendete Toroidsegment entspricht hinsichtlich seiner Geometrie etwa den Segmenten, die für den geplanten Speicherring vorgesehen sind. Während es sich später jedoch um supraleitende Magneten handeln wird, die eine Feldstärke von bis zu  $5 T$  erzeugen können, kann das für die Experimente ausgelegte Toroidsegment bei Raumtemperatur betrieben werden und erreicht eine magnetische Feldstärke von  $0,6T$  auf der magnetischen Achse. Durch den Vergleich der experimentellen Befunde mit den Ergebnissen der numerischen Simulation kann eine Skalierung auf die zu erwartenden Strahleigenschaften in dem zukünftigen Speicherring erfolgen. Ein erster Schritt war hierbei, eine Ionenquelle auf ihre Eignung hin zu untersuchen einen Ionenstrahl zu erzeugen, der sich durch eine sehr gute Strahlqualität auszeichnet und dessen Intensität das Studium von Raumladungseffekten ermöglicht. Für diese Untersuchungen wurde ein Experiment aufgebaut, mit dem es möglich war, die Strahlemittanz, den Strahlstrom und die Strahlzusammensetzung zu bestimmen. Die verwendete Ionenquelle ist einfach im Aufbau und sehr zuverlässig im Betrieb, insbesondere zeichnet sie sich durch eine sehr kleine Strahlemittanz und einen stabilen Betrieb aus, so dass ein maximaler Protonenanteil von  $48\%$  bei den Experimenten tolerierbar war. Die Strahlzusammensetzung lässt sich bei dem verwendeten Quellentyp über die Plasmaparameter steuern, so dass sich auch Strahlen, die zu  $80 - 90\%$  aus  $H_2^+$  oder  $H_3^+$  bestehen, extrahieren lassen. Die Strahlenergie konnte zwischen  $3 - 20 keV$  variiert werden. Bei allen Experimenten wurde ein  $He^+$  - Strahl als Referenz benutzt, da dieser ausschließlich aus einfach positiv geladenen Heliumionen zusammengesetzt ist. Es entstand im Rahmen dieser Doktorarbeit eine Veröffentlichung zu einer für die Strahltherapie interessanten Quelle, welche mit hoher Effizienz  $H_3^+$ -Strahlen erzeugt.

Die Anpassung des aus der Ionenquelle extrahierten Ionenstrahles an die Toroidsegmente erfolgte mit Hilfe eines Solenoiden. Deshalb wurden zunächst die Abbildungseigenschaften bei einer Variation der Strahlsteifigkeit und der magnetischen Feldstärke untersucht. Parallel zu den Experimenten wurden numerische Simulationen durchgeführt und mit den Messergebnissen verglichen. Es konnte gezeigt werden, dass die experimentellen und numerischen Resultate bis auf einen Fehler von  $1,7\%$  übereinstimmen. Dies war eine gute Voraussetzung um die Phasenraumverteilung am Injektionspunkt hinsichtlich des Transports durch das Toroidsegment zu optimieren und die gewonnenen Startverteilungen als Grundlage für die weiteren numerischen Untersuchungen mit dem Computerprogramm TBT zu verwenden.

Ein Schwerpunkt bei den Strahltransportexperimenten durch das Toroidsegment stellte die Strahldiagnose dar, mit deren Hilfe die Abbildungs- und Transporteigenschaften bestimmt werden sollten. Die Verwendung einer klassischen Schlitz-Gitter-Emittanzmessanlage wurde zum einen durch die maximal detektierbaren transversalen Impulse von  $120 mrad$  limitiert und durch das vorhandene Randfeld des Toroidsegmentes kam es zu einer prinzipiellen Schwierigkeit bei der Interpretation der Messsignale. Trotzdem konnten für wenige spezielle Setups verwertbare Messergebnisse gewonnen werden, die im direkten Vergleich mit den

numerischen Ergebnissen und Resultaten aus einem optischen Diagnoseverfahren dargestellt werden konnten. Bei der optischen Diagnose wurde ein *P20* Phosphorzintillator benutzt, um die Strahlprofile am Ausgang des Toroidsegmentes zu detektieren. Die maximale Konversionseffizienz liegt bei einer Lichtwellenlänge von  $500\text{ nm}$ , trotzdem war der Einsatz einer Digitalkamera durch das starke magnetische Randfeld nur bedingt möglich. Mit Hilfe einer magnetischen Abschirmung und unter Verwendung einer bezüglich der Elektronik sehr einfach aufgebauten Kamera war es möglich, optische Strahlprofile zu vermessen und die Lage des Ionenstrahles bezüglich der geometrischen Achse des experimentellen Aufbaus zu bestimmen. Aus den gewonnen Datensätzen konnten so die vertikalen und horizontalen Driften des Strahles und der Strahlradius bestimmt werden. Diese Parameter sind direkt vergleichbar mit denen des numerischen Modells. Allerdings ist eine Interpretation bei der Verwendung des Protonenstrahles sehr schwierig, weil sich die einzelnen Fraktionen bei der Detektion überlagern können. Aus diesem Grund wurde bei den Transportexperimenten wieder der Heliumionenstrahl als Referenz verwendet. Außerdem war es möglich, aus der verwendeten Ionenquelle einen reinen Elektronenstrahl zu extrahieren. Wegen der um einen Faktor 1836 geringeren Masse war eine Drift des Elektronenstrahles praktisch nicht nachweisbar, so dass sich aus der Lage des Strahlschwerpunktes auf die Lage der magnetischen Achse des Systems schließen ließ. Dieser Umstand führte dazu, dass die Achsen der Ionenstrahlen bezüglich dieser magnetischen Achse verglichen und so die exakten vertikalen und horizontalen Driften ermittelt werden konnten.

Entlang des Transportkanals durch das Toroidsegment wurden vom Ionenstrahl Sekundärelektronen erzeugt, die auch mit dem Diagnosesystem untersucht werden konnten. So konnten zum Beispiel die Produktionsorte der durch Strahlionenverluste generierten Sekundärelektronen lokalisiert werden. Durch den Einbau einer Repeller-Elektrode war es möglich, den Elektronenstrom auf den Detektor durch Anlegen eines negativen Potentials zu verhindern und durch das Anlegen eines positiven Potentials sämtliche Elektronen aus dem Transportkanal abzusaugen. Im Ergebnis führten diese Untersuchung zur Klassifikation von drei Arten von Sekundärelektronen und deren Einfluss auf die Messungen und den Strahltransport. Dies ermöglichte im Zusammenspiel mit der Screening-Elektrode der Ionenquelle auch eine Variation der Raumladung des Ionenstrahles, so dass der Strahltransport durch das Toroidsegment als Funktion des Eigenfeldes des Strahles untersucht werden konnte.

Durch die Vielzahl an Experimenten zum Strahltransport konnte das im Rahmen der Arbeit entwickelte Computerprogramm (TBT) erfolgreich evaluiert werden. Die Messergebnisse konnten durch das numerische Modell mit geringen Abweichungen reproduziert werden, so dass sich das Programm dazu eignen sollte die Strahldynamik in einem kompletten Ring zu beschreiben und die Auslegung des Injektionssystems zu berechnen. Gerade die Injektion in einen toroidalen Speicherring stellt wegen der geschlossenen magnetischen Flächen eine Herausforderung dar.

Für die Injektion in den Speicherring gibt es zwei mögliche Szenarien, die mit dem Programm TBT untersucht wurden. Der Ionenstrahl könnte wie in Abbildung (2) links dargestellt in den geraden Bereichen mit Hilfe eines elektrischen Kickers in das Ringvolumen injiziert werden. Es ist jedoch auch möglich die Injektion zwischen den Toroidsegmenten zu installieren wie in Abbildung (2) rechts skizziert.

Da das Injektionssystem zu einem späteren Zeitpunkt mit der im Rahmen dieser Arbeit aufgebauten Experimentieranordnung untersucht werden soll, wurde

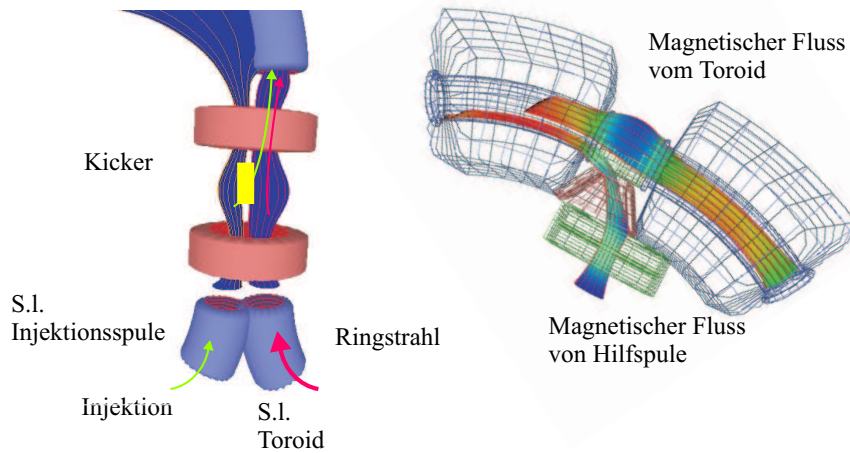


Figure 2: Schematische Darstellung des Injektionssystems für den geplanten Hochstromspeicherring (links) und des untersuchten Injektionsexperiments mit den zwei normalleitenden Toroidsegmenten (rechts).

die Injektion auf die vorhandene Spezifikation der Toroidsegmente angepasst. Der bisherige Aufbau soll zunächst um ein Toroidsegment erweitert werden und ermöglicht so den Einfluss des Kickers auf den im Ring zirkulierenden Strahl zu untersuchen. Die Transportrechnungen mit TBT ergaben für das geplante Setup optimale Abmessungen der Ablenkplatten, um bei möglichst großen Driften, die für die Injektion benötigt werden geringe Störungen des Primärstrahles zu erreichen. Für die kommenden Experimente wird eine baugleiche Ionenquelle verwendet, die den Injektionsstrahl erzeugen soll. Die Strahlanpassung erfolgt mit Hilfe eines Solenoiden, während die Ankopplung der Strahltrajektorien an den Feldverlauf im Ringsegment mit Hilfe von Hilfsspulen erfolgen soll, deren sorgfältige Auslegung mit TBT erfolgte. Der Strahltransport durch die Toroidsegmente ist sehr sensitiv auf die Randfelder der Hilfsspulen. Es konnte aber gezeigt werden, dass es Einstellungen gibt, bei denen sich ein Ionenstrahl bei guter Transmission injizieren lässt, während der im Ring zirkulierende Strahl kaum beeinflusst wird. Eine große Variation der Einschlussparameter bei den Simulationen lieferte schließlich die Akzeptanz des Injektionssystems sowie dessen Abbildungseigenschaften.

Als Fazit lässt sich konstatieren, dass im Rahmen der vorliegenden Arbeit der Ionenstrahltransport durch ein Toroidsegment erstmalig bezüglich der horizontalen und vertikalen Driften untersucht wurde. Die Entwicklung eines numerischen Modells und dessen Evaluierung mit Hilfe von Messergebnissen mündeten in ein Computerprogramm (TBT), das für die Auslegung des geplanten Hochstromspeicherrings und das benötigte Injektionssystem verwendet werden kann. Viele Fragen, die bei den Untersuchungen aufgeworfen wurden, wie zum Beispiel die Rolle der produzierten Sekundärelektronen beim toroidalen Strahltransport oder die Strahl diagnose im Inneren des toroidalen Speicherrings, können erst in weiteren Experimenten untersucht werden.

# Contents

<b>1</b>	<b>Introduction</b>	<b>1</b>
<b>2</b>	<b>Theory and simulation techniques</b>	<b>4</b>
2.1	Particle motion in magnetic fields . . . . .	4
2.1.1	Charged particle gyration . . . . .	4
2.1.2	$\mathbf{R} \times \mathbf{B}$ Drift . . . . .	5
2.1.3	$\nabla \mathbf{B}$ drift . . . . .	6
2.1.4	$\mathbf{E} \times \mathbf{B}$ drift . . . . .	7
2.1.5	Collective behavior of charged particles . . . . .	8
2.1.6	Figure-8 ring . . . . .	10
2.2	Simulation Techniques . . . . .	10
2.2.1	Circular Toroidal Coordinates . . . . .	13
2.2.2	Matrix solution with iterative method . . . . .	17
2.2.3	Equation of motion and symplectic integrator . . . . .	20
2.2.4	Efficiency of simulation code . . . . .	21
<b>3</b>	<b>Transport in a single toroidal segment</b>	<b>24</b>
3.1	The geometry and input parameters for simulations . . . . .	24
3.2	Analysis parameter <i>velocity ratio</i> ( $v_\lambda$ ) and a mapping technique . . . . .	25
3.3	Analytical calculation for the proton beam . . . . .	28
3.4	Single particle simulation . . . . .	29
3.5	Simulations of proton beam with multi particles . . . . .	30
3.5.1	Beam properties with energy variation . . . . .	30
3.5.2	Beam properties at various input distributions . . . . .	30
3.5.3	Beam properties with variable magnetic field . . . . .	32
3.5.4	Effect of self fields . . . . .	34
3.6	Comparison with analytical values . . . . .	37
<b>4</b>	<b>Experiments</b>	<b>38</b>
4.1	Characterization of Ion Source . . . . .	38
4.1.1	$He^+$ beam . . . . .	42
4.1.2	Proton beam . . . . .	45
4.2	Solenoidal Transport . . . . .	48
4.2.1	Simulations with measured data . . . . .	49
4.2.2	$He^+$ beam transport through solenoid . . . . .	49
4.2.3	<i>Proton</i> beam transport . . . . .	51
4.2.4	Effect of magnetic field from toroidal segment . . . . .	52
4.3	Transport through a toroidal segment . . . . .	55
4.3.1	Input Parameter Space . . . . .	55
4.3.2	Acceptance of an emittance scanner . . . . .	60
4.3.3	Measurement with emittance scanner . . . . .	61



4.3.4	Optical diagnostics assembly . . . . .	62
4.3.5	Measurements with phosphor screen . . . . .	64
4.3.6	Self field effect . . . . .	68
4.3.7	Comparing the simulations with measurements . . . . .	69
4.3.8	$He^+$ beam . . . . .	72
4.3.9	Electron beam . . . . .	73
<b>5</b>	<b>Injection System</b>	<b>75</b>
5.1	Simplified field model . . . . .	76
5.2	Magnetic field design for injection experiments . . . . .	79
5.2.1	Optimization for the circulating beam . . . . .	79
5.2.2	Optimization for injection coil . . . . .	80
5.2.3	Phase-space acceptance . . . . .	85
5.2.4	Self field effect . . . . .	85
5.2.5	Effect of energy variation . . . . .	85
5.2.6	Misalignment errors . . . . .	86
5.3	Kicker system for injection . . . . .	88
5.3.1	$\mathbf{E} \times \mathbf{B}$ drift . . . . .	89
5.3.2	Beam simulations in a kicker system . . . . .	90
5.3.3	Effect of fringing fields on the injected beam . . . . .	92
5.4	Two beam simulation . . . . .	93
<b>6</b>	<b>Conclusions</b>	<b>95</b>
<b>A</b>		<b>97</b>
A.1	Poisson Solver with FFT . . . . .	97
A.2	Magnetic field measurements and simulation . . . . .	99
A.3	Magnetic shielding of Turbo molecular pump . . . . .	102
A.4	Image calibration for optical measurements . . . . .	105
A.5	Photographs . . . . .	106
	<b>References</b>	<b>108</b>
	<b>Acknowledgements</b>	<b>113</b>

# Chapter 1

## Introduction

This thesis, regarding beam transport investigations, is related to the larger research fields, **storage rings** used in accelerator physics and **non-neutral plasmas**. The proposal of building a storage ring with longitudinal guiding magnetic fields was made. Due to natural transversal focussing in magnetic fields it is possible to accumulate very intense charged particle beams, a subject of interest within the physics community. A lot of interest has emerged in the field of moving plasmas in toroidal like systems. Study of moving plasmas revolves around the confinement theory, fusion reactions and efficient injection systems, neutral beam heating and production of non-conventional plasmas like anti matter plasmas.

The concept of a storage ring with a longitudinal magnetic field for accumulation of intense  $150\text{ keV}$  proton beams was proposed in 2002 by U. Ratzinger [1] and later presented and published in the European Particle Accelerator Conference in 2004 [2]. The figure-8 shape is the natural choice to compensate the vertical drift arising from curved magnetic field lines. Additionally it provides the *rotational transform* for magnetic fields. Figure-8 shaped stellarators were investigated for plasma confinement in fusion research [3][4]. The magnetic confinement was based on strong magnetic fields produced by toroidal coils around a vessel. The plasma was induced by ionizing and heating the gas by energetic particles or by electric fields. A quasi-neutral plasma would then have to be confined on closed magnetic field lines. Parallel research on the Tokamak, a toroidal device, found increasing popularity over stellarators which used high plasma current to produce the helical component of a magnetic field. Recently stellarators have again found more interest and research with modular coils is gaining attention.

The main distinction to the storage ring scenario lies in the stored energy. The storage ring accumulates single specie low energy ion beams up to a few *Ampere* beam currents producing low magnetic self-fields. Due to the electron flow, the plasma current is much higher in stellarators and tokamaks within the order of  $kA$  to  $MA$  range. This leads to the unfolding of a rotational transform and results in kink instabilities [5][6].

A similarity can be seen in terms of magnetic field configuration. A rotational transform is provided by twisting a toroidal shaped ring into a figure-8. In such a configuration the magnetic field lines do not enclose in a circle but form a surface called magnetic flux surface. Figure 1.1 shows a simulated magnetic surface with colour-coded magnetic field strength and a single particle trajectory with  $\mathbf{F} \times \mathbf{B}$  drift envisaged. The energetic ( $100 - 200\text{ keV}$ ) runaway electrons confined over the time scale of few seconds in stellarators gives us a clue for the confinement of single specie charged particle beams [7].

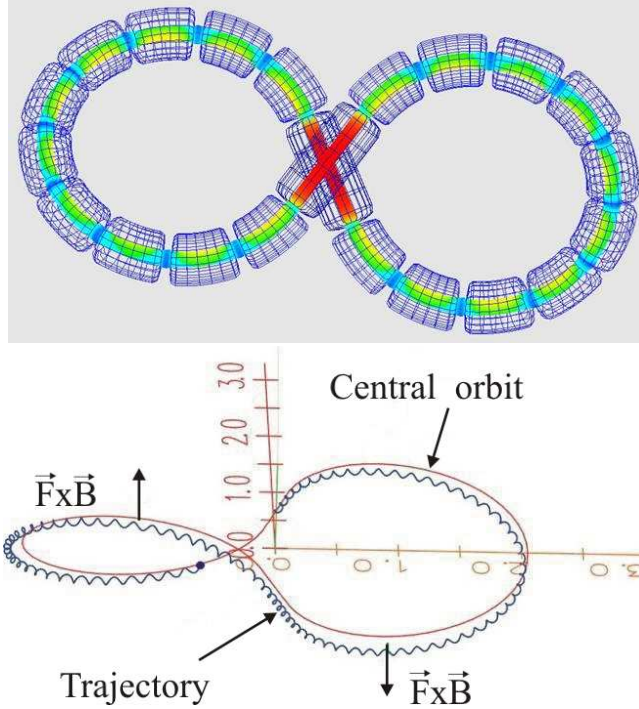


Figure 1.1: An example of a magnetic surface of the segmented figure-8 structure (top) and single particle trajectory (bottom).

In the recent years the subject of confinement of a single specie plasma, especially a pure electron plasma has aroused interest within the scientific community. Literature by A. Boozer extensively investigates pure electron plasmas and confinement by magnetic surfaces [8][9][10]. The theory is being directly compared with the Columbia Nonneutral Torus (CNT) experiments [11][12]. The additional prospects of positron-electron plasma has also been discussed in [13].

The problem of confining the self consistent electron plasma in a toroidal field was addressed as early as 1967 [14]. In SPAC-II an axisymmetric toroidal device, relativistic electron beams were investigated [19]. Recently, trapped electron clouds in toroidal magnetic fields were studied with respect to stability, equilibrium and space-charge issues [15]-[18].

In the Prototype-Ring Trap (PROTO-RT) from Tokyo University, a central conductor was used to provide confinement [20][21].

The dynamics of electron clouds in a partial torus was investigated at Lawrence University[22]. Successful trapping was observed using electrodes with a horizontal electric field ( $0.5 - 1.0 \text{ kV/m}$ ).

In accelerator physics a toroidal magnetic field configuration is mostly used in electron coolers [23][24]. The Low Energy Particle Toroidal Accumulator (LEPTA) project incorporates a small positron storage ring. Positrons are cooled by circulating electron beams [25]. Another example is a proposed Muon to Electron CONversion (MECO) project, where toroidal like sectors are used for secondary specie separation, confinement and guidance to the detector.

The preliminary beam investigations with room temperature toroidal magnets undertaken at IAP Frankfurt were necessary to study the dynamics of positive

beams in toroidal like magnetic field configurations. The experiments with small segments provide a basic understanding of the beam dynamics, diagnostics system, and beam injection schemes. It provides a comparison between numerical simulations and experimental results. The calculations and design, which demands for precise simulations and possibility of practical realization for an injection system, forms a core of the thesis.

In the first chapter, the drift theory in toroidal magnetic fields and simulation techniques are discussed. A numerical code was necessary to investigate the drift motions and space-charge effects. Multiple species can be simulated with the code. It also includes the possibility to simulate a beam with measured phase-space distribution. The theoretical calculations and matching conditions for beam transport in a single toroidal segment are described in the following chapter.

The experiments were carried out using a single segment with toroidal magnetic field. Beam dynamics and transport of multi specie beams were studied. The challenges in detection systems are discussed in the fourth chapter. It also describes the space-charge effects to some extent. The comparison of experimental results with simulations forms a basis to design an injection system.

The last chapter deals with the injection system. As ions can not be generated and accelerated conventionally inside the vessel, they have to be injected into the ring acceptance with its high magnetic fields. This results in a complicated multiturn injection scheme, as the circulating particles have to be kept on stable tracks. A new system for this purpose with special magnetic fields is designed and analyzed in detail.

# Chapter 2

## Theory and simulation techniques

### 2.1 Particle motion in magnetic fields

#### 2.1.1 Charged particle gyration

The equation of motion for charged particles in homogeneous magnetic fields is given by

$$m \frac{d\mathbf{v}}{dt} = q(\mathbf{E} + \mathbf{v} \times \mathbf{B}). \quad (2.1)$$

Ignoring electric fields and taking magnetic field in longitudinal  $z$ -direction only, we have

$$\begin{aligned} \ddot{v}_x &= \frac{qB}{m} \dot{v}_y = -\left(\frac{qB}{m}\right)^2 v_x, \\ \ddot{v}_y &= -\frac{qB}{m} \dot{v}_x = -\left(\frac{qB}{m}\right)^2 v_y. \end{aligned} \quad (2.2)$$

This describes a simple harmonic oscillator at *cyclotron frequency* which is defined as

$$\omega_c = \frac{|q|B}{m}. \quad (2.3)$$

The solution is then written as

$$v_{x,y} = v_{\perp} \exp(\pm i\omega_c t + i\delta_{x,y}). \quad (2.4)$$

The  $\pm$  denoting sign of  $q$ . We may choose the phase  $\delta$  so that

$$v_x = v_{\perp} e^{i\omega_c t} = \dot{x}, \quad (2.5)$$

where  $v_{\perp}$  is a positive constant denoting the speed in plane perpendicular to  $\mathbf{B}$ . This gives,

$$v_y = \frac{m}{qB} \dot{v}_x = \pm i v_{\perp} e^{i\omega_c t} = \dot{y}. \quad (2.6)$$

Integrating, we have

$$\begin{aligned} x - x_0 &= -i \frac{v_{\perp}}{\omega_c} e^{i\omega_c t}, \\ y - y_0 &= \pm \frac{v_{\perp}}{\omega_c} e^{i\omega_c t}. \end{aligned} \quad (2.7)$$

The *gyro radius* is defined as

$$r_g \equiv \frac{v_{\perp}}{\omega_c} = \frac{mv_{\perp}}{|q|B}. \quad (2.8)$$

Taking the real part

$$\begin{aligned} x - x_0 &= r_g \sin \omega_c t, \\ y - y_0 &= \pm r_g \cos \omega_c t. \end{aligned} \quad (2.9)$$

This describes a circular orbit with a guiding centre  $(x_0, y_0)$ . The direction of gyration is always such that the magnetic field generated by charged particles is opposite to the external imposed field (Lenz rule). In addition to this motion, there is velocity  $v_z$  along  $B_z$  which is unaffected. Thus the trajectory of particles is a helix.

### 2.1.2 $\mathbf{R} \times \mathbf{B}$ Drift

In general, if a force  $\mathbf{F}$  is acting on the moving particle, the corresponding drift velocity is derived as [26],

$$\mathbf{v} = \frac{1}{q} \frac{\mathbf{F} \times \mathbf{B}}{B^2}. \quad (2.10)$$

In particular, if magnetic lines are curved with a constant radius  $R_c$  and a constant  $|B|$  is assumed, a particle experiences a drift perpendicular to the centrifugal force. Particles experience a drift velocity given by

$$\mathbf{v}_R = \frac{mv_{\parallel}^2}{qB^2} \frac{\mathbf{R}_c \times \mathbf{B}}{R_c^2}. \quad (2.11)$$

This drift is called *curvature drift* (see Figure 2.1 ). The direction of velocity depends on the charge. Thus positive ions and electrons will be drifted in opposite directions if injected into a magnetic field with the same longitudinal velocity direction. When a proton beam is injected in a curved magnetic field it will experience a vertical drift. The shift in position is proportional to longitudinal velocity. For a ring with toroidal magnetic field this is the major effect that has to be compensated along each turn. Let  $v_R$  be the drift velocity and  $\Delta t$  be the time required to complete one turn. Then we can write

$$v_R = \frac{mv_{\parallel}^2}{qBR}; \quad \Delta t = \frac{2\pi R}{v_{\parallel}}. \quad (2.12)$$

Then, the vertical shift in beam position in one round turn is given as

$$\Delta l = v_R \Delta t = 2\pi \frac{mv_{\parallel}}{qB}, \quad (2.13)$$

which is independent of major radius  $R$ .

The proton beam of  $10 \text{ keV}$  energy experiences a  $12 \text{ mm}$  vertical shift from the geometrical centre when injected in a  $30^\circ$  toroidal sector with major radius  $1.3 \text{ m}$  at  $0.6 \text{ T}$ ; i.e. a drift of  $144 \text{ mm}$  for  $360^\circ$  arc angle. For  $100 \text{ keV}$  proton beam in a  $5 \text{ T}$  magnetic field, the beam shift is  $57 \text{ mm}$  in a single turn ( $360^\circ$  arc angle). Relevant numbers for the experimental test setup are tabulated in chapter 3 and 4.

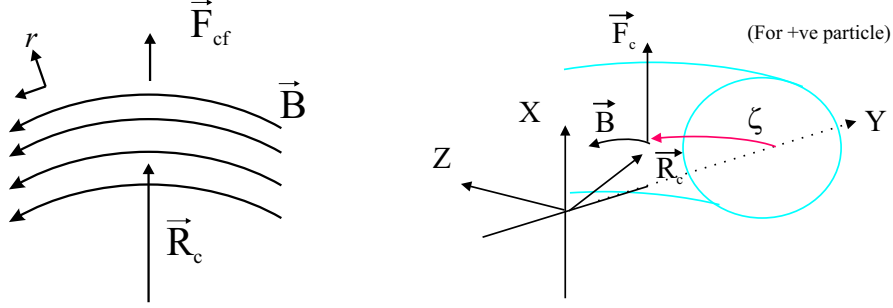


Figure 2.1: Left: The generalized force and radius vector in top view. Right: The direction  $\mathbf{v}_R$  of the  $\mathbf{R} \times \mathbf{B}$  drift for positively charged particles. For electrons, force is in the opposite direction.

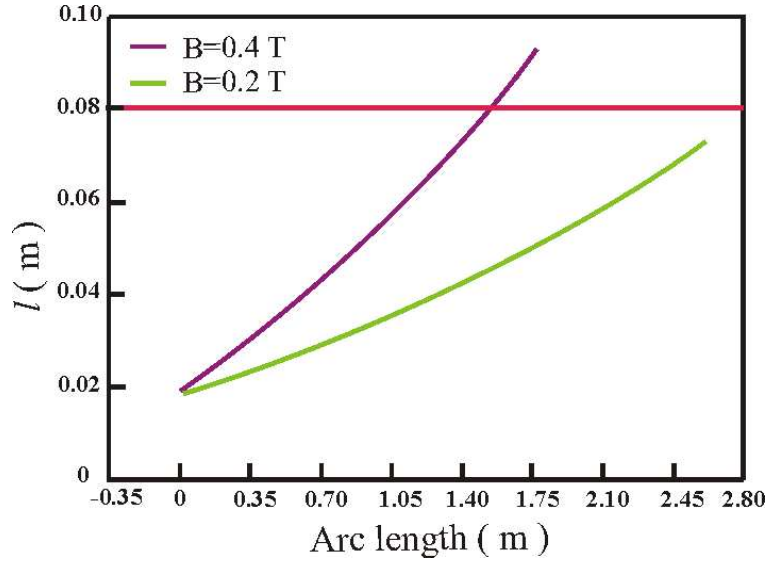


Figure 2.2: Vertical shift against the path length along a torus with  $R_0 = 1.0 \text{ m}$  at an energy of  $6 \text{ keV}$ . Initial  $20 \text{ mm}$  added for beam radius. The horizontal line represents maximum acceptable drift with respect to the vessel aperture.

The graph in figure 2.2 shows the vertical shift of a beam with energy  $6 \text{ keV}$  at two different toroidal magnetic field levels.

### 2.1.3 $\nabla B$ drift

The inner and outer radii differ for a torus, the coil density is different on either side. This gives rise to a non uniform magnetic field along the radial direction (see figure 2.3). The drift velocity associated with varying magnetic field is given by

$$\mathbf{v}_{\nabla B} = \pm \frac{1}{2} v_{\perp} r_g \frac{\mathbf{B} \times \nabla B}{B^2}, \quad (2.14)$$

where  $\pm$  indicates the charge of particle.

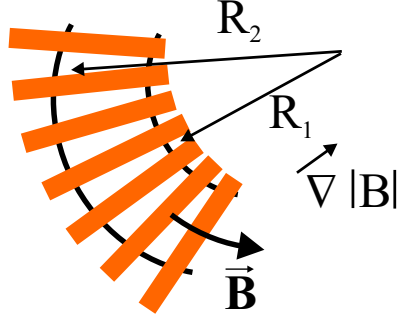


Figure 2.3: Figure showing the difference between inner and outer radii of a torus. This results in a radial magnetic field gradient  $\nabla|B|$ .

In cylindrical coordinates  $\nabla \times \mathbf{B}$  only has a  $z$  component, in vacuum we have

$$\begin{aligned} \frac{1}{r} \frac{\partial}{\partial r}(rB_\theta) &= 0 \\ \implies B_\theta &\propto \frac{1}{r}. \end{aligned} \quad (2.15)$$

This gives,

$$\frac{\nabla|B|}{|B|} = -\frac{\mathbf{R}_c}{R_c^2}. \quad (2.16)$$

Substituting in equation(2.14) the drift velocity is written as,

$$\mathbf{v}_{\nabla B} = \frac{1}{2} \frac{m}{q} v_\perp^2 \frac{\mathbf{R}_c \times \mathbf{B}}{R_c^2 B^2}. \quad (2.17)$$

In case of an ion beam, the transverse velocity is usually lower than the longitudinal velocity. The vertical  $\mathbf{R} \times \mathbf{B}$  drift velocity dominates over the  $\nabla \mathbf{B}$  drift velocity. Moreover the phase space distribution of the beam can be chosen by a focussing element so that the beam at injection is matched to the magnetic field direction making the  $\nabla \mathbf{B}$  drift as low as possible.

#### 2.1.4 $\mathbf{E} \times \mathbf{B}$ drift

In the presence of an electric field  $\mathbf{E}$ , say  $E_x$ , Lorentz force equation can be solved to give the  $y$ -component of velocity as

$$v_y = \pm i v_\perp e^{i\omega ct} - \frac{E_x}{B}. \quad (2.18)$$

Thus the drift velocity of the guiding center is in  $-y$  direction. The transverse component of drift velocity can be deduced from equation (2.10) as

$$\mathbf{v}_{\perp gc} = \mathbf{E} \times \mathbf{B} / B^2 \equiv \mathbf{v}_E. \quad (2.19)$$

We define this as  $\mathbf{v}_E$ , the electric field drift of the guiding centre. The magnitude of drift velocity is



$$v_E = \frac{E(V/m)}{B(\text{tesla})} \frac{m}{\text{sec}}. \quad (2.20)$$

This drift velocity is independent of mass and charge of particle.

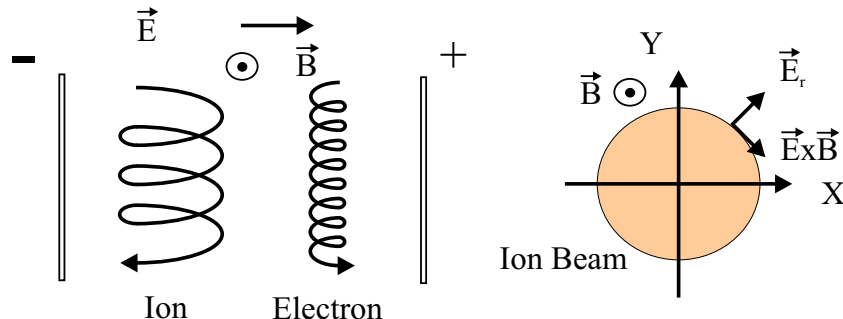


Figure 2.4:  $\mathbf{E} \times \mathbf{B}$  drift for a single particle (left) and beam rotation caused by  $\mathbf{E}_r$  from self field (right).

An effect due to the self field of the charged particle beam is the rotation of the beam around its axis. The particles at the boundary of a beam with homogeneous constant space charge density experience maximum electric field in radial direction. Thus, together with the longitudinal magnetic field this leads to a rotation of the particles around the beam axis (see figure 2.4 ).

## 2.1.5 Collective behavior of charged particles

### Debye screening

When a positively charged particle with charge  $Ze$  is placed in the plasma, it redistributes the ions and electrons surrounding in such a way that Coulomb electrostatic potential  $\phi_c \approx Ze/4\pi\epsilon_0 r$  is attenuated at distance beyond *Debye length*. This effect is known as *Debye screening*[27]. A Maxwell-Boltzmann distribution function with

$$f(\mathbf{x}, \mathbf{v}) = n_0 \exp\left(-\frac{mv^2}{2k_B T} + \frac{e\phi}{2k_B T}\right), \quad (2.21)$$

and density

$$n(r) = n_0 \exp\left(\frac{e\phi(r)}{k_B T}\right) \quad (2.22)$$

is assumed.

Here  $k_B$  is Boltzmann constant. Then the potential must satisfy Poisson's equation, which is written in spherical symmetry as,

$$\frac{1}{r^2} \frac{d}{dr} r^2 \frac{d\phi}{dr} = \frac{2n_0 e^2}{\epsilon_0 k_B T} \phi, \quad (2.23)$$

under the assumption  $e\phi/k_B T \ll 1$ . Taking the solution which vanishes at  $r \rightarrow \infty$ ,

$$\phi = \frac{A}{r} \exp(-r/\lambda_D), \quad (2.24)$$

where

$$\lambda_D = \sqrt{\frac{\epsilon_0 k_B T}{2n_0 e^2}}, \quad (2.25)$$

is known as the Debye length.

### Brillouin limit

The maximum number density that can be transported through a magnetic field is limited by the Brillouin limit [28] given by

$$n_B = \frac{\epsilon_0 B^2}{2m}, \quad (2.26)$$

where  $\epsilon_0$  is a permittivity of space and  $m$  is mass of the particles. This is expressed in units of  $m^{-3}$ . The Brillouin limit in turn imposes the current density limit that can be transported through a magnetic configuration. The maximum current density is then given as

$$j_{\parallel} = n_B q v_{\parallel}. \quad (2.27)$$

Table (2.1) and (2.2) summarizes some of the beam transport properties in different scenario of low energies with low magnetic fields and higher energy with higher magnetic fields.

Table 2.1: Beam Transport properties at low energies for 0.6 T in 30° sector with  $R_0 = 1.3 m$

Energies $W_{\parallel}$	4 keV	10 keV	20 keV
Velocity (m/s)	8.8e05	1.38e06	1.95e06
Time of flight (s)	7.73e - 07	4.93e - 07	3.49e - 07
No. of Oscillations	7.1	4.5	3.2
Vertical drift (mm)	8.0	12.5	17.6
Maximum current density (mA/cm <sup>2</sup> )	13.5	21.4	30.0

Table 2.2: Beam Transport properties at high energy (150 keV) for higher magnetic fields in 30° sector with  $R_0 = 1.3 m$

Magnetic field (B)	2.0 T	5.0 T
Velocity (m/s)	5.37e06	
Time of flight (s)	1.27e - 07	
No. of Oscillations	3.9	9.8
Vertical drift (mm)	14.6	5.8
Maximum current density (A/cm <sup>2</sup> )	0.92	5.74

### 2.1.6 Figure-8 ring

The vertical drift for a single turn in a torus could be very high. This causes beam loss on the wall. To overcome this problem a simple arrangement of figure-8 can be used. As shown in figure 2.5 a ring is twisted to form an 8 shaped figure. In either arm of this ring the  $\mathbf{R} \times \mathbf{B}$  force is in opposite directions. The vertical drift is thus compensated.

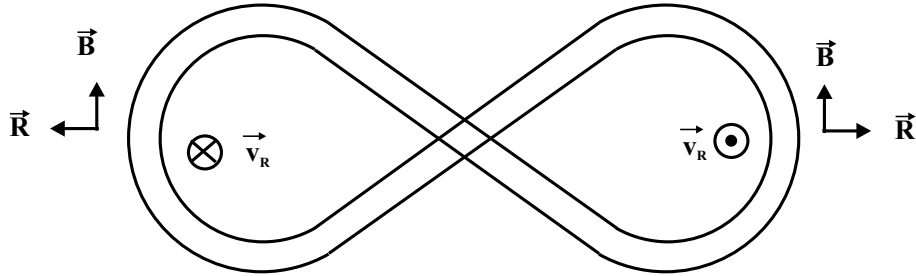


Figure 2.5: Figure-8 type ring showing the vertical drift compensation on either side.

## 2.2 Simulation Techniques

The Particle in Cell method was used to simulate the beam transport in external magnetic fields including the space charge effect. Figure 2.6 shows the block diagram of this PIC scheme.

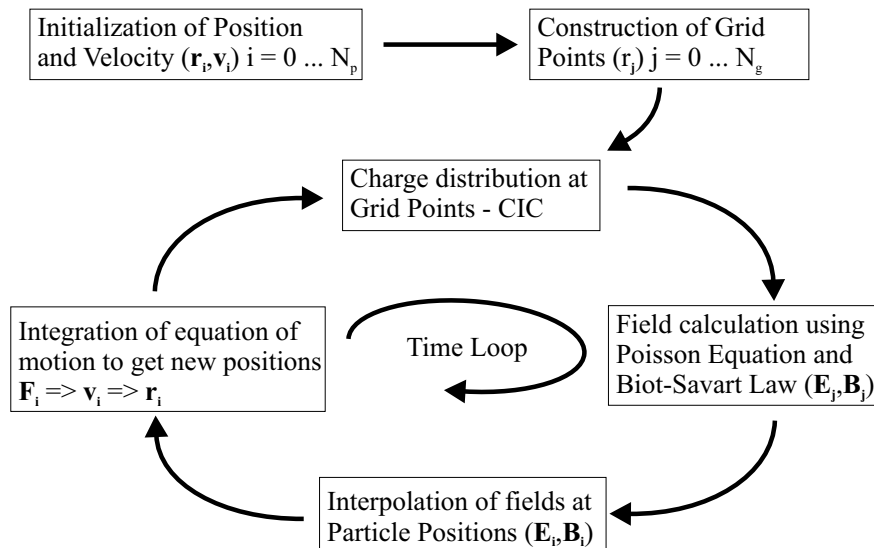


Figure 2.6: Flow chart of a PIC scheme.

In a first step the simulation program generates particle positions and velocities in 6-dimensional phase-space. Then it initializes the static mesh depending on

the geometry in demand. The magnetic field is then calculated at grid points using Biot-Savart law by defining real coil geometry. The space charge routine is then evoked to calculate the charge densities at grid points, consequently which calculates potential and electric fields at grid points. These fields are interpolated at particle positions and then the particle positions are advanced in time using a discretised Lorentz equation of motion [29].

## Initialization of particle coordinates

The initial distribution is defined as homogenous distribution, Kapchinsky-Vladimirsky (KV) or can be read from an external file, which provides an opportunity to simulate the transport with measured particle distributions. In the case of theoretical studies homogeneous distribution was used and measured distributions were used for comparison with experimental data.

## Charge distribution

For efficient calculation of inter particle forces the Particle in Cell method was used, also known as Cloud in cell (CIC) method. Cartesian, cylindrical, or toroidal grids, as per requirement imposed by geometry were generated. The first order weighted scheme was used to calculate the charge density at grid points. The particle is identified in a particular cell and then the charge is attributed to grid points according to relative volume in 3D space.

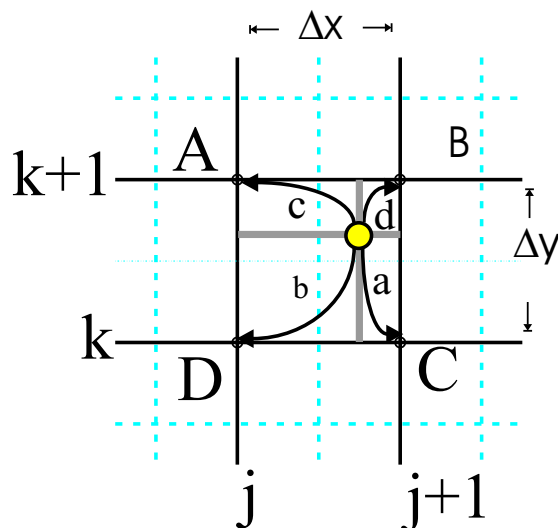


Figure 2.7: PIC charge distribution in cartesian.

For example, as shown in figure 2.7 in 2-dimension, a particle is identified at point B called Nearest Grid Point (NGP). The charge of this particle, which can be macro particle with cluster of particles, is divided according to inverse area weight. Charge density at every point is given by

$$\begin{aligned}
Q_A &= Q_0 \frac{\text{area}(a)}{\text{area}(ABCD)}, \\
Q_B &= Q_0 \frac{\text{area}(b)}{\text{area}(ABCD)}, \\
Q_C &= Q_0 \frac{\text{area}(c)}{\text{area}(ABCD)}, \\
Q_D &= Q_0 \frac{\text{area}(d)}{\text{area}(ABCD)},
\end{aligned} \tag{2.28}$$

where  $Q_0$  is the macro charge of a single particle. Thus the nearest grid point, point B, is weighted maximum when compared to the point D.

## Potential and Electric field at Grid points

Potential was calculated using the Poisson equation

$$\nabla^2 \phi(\mathbf{r}) = \frac{-\rho(\mathbf{r})}{\epsilon_0}. \tag{2.29}$$

The periodicity in mesh structure gives a main advantage for the fast calculations of potential and electric field against particle-particle force calculation. For a general one dimensional case, the equation (2.29) can be written in a discretised dimensionless form as

$$\begin{aligned}
\phi_{N_g} - 2\phi_1 + \phi_2 &= \rho_1 \\
\phi_1 - 2\phi_2 + \phi_3 &= \rho_2 \\
&\vdots \\
\phi_{N_g-2} - 2\phi_{N_g-1} + \phi_{N_g} &= \rho_{N_g-1} \\
\phi_{N_g-1} - 2\phi_{N_g} + \phi_1 &= \rho_{N_g}.
\end{aligned} \tag{2.30}$$

Here  $\phi_i$ 's represent potential at grid points ( $N_g$ ) and  $\rho_i$ 's represent charge densities. This system of equation is readily solved with Fast Fourier Transform for simple periodic cartesian coordinates. Integrating with respect to mesh sizes electric fields at mesh points are obtained

## Fourier transform

For a periodic system, discrete fourier series for all grid quantities can be used. Thus fourier transform  $\rho(\mathbf{k})$  of  $\rho(\mathbf{x})$  can be calculated, where  $\mathbf{k}$  is the wave vector in fourier transform kernel. The equation(2.29) can be rewritten in Fourier space as

$$\phi(k) = \frac{\rho(k)}{\epsilon_0 k^2}. \tag{2.31}$$

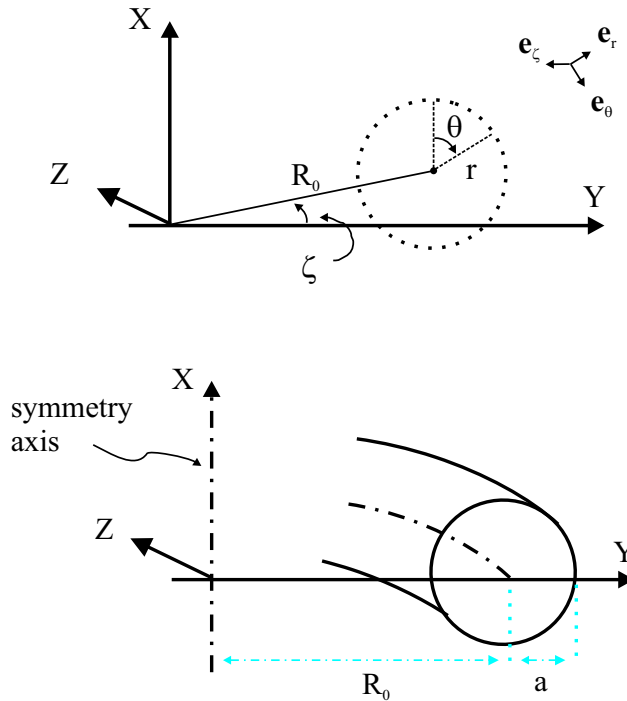
By calculating  $\phi(\mathbf{k})$  and then taking a reverse transform we get potential and electric fields on grid points. Again a weighted scheme was used to calculate the electric field at particle position.

$$\rho(\mathbf{x}) \longrightarrow \rho(\mathbf{k}) \longrightarrow \phi(k) \longrightarrow \phi(\mathbf{x}) \longrightarrow \mathbf{E}(\mathbf{x}) \quad (2.32)$$

Detail of a code and boundary conditions are described in the appendix A.1. Although this method is very effective in terms of speed, setting boundary condition, external definition of fields and matching with geometry, is inconvenient. Thus matrix method was used for efficient calculation in toroidal coordinates.

### 2.2.1 Circular Toroidal Coordinates

For the simulation of beam transport in toroidal magnetic field, the circular toroidal coordinate system was used. This is shown in figure 2.8. To be consistent with accelerator physics notations the transverse plane was defined to be  $x - y$  plane at injection plane [31].




---

Figure 2.8: Concentric circular toroidal coordinates.

With respect to the cartesian plane the  $x$ -axis was taken as a symmetry axis of tori and  $y - z$  plane as symmetry plane. If  $R_0$  is the major radius then any point in the region of interest is given by three coordinates as

- $r$  : minor radius of toroidal segment;
- $\theta$  : the poloidal angle measured in  $x - y$  plane from  $+ve$   $x$ -axis;
- $\zeta$  : the toroidal angle.

The relationship between cartesian and toroidal coordinates is given by,

$$\begin{aligned}x &= r \sin \theta \\y &= (R_0 + r \cos \theta) \sin \zeta \\z &= (R_0 + r \cos \theta) \cos \zeta.\end{aligned}\tag{2.33}$$

Inverse relations are

$$\begin{aligned}r &= \{x^2 + ((y^2 + z^2)^{1/2} - R_0)^2\}^{1/2} \\ \theta &= \tan^{-1}\{((y^2 + z^2)^{1/2} - R_0)/x\} \\ \zeta &= \tan^{-1}(z/y).\end{aligned}\tag{2.34}$$

This coordinate system is right handed and orthogonal. The scaling factors are given as,

$$\begin{aligned}h_r &= 1 \\ h_\theta &= r \\ h_\zeta &= R_0 + r \cos \theta.\end{aligned}\tag{2.35}$$

The volume element is

$$\begin{aligned}d^3\mathbf{x} &= h_r h_\theta h_\zeta dr d\theta d\zeta \\ &= r (R_0 + r \cos \theta) dr d\theta d\zeta.\end{aligned}\tag{2.36}$$

### Magnetic field in toroidal coordinates

If  $a$  is the inner radius of a torus and  $R_0$  is the major radius then *aspect ratio* is defined as

$$A = \frac{R_0}{a} > 1.\tag{2.37}$$

The magnetic field in the standard toroidal coordinates is given as

$$B(r, \theta) = \frac{B_0}{q(r)} \frac{r}{R_0} \mathbf{e}_\theta + \frac{B_0}{1 + (r/R_0)\cos \theta} \mathbf{e}_\zeta,\tag{2.38}$$

where  $B_0$  is constant and  $q(r)$  is a dimensionless function of  $r$ . In tokamak physics  $q(r)$  is known as *winding number* (or safety factor). Equation(2.38) defines an axisymmetric magnetic field compatible with magnetic surfaces if the condition

$$\bar{\eta} = \frac{a}{R_0} \ll 1,\tag{2.39}$$

is satisfied. The term  $\bar{\eta}$  is called *inverse aspect ratio*.

### Charge distribution in toroidal coordinates

The charged distribution in toroidal coordinates can be calculated in the same way as in the cartesian system. Figure 2.9 shows a 2-dimensional projection.

The macroparticle charge is divided into an 8 point polynomial except at the centre where it is a 6 point polynomial. Weighting factor is given with respect to the volume element.

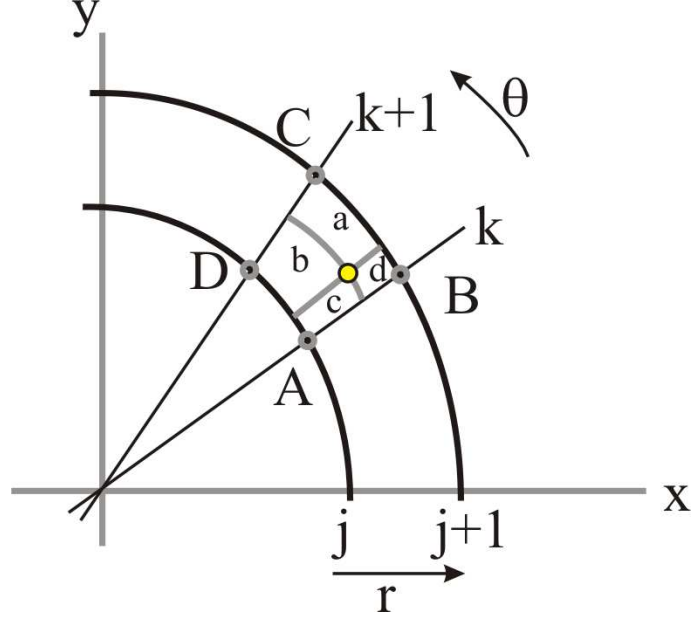


Figure 2.9: PIC charge distribution in toroidal coordinates in 2-dimensional projection.

### Poisson equation in toroidal coordinates

The Poisson equation in circular toroidal coordinates is written as,

$$\nabla^2 \phi = \frac{\partial^2 \phi}{\partial r^2} + \frac{R_0 + 2r \cos \theta}{r(R_0 + r \cos \theta)} \frac{\partial \phi}{\partial r} - \frac{\sin \theta}{r(R_0 + r \cos \theta)} \frac{\partial \phi}{\partial \theta} + \frac{1}{r^2} \frac{\partial^2 \phi}{\partial \theta^2} + \frac{1}{(R_0 + r \cos \theta)^2} \frac{\partial^2 \phi}{\partial \zeta^2} = -\frac{\rho}{\epsilon_0}. \quad (2.40)$$

Using the finite difference method this can be discretised,

$$\frac{\phi_{i+1,j,k} - 2\phi_{i,j,k} + \phi_{i-1,j,k}}{\Delta r^2} + \frac{R_0 + 2r_{i,j,k} \cos \theta_{i,j,k}}{r_{i,j,k}(R_0 + r_{i,j,k} \cos \theta_{i,j,k})} \frac{\phi_{i+1,j,k} - \phi_{i-1,j,k}}{2\Delta r} - \frac{\sin \theta_{i,j,k}}{r_{i,j,k}(R_0 + r_{i,j,k} \cos \theta_{i,j,k})} \frac{\phi_{i+1,j,k} - \phi_{i-1,j,k}}{2\Delta \theta} + \frac{1}{r_{i,j,k}^2} \frac{\phi_{i,j+1,k} - 2\phi_{i,j,k} + \phi_{i,j-1,k}}{\Delta \theta^2} + \frac{1}{(R_0 + r_{i,j,k} \cos \theta_{i,j,k})^2} \frac{\phi_{i,j,k+1} - 2\phi_{i,j,k} + \phi_{i,j,k-1}}{\Delta \zeta^2} = -\frac{\rho_{i,j,k}}{\epsilon_0}.$$

On rearranging the terms, we get



$$\begin{aligned}
& \phi_{i,j,k+1} \left( \frac{1}{\Delta z^2 (R_0 + r_{i,j,k} \cos\theta_{i,j,k})^2} \right) + \phi_{i,j+1,k} \left( \frac{1}{r_{i,j,k}^2 \Delta\theta^2} - \frac{\sin\theta_{i,j,k}}{2r_j \Delta\theta (R_0 + r_{i,j,k} \cos\theta_{i,j,k})} \right) \\
& + \phi_{i+1,j,k} \left( \frac{1}{\Delta r^2} + \frac{R_0 + 2r_{i,j,k} \cos\theta_{i,j,k}}{2r_{i,j,k} \Delta r (R_0 + r_{i,j,k} \cos\theta_{i,j,k})} \right) \\
& + \phi_{i,j,k} \left( -\frac{2}{\Delta r^2} - \frac{2}{2r_{i,j,k}^2 \Delta\theta^2} - \frac{2}{\Delta\zeta^2 (R_0 + r_{i,j,k} \cos\theta_{i,j,k})^2} \right) \\
& + \phi_{i-1,j,k} \left( \frac{1}{\Delta r^2} - \frac{R_0 + 2r_{i,j,k} \cos\theta_{i,j,k}}{2r_{i,j,k} \Delta r (R_0 + r_{i,j,k} \cos\theta_{i,j,k})} \right) \\
& + \phi_{i,j-1,k} \left( \frac{1}{r_{i,j,k}^2 \Delta\theta^2} + \frac{\sin\theta_{i,j,k}}{2r_j \Delta\theta (R_0 + r_{i,j,k} \cos\theta_{i,j,k})} \right) \\
& + \phi_{i,j-1,k} \left( \frac{1}{\Delta\zeta^2 (R_0 + r_{i,j,k} \cos\theta_{i,j,k})^2} \right) = -\frac{\rho_{i,j,k}}{\epsilon_0}. \tag{2.41}
\end{aligned}$$

This numerical equation is used to solve potential in a toroidal coordinate system where  $\rho_{ijk}$  are the charge densities at mesh points and  $\phi_{i,j,k}$  are potentials.

## 2.2.2 Matrix solution with iterative method

Equation(2.41) represents a discretised Poisson equation, which is set of  $N_i \times N_j \times N_k = N$  linear equations and can be written in matrix form similar to equation(2.30). This is written in the form

$$\mathbf{A} \cdot \phi = -\frac{\rho}{\epsilon_0}, \quad (2.42)$$

Form of matrix  $\mathbf{A}$  is schematically shown on the following page. This matrix consist of a multitude of zero elements, known as *sparse*. The matrix representing  $\rho$  is simply a single column matrix with  $N_i \times N_j \times N_k = N$  rows containing values of charge density at grid point. The sparse matrix format allows us to save computational memory. Since matrix  $\mathbf{A}$  contains many zeros, only non zero values required to be stored with a reference pointer. A minimum of two boundary conditions is required to solve this system of equations. One is simply given by the vessel. The mesh size in radial direction is defined till vessel of system and declared to be at zero potential.

### For $r = 0$ , Gauss Law

At  $r = 0$  we get an infinity problem, which was resolved using the Gauss' law,

$$\int E \cdot dS = \frac{Q_{enclosed}}{\epsilon_0}. \quad (2.43)$$

This also gives the second boundary condition to solve the matrix equation.

By defining the particular grid point at fixed potential and correcting corresponding equation in a matrix  $\mathbf{A}$ , the external electric field can be defined from e.g. parallel electric plates.



## Iterative methods

To solve the matrix equation iterative methods can be used. They are effective when the number of equations  $N > 10^6$ , where  $N$  is the number of grid points. The general algorithm may be written as

$$\mathbf{x}^{(k)} = \mathbf{B}\mathbf{x}^{(k-1)} + c. \quad (2.44)$$

When  $\mathbf{B}$  and  $c$  are constants in the iteration process it is called a stationary method, else called Non-stationary method [32]

- Stationary methods
  - Jacoby Method (JM)
  - Gauss-Seidel Method (GS)
  - Successive Over-Relaxation (SOR)
  - Symmetric Successive Over-Relaxation (SSOR)
- Non-stationary methods
  - Conjugate Gradient (CG)
  - Conjugate Gradient Squared (CGS)
  - BiConjugate Gradient (BiCG)
  - BiConjugate Gradient Stabilized (BiCGSTAB)
  - Chebyshev Iteration (CI)

## BiConjugate Gradient Stabilized (BiCGSTAB)

The biconjugate gradient stabilized (BiCGSTAB) method can be used to solve non-symmetric linear systems efficiently. This iterative method is based on finding local minima through the conjugate gradient calculation of function of  $n$  variables. The investigated systems in this work often exhibit irregular and various pre-defined boundary conditions, hence BiCGSTAB was used to solve the Poisson equation. Different codes were written for cylindrical and toroidal coordinates. Schematically algorithm can be illustrated as follows.

For update of residual vectors  $\mathbf{r}, \tilde{\mathbf{r}}$ , with known matrices  $\mathbf{A}, \mathbf{A}^T$  can be written

$$\begin{aligned} \mathbf{r}^{(i)} &= \mathbf{r}^{(i-1)} - \alpha_i \mathbf{A}\mathbf{p}^{(i)} \\ \tilde{\mathbf{r}}^{(i)} &= \tilde{\mathbf{r}}^{(i-1)} - \alpha_i \mathbf{A}^T \mathbf{p}^{(i)}, \end{aligned} \quad (2.45)$$

where  $\mathbf{p}^i$  is a sequence of  $n$  mutually conjugate directions. Then

$$\begin{aligned} \mathbf{p}^{(i)} &= \mathbf{r}^{(i-1)} + \beta_{i-1} \mathbf{p}^{(i-1)} \\ \tilde{\mathbf{p}}^{(i)} &= \tilde{\mathbf{r}}^{(i-1)} + \beta_{i-1} \tilde{\mathbf{p}}^{(i-1)}, \end{aligned} \quad (2.46)$$

Thus

$$\begin{aligned} \alpha_i &= \frac{(\tilde{\mathbf{r}}^{(i-1)})^T \mathbf{r}^{(i-1)}}{(\tilde{\mathbf{p}}^{(i)})^T \mathbf{A}\mathbf{p}^{(i)}} \\ \beta_i &= \frac{(\tilde{\mathbf{r}}^{(i)})^T \mathbf{r}^{(i)}}{(\tilde{\mathbf{r}}^{(i-1)})^T \mathbf{r}^{(i-1)}} \end{aligned} \quad (2.47)$$

gives the orthogonality condition for

$$(\tilde{\mathbf{r}}^{(i)})^T \mathbf{r}^{(j)} = (\tilde{\mathbf{p}}^{(i)})^T \mathbf{A} \mathbf{p}^{(j)} = 0 \quad (2.48)$$

if  $i \neq j$ .

### 2.2.3 Equation of motion and symplectic integrator

To calculate the particle motion the Lorentz force equation was used,

$$m \frac{d\mathbf{v}}{dt} = q(\mathbf{E} + \mathbf{v} \times \mathbf{B}), \quad (2.49)$$

where  $\mathbf{E}$  is electric field calculated from Poisson equation and  $\mathbf{B}$  is the magnetic field calculated using Biot-Savart law. FDTD scheme was used to discretize the equation and to calculate the time evolution of particle motion.

For long term simulations symplectic integrators are required to conserve phase space behaviour. For  $(p, q)$  canonical variables we can write middle step symplectic algorithm as

$$q^j = q^{j-1} + \nabla_p H\left(\frac{p^j + p^{j-1}}{2}, \frac{q^j + q^{j-1}}{2}\right) dt, \quad (2.50)$$

$$p^j = p^{j-1} - \nabla_q H\left(\frac{p^j + p^{j-1}}{2}, \frac{q^j + q^{j-1}}{2}\right) dt, \quad (2.51)$$

where  $H(p, q)$  is the Hamiltonian of the system [33].

For simulations the non relativistic Lorentz force equation(2.1) , was discretised in three point scheme Figure 2.10 shows an example in a single dimension.

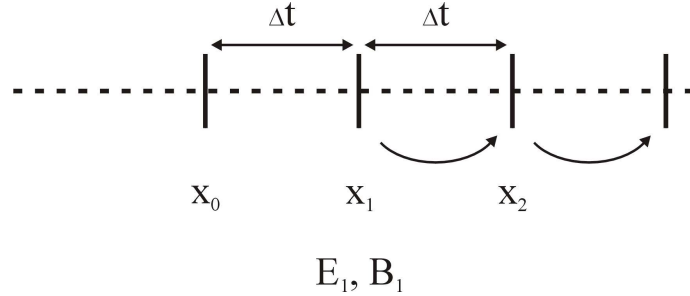


Figure 2.10: Three point scheme for discrete time evolution.

To avoid the singularity at  $r = 0$ , positions in toroidal coordinates were transformed into cartesian coordinates. Taking  $x_0$  and  $x_1$  as known positions,  $E$  and  $B$ , the electric and magnetic fields at position  $x_1$ , and taking  $x_2$  the position to be calculated, the discrete equation of motion in three dimensions can be written as,

$$\begin{aligned} m \frac{x_2 - 2x_1 + x_0}{\Delta t^2} &= qE_x + q \left( \frac{y_2 - y_0}{2\Delta t} B_z - \frac{z_2 - z_0}{2\Delta t} B_y \right), \\ m \frac{y_2 - 2y_1 + y_0}{\Delta t^2} &= qE_y + q \left( \frac{z_2 - z_0}{2\Delta t} B_x - \frac{x_2 - x_0}{2\Delta t} B_z \right), \\ m \frac{z_2 - 2z_1 + z_0}{\Delta t^2} &= qE_z + q \left( \frac{x_2 - x_0}{2\Delta t} B_y - \frac{y_2 - y_0}{2\Delta t} B_x \right). \end{aligned} \quad (2.52)$$

Rearranging the terms we get ,

$$\begin{aligned}
\left(\frac{m}{\Delta t^2}\right) x_2 + \left(\frac{-qB_z}{2\Delta t}\right) y_2 + \left(\frac{qB_y}{2\Delta t}\right) z_2 &= \left(\frac{m}{\Delta t^2}\right) (2x_1 - x_0) + qE_x + q\left(\frac{-y_0B_z}{2\Delta t} + \frac{z_0B_y}{2\Delta t}\right), \\
\left(\frac{qB_z}{2\Delta t}\right) x_2 + \left(\frac{m}{\Delta t^2}\right) y_2 + \left(\frac{-qB_x}{2\Delta t}\right) z_2 &= \left(\frac{m}{\Delta t^2}\right) (2y_1 - y_0) + qE_y + q\left(\frac{-z_0B_x}{2\Delta t} + \frac{x_0B_z}{2\Delta t}\right), \\
\left(\frac{-qB_y}{2\Delta t}\right) x_2 + \left(\frac{qB_x}{2\Delta t}\right) y_2 + \left(\frac{m}{\Delta t^2}\right) z_2 &= \left(\frac{m}{\Delta t^2}\right) (2z_1 - z_0) + qE_z + q\left(\frac{-x_0B_y}{2\Delta t} + \frac{y_0B_x}{2\Delta t}\right).
\end{aligned} \tag{2.53}$$

thus

$$\begin{aligned}
x_2 + \left(\frac{-qB_z\Delta t}{2m}\right) y_2 + \left(\frac{qB_y\Delta t}{2m}\right) z_2 &= (2x_1 - x_0) + \frac{qE_x\Delta t^2}{m} - q\left(\frac{y_0B_z - z_0B_y}{2m}\right) \Delta t, \\
\left(\frac{qB_z\Delta t}{2m}\right) x_2 + y_2 + \left(\frac{-qB_x\Delta t}{2m}\right) z_2 &= (2y_1 - y_0) + \frac{qE_y\Delta t^2}{m} - q\left(\frac{z_0B_x - x_0B_z}{2m}\right) \Delta t, \\
\left(\frac{-qB_y\Delta t}{2m}\right) x_2 + \left(\frac{-qB_y\Delta t}{2m}\right) y_2 + z_2 &= (2z_1 - z_0) + \frac{qE_z\Delta t^2}{m} - q\left(\frac{x_0B_y - y_0B_x}{2m}\right) \Delta t.
\end{aligned} \tag{2.54}$$

With  $x_2, y_2, z_2$  the three unknowns and three equations represent a linear matrix equation system,

$$\begin{pmatrix} a_{11} & a_{12} & a_{13} \\ a_{21} & a_{22} & a_{23} \\ a_{31} & a_{32} & a_{33} \end{pmatrix} \begin{pmatrix} x_2 \\ y_2 \\ z_2 \end{pmatrix} = \begin{pmatrix} b_1 \\ b_2 \\ b_3 \end{pmatrix}. \tag{2.55}$$

Thus writing determinants in the form

$$D_1 = \begin{vmatrix} b_1 & a_{12} & a_{13} \\ b_2 & a_{22} & a_{23} \\ b_3 & a_{32} & a_{33} \end{vmatrix}, D_2 = \begin{vmatrix} a_{11} & b_1 & a_{13} \\ a_{21} & b_2 & a_{23} \\ a_{31} & b_3 & a_{33} \end{vmatrix}, D_3 = \begin{vmatrix} a_{11} & a_{12} & b_1 \\ a_{21} & a_{22} & b_2 \\ a_{31} & a_{32} & b_3 \end{vmatrix}. \tag{2.56}$$

with ,

$$D_0 = \begin{vmatrix} a_{11} & a_{12} & a_{13} \\ a_{21} & a_{22} & a_{23} \\ a_{31} & a_{32} & a_{33} \end{vmatrix} \neq 0, \tag{2.57}$$

the solution is given by Cramer's rule,

$$x_2 = \frac{D_1}{D_0}, \tag{2.58}$$

$$y_2 = \frac{D_2}{D_0}, \tag{2.59}$$

$$z_2 = \frac{D_3}{D_0}. \tag{2.60}$$

## 2.2.4 Efficiency of simulation code

The efficiency of any simulation code depends on the number of parameters used such as, programming style, hardware, compiler, errors and tolerance acceptability. Figure 2.11 shows the behavior of relative error in electric field calculation. The

electric field was calculated for homogeneously distributed particle beam using Gauss' Law and compared with their numerical value. The error number of grid points is an important parameter as the space-charge forces have to be resolved. When grid points are too low, higher particle number will be weighted at same value leading to so called *mesh effect* or numerical heating. On the other hand, a higher number of grid points cause excessive computational time.

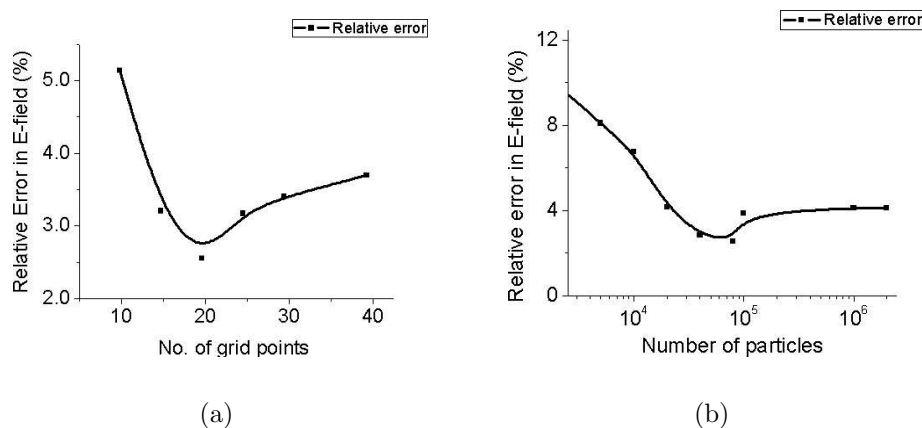


Figure 2.11: (a) Error due to number of grid points at constant particle number  $N_p = 10000$  (b) Error due to number of particles at constant *gridpoints* =  $50 \times 50 \times 50$ .

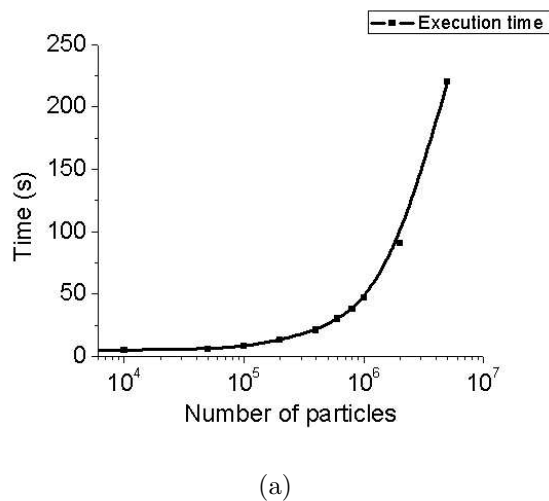


Figure 2.12: Time for a single time step calculation as function of particle number.

It is often inconvenient to define a large number of particles which may cause long time on Desktop computer. Therefore, the number of particles should be matched with requirements. So we define less number of particles assigning a

*macro* charge to each particle, but a certain minimum number of macro particles must be defined in order to maintain a reasonable particle to grid point ratio. As can be seen in figure 2.11(b) for homogenous distribution, when number of particles are very low the error in electric field is high. It reaches minima at a certain level and stays constant after a certain value as *homogeneity* is reached. Figure 2.12 shows the time required for a single step. Thus defining around 60,000 particles is reasonable for given grid points. For above used settings 3D space charge routine takes approximately 6 *seconds* every time step.



# Chapter 3

## Transport in a single toroidal segment

Simulations were performed to investigate the beam transport properties in toroidal magnetic fields. The code incorporates the multi particles multi specie simulations with real field (magnetic or electric) configuration. A desired type of the field source, in this case current carrying coils, was simulated to take into account the fringe fields. Direct comparisons were made between analytical, simulated and measured properties of the beam. Simulations, spanning a large range of theoretically possible parameters, used to probe the beam transport in a single toroidal segment.

### 3.1 The geometry and input parameters for simulations

The external magnetic field values at grid points were calculated using the Biot-Savart law. A toroidal mesh was defined with a central axis of arc radius  $1.3\text{ m}$ , and a minor radius  $0.1\text{ m}$  (see figure 3.1). The numerical mesh was chosen to be a  $35^\circ$  toroidal arc, so that fringe fields from toroidal segments can be taken into consideration. The arc angle of  $5^\circ$  (in fringe field region) corresponds to a distance of  $135\text{ mm}$  on the axis. The output plane was set at the last coil position.

The homogeneous phase-space distribution was generated to investigate beam properties. The chosen distribution allows us to generate maps for beam matching condition in a single segment. For the theoretical investigation proton beam was chosen due to its low vertical drift. An energy range  $4\text{ keV} - 20\text{ keV}$  with the magnetic field strengths  $0.4 - 0.6\text{ T}$  was simulated. Beam energy of  $10\text{ keV}$  and a magnetic field of  $0.6\text{ T}$  was taken as standard setting which gives moderate drift and intensity for experiments. For positive charged particles, the  $\mathbf{R} \times \mathbf{B}$  drift is vertical, i.e. perpendicular to the ring plane.

Figure 3.2 shows an example of magnetic field distribution used at mesh points. The field gradient in the radial direction of  $0.42\text{ T/m}$  was simulated at the centre for  $480\text{ A}$  current that corresponds to magnetic field of  $0.6\text{ T}$  maximum on the axis.

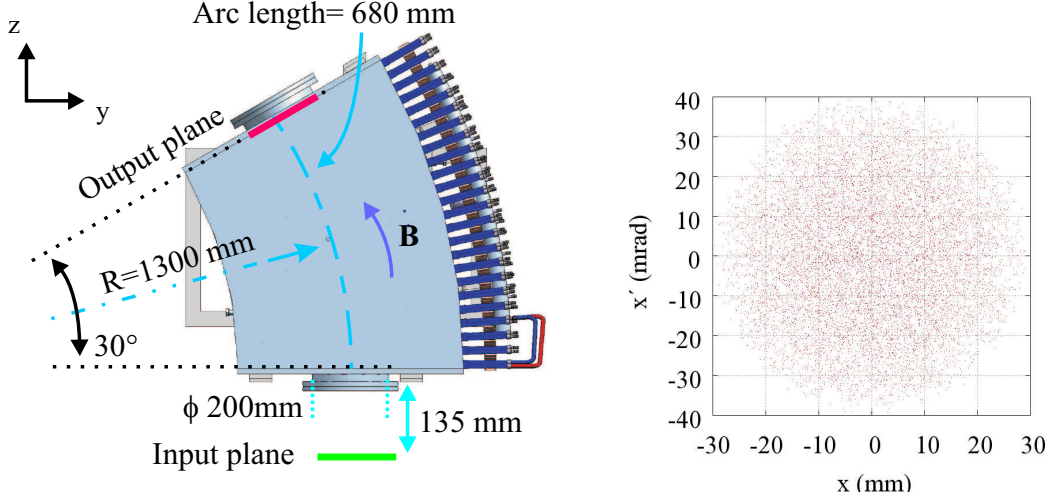


Figure 3.1: Scheme for simulation (left) and input phase-space distribution for mapping technique (right).

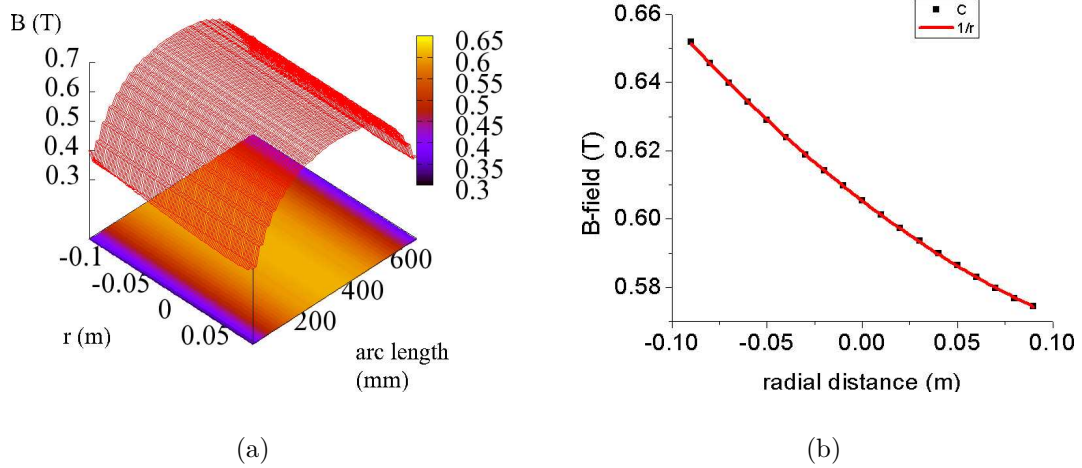


Figure 3.2: 3-dimensional toroidal field distribution over the mesh (left) and graph of magnetic field strength in radial direction at middle plane of the segment (right).

### 3.2 Analysis parameter *velocity ratio* ( $v_\lambda$ ) and a mapping technique

In accelerator physics phase-space (also called *trace-space*) distribution is generally used to analyze beam properties. On the  $y$ -axis, angle  $\tan^{-1}(p_\perp/p_\parallel)$  is plotted against position on  $x$ -axis. Where  $p_\parallel$  is taken parallel to the longitudinal geometrical axis for every particle. This is shown schematically in Figure 3.3. To describe the intrinsic dependence of canonical momentum on magnetic fields additional variable is needed to describe properties of the beam.

The parameter *velocity ratio* was defined as

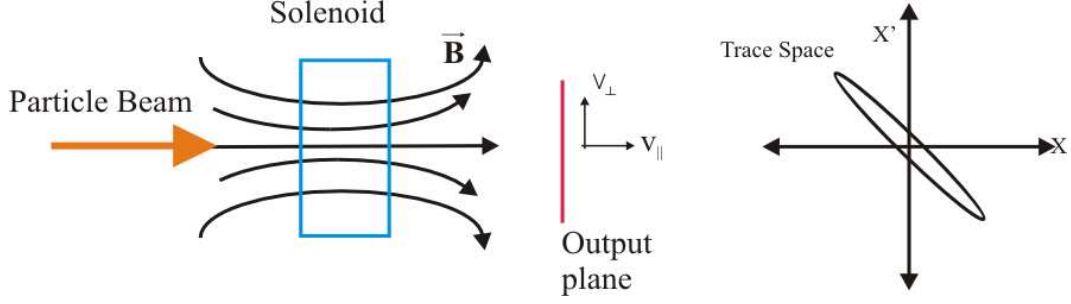


Figure 3.3: Trace space (phase-space) for linear system. In this case phase space at output plane is not containing information of canonical momentum in magnetic fields.

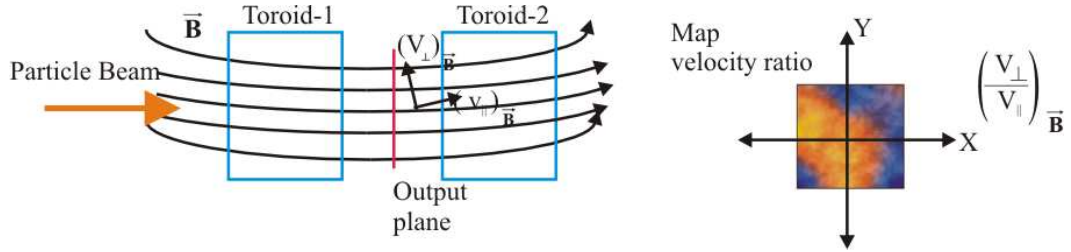


Figure 3.4: Figure explaining to  $v_\lambda$  factor. Both components of velocities,  $v_\parallel$  and  $v_\perp$ , are defined with respect to magnetic field lines at the position of particle. Hence the "guidance" property is integrated in 3-dimensional map.

$$velocity\ ratio = v_\lambda = \left( \frac{v_\perp}{v_\parallel} \right)_{\mathbf{B}}, \quad (3.1)$$

where  $v_\parallel$  is defined as a velocity component parallel to the magnetic field at a particular position and magnetic field strength distribution as shown in figure 3.4.

This parameter was especially defined to show the beam guidance along field lines and is important with respect to the variation in magnetic field strength  $|\mathbf{B}|$ . We are interested in beam like particle distribution. Therefore the condition  $v_\lambda < 0.1$  was adapted with respect to the injection experiments. Particle inside the interval  $[0, 0.1]$  will be depicted as a "good beam". Mapping technique was used to find the emittance required for maximum **transmission** or **injection efficiency**.

The homogeneous distribution in  $x - x'$  of a beam is mapped and particles satisfying  $v_\lambda < 0.1$  at the output plane gives information regarding optimal injection for a given system. The map of  $v_\lambda$  in  $x - y$  plain depicts the "good beam" condition as shown in Figure 3.5.

To investigate beam properties in terms of  $v_\lambda$ , histograms were produced. The number of particles against velocity ratio was plotted. The *peak velocity ratio* and *Full Width at Half Maximum (FWHM)* was defined with respect to the histogram as shown in Figure 3.6. Then the beam distribution is optimal when the  $v_\lambda$  at peak and the FWHM both have a minimum value.

The *injection efficiency* or *transmission function*  $T(v_\lambda)$  was defined with

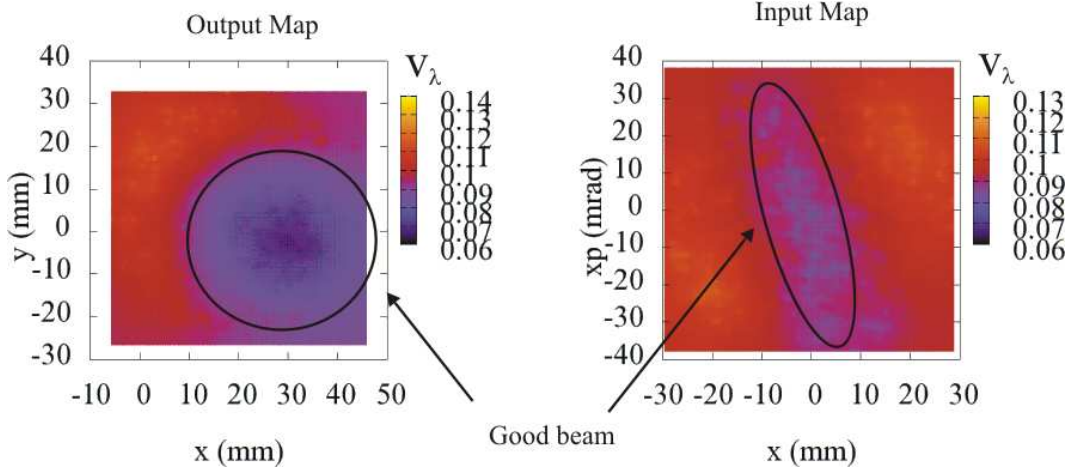


Figure 3.5: The graph depicting "good beam" case. The figure on the right shows the ellipse definition for "good beam".

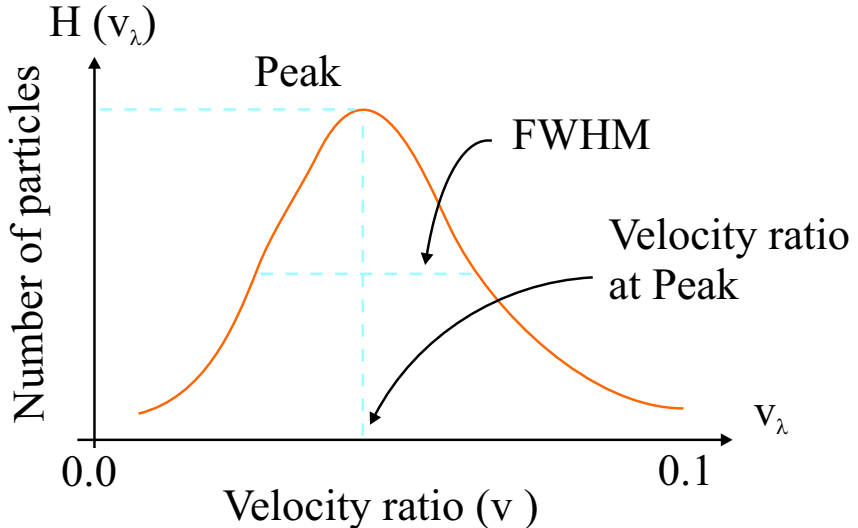


Figure 3.6: Explanation to histogram of  $v_\lambda$ . The best case occurs when a maximum number of particles show  $v_\lambda$  values below a given limit, and with an acceptable spread in  $v_\lambda$ .

respect to  $v_\lambda$  as,

$$T(v_\lambda) = \frac{\text{No. of particles at output plane with } v_\lambda < 0.1}{\text{Total No. of particles injected}}. \quad (3.2)$$

The **velocity factor** ( $v_f$ ) which can also be called *good core factor* was defined as

$$v_f = \frac{1}{v_\lambda(H_{max}) \times FWHM \text{ of histogram}(H)}. \quad (3.3)$$

FWHM can be translated to give the transversal beam temperature. Beam emittance in terms of ellipse area is defined as

$$\epsilon_x = x_{max}(x'_{max}). \quad (3.4)$$

This definition was not used as output beam property since  $x$  and  $y$  momenta are coupled in magnetic fields. But this property was used to find the matched case at the input plane.

### 3.3 Analytical calculation for the proton beam

Tables (3.1 & 3.2) show the analytical calculation for single particle dynamics (proton) in a toroidal magnetic field. Vertical drift is calculated for the arc length of 0.815  $m$ . Important numbers can be calculated by using following formulae.

$$\begin{aligned} \text{Longitudinal velocity } v_{\parallel} &= \sqrt{\frac{2qV}{m}} \\ \text{Gyration Period } T &= \frac{2\pi m}{qB} \\ \text{Time of Flight } TOF \ \Delta t &= s/v_{\parallel} \\ \text{Drift velocity } v_R &= \frac{mv_{\parallel}^2}{qBR}; \text{ drift } \Delta l = v_R \times \Delta t = \frac{smv_{\parallel}}{qBR} \\ \text{no. of osci } ^n &= \Delta t/T = \frac{sqB}{2\pi mv_{\parallel}} \end{aligned} \quad (3.5)$$

The velocity  $v_{\parallel}$  can be calculated from extraction potential  $V$ , which determines the time of flight ( $TOF$ ) for given a given distance 's' (e.g. 0.815  $m$ ). Number of oscillations can be calculated as dividing  $TOF$  by gyration periods ( $T$ ). The number of oscillations corresponds to the gyration along  $\mathbf{B}$  field lines. Beam size can be calculated by taking the sinusoidal function of the oscillation number.

Table 3.1: Proton motion along the 30° toroid at 10keV beam energy

Magnetic field (T)	Drift (mm)	No. of osci.
0.400	22.58	3.60
0.425	21.25	3.83
0.450	20.00	4.05
0.475	19.01	4.28
0.500	18.06	4.50
0.525	17.20	4.73
0.550	16.42	4.95
0.575	15.71	5.18
0.600	15.05	5.40

From Table (3.1) one can see that the maximum magnetic field is required for minimum vertical drift. Table (3.2) shows that minimum drift occurs at low energy end. For maximum magnetic field, the vertical shift is 9.51  $mm$  at 4  $keV$ . For higher energies drift is higher. In 10  $keV$  case, the drift is good enough to resolve it from the beam size.

Table 3.2: Proton motion along the 30° toroid at constant magnetic field of 0.6 T

Energy (keV)	4.0	5.0	6.0	7.0	8.0	9.0
Drift (mm)	9.51	10.64	11.65	12.59	13.46	14.28
No.of osci.	8.54	7.64	6.98	6.46	6.04	5.70
Energy (keV)	10.0	11.0	12.0	13.0	14.0	15.0
Drift (mm)	15.05	15.79	16.49	17.16	17.81	18.43
No. of osci.	5.40	5.15	4.93	4.74	4.57	4.41
Energy (keV)	16.0	17.0	18.0	19.0	20.0	
Drift (mm)	19.03	19.62	20.19	20.75	21.29	
No.of osci.	4.27	4.14	4.03	3.92	3.82	

### 3.4 Single particle simulation

To investigate single particle dynamics, consider a single particle (proton) injected into the toroidal magnetic field, on the toroidal axis. Figure 3.7(a) shows the behavior of  $v_\lambda$  and the gyro radius as a function of energy.

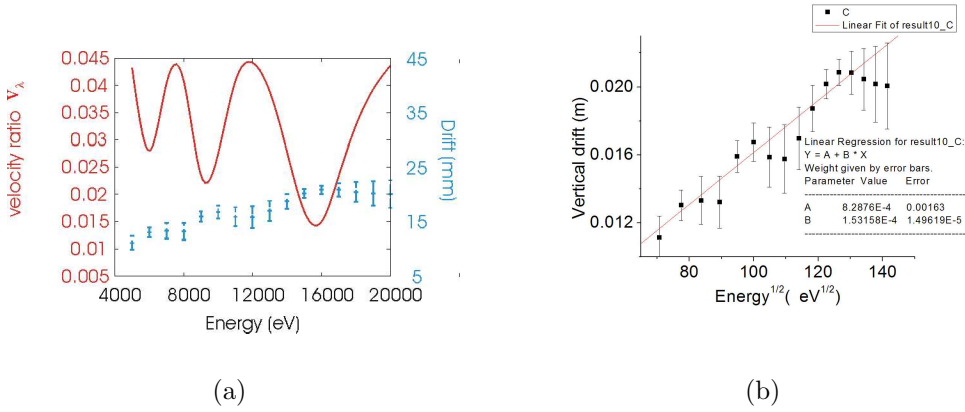


Figure 3.7: Left: Velocity ratio  $v_\lambda$  as a function of energy at the toroid output plane (red curve)(see figure 3.1) with vertical position (blue) at output plane. Oscillations in curve are mainly due to gyration. Right: Vertical drift of proton beam plotted with Larmor radius as errorbars against beam velocity.

One can see in figure 3.7(a) that the peaks and valleys in the graph coincide with energy for which the number of oscillation tends towards integral value. Only at 18 keV, the peak is shifted by 2 keV. When a singly charged particle is injected into a toroidal magnetic field it gyrates around a field line with a guiding centre drifting vertically. Due to the curved nature of the magnetic field in toroidal segment, there will be always some transversal impulse at the output plane, that results in non-zero  $v_\lambda$  parameter. To determine the absolute drift the vertical drift was plotted with gyro radius as error bars. For given arc length  $s$ , the vertical ( $\mathbf{R} \times \mathbf{B}$ ) drift of the particle is given by,

$$\Delta l = \frac{ms}{qBR} v_\parallel. \quad (3.6)$$

$\nabla\mathbf{B}$  drift vanishes due to low  $v_{\perp}$  velocity. Thus for a proton the ratio  $\Delta l/\sqrt{E}$  is a constant equal to  $1.504 \times 10^{-4} m(eV)^{-1/2}$ .

The plot of the vertical deflection of proton with gyro radius as error bar against the root of energy is shown in the figure 3.7(b). The slope of the graph is  $1.53 \times 10^{-4} \pm 0.15 \times 10^{-4} m(eV)^{-1/2}$ , which is in a good agreement with the analytical calculation.

## 3.5 Simulations of proton beam with multi particles

### 3.5.1 Beam properties with energy variation

To investigate the multi particle behavior of a system, a parallel beam of proton with 30 mm radius and  $\pm 5$  mrad angular width was injected into the single segment. In this case 10 keV with 2 mA beam current was chosen. At the output plane, drift and beam size were calculated with respect to  $v_{\lambda}$ .

Figure shows an example of beam envelop of proton beam at 10 keV transported through toroidal magnetic field (0.6 T). Four focal points can be observed along the toroidal beam path.

Figure 3.9(a) shows a dependence of vertical drift position on energy. As seen from figure 3.9(b) the beam size varies in the range of  $\sim 2 - 4$  cm. Graph depicts beam focus at 8 keV and 14 keV. At the same position the drift curve falls down with the value equal to this variation. Thus a drift curve can be seen as a smooth function of energy.

Transmission function was calculated with respect to the  $v_{\lambda}$  (see figure 3.9(c)). Due to the higher impulse at higher energy the number of trapped particles is lower, and transmission function is higher. Magnetic field was 0.6 T set. Maximum beam size with minimum losses are of interest when dynamics for multiturn injection is investigated.

The plot of peak value of  $v_{\lambda}$  for a beam is shown in figure 3.10(a). Due to fringe fields a large momentum spread was observed at lower energies. Figure 3.10(b) shows higher FWHM values at the lower energy end. The fluctuations characterize the phase of the beam.  $v_f$  is the inverse function of peak value and FWHM. To find the optimum case the velocity factor  $v_f$  was plotted shown in figure 3.10(c). As seen from the graph, the matched case occurs at 14 keV. A focused proton beam was simulated in this case.

One explains this phenomena by comparing the analytical value. At 14 keV a beam waist is calculated with respect to near half integer oscillation number. When the number of oscillations is a half or full integer minima and maxima of beam size are seen. In the case of higher energies the effect of fringing fields will be lower hence improving the  $v_f$  factor.

### 3.5.2 Beam properties at various input distributions

From figure 3.9(c) one infers that at operating energy of 10 keV the maximum injection efficiency (transmission) is as low as 64%. But it was found that the beam distribution or input phase, at the input plane can be chosen to improve value of transmission function. With the help of a focussing element one chooses the input phase-space distribution. To find the optimum case the input ellipse was

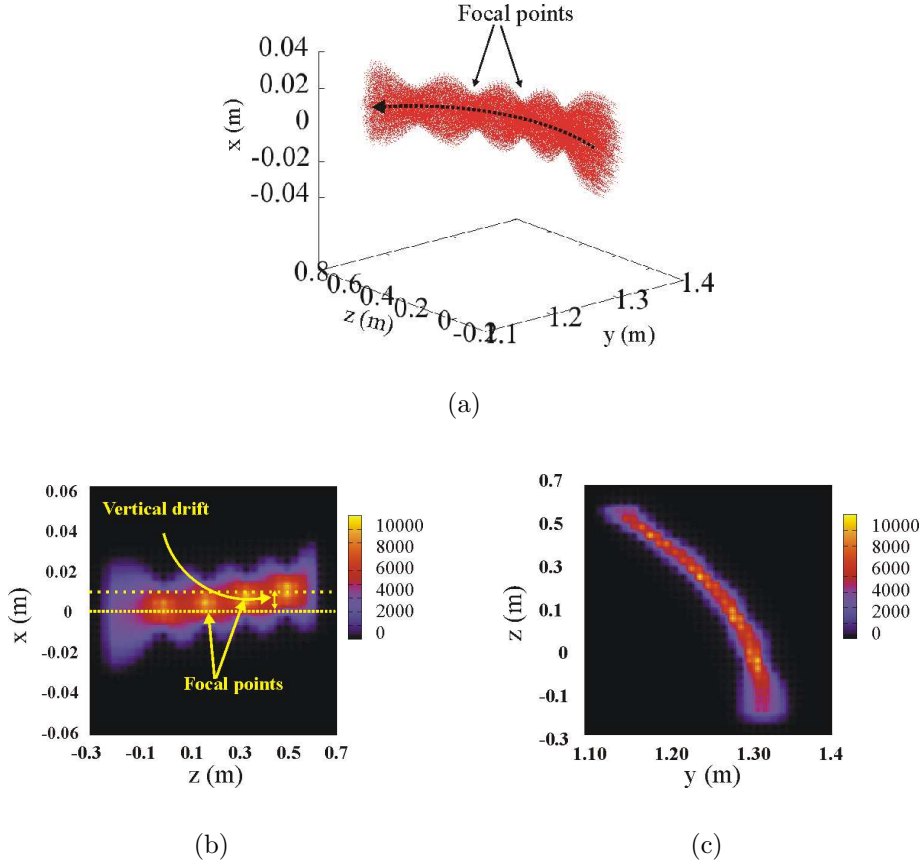


Figure 3.8: (a) An example of 3-dimensional particle beam (proton beam at  $10\text{ keV}$ ) transported through toroidal magnetic field of  $0.6\text{ T}$ . Four focal points are seen along the beam path. (b) Density profile mapped on  $x - z$  plane. Vertical drift of beam is indicated. (c) Density profile mapped on  $y - z$  plane shows  $30^\circ$  arc along the beam path.

rotated in  $x - x'$  plane. Ellipse angle  $0^\circ$  and  $180^\circ$  represents a parallel input beam and  $90^\circ$  represents a focused input beam. A  $10\text{ keV}$  beam with  $2\text{ mA}$  current was simulated in a magnetic field of  $0.6\text{ T}$ .

As seen from figure 3.11, matched case occurs when a focused beam is injected into toroidal field giving 100% transmission. The acceptance of the system at standard settings was estimated to  $400\pi\text{ mm mrad}$

With respect to the magnetic field, acceptance is variable but the ellipse angle is almost constant within range of  $100$  to  $120^\circ$ . A homogeneous beam in 4-dimensional space was injected into a toroidal magnetic field. When the output  $v_\lambda$  was plotted as a function of input parameters  $x - x'$  one produces graphs as shown in figure 3.12. One can see that, the maximum transmission, the blue region, occurs when a beam with an ellipse angle around  $115^\circ$  is injected.

It can also be noticed from figure 3.12 that at some of the magnetic field levels an off axis injection is required for maximum transmission. This shift is in the range of  $10\text{ mm}$ . In the graphs the  $x -$  axis is the vertical axis. The  $\mathbf{R} \times \mathbf{B}$  force causes a drift in vertical direction. Thus the additional vertical momentum gain (a kick) from curved magnetic field lines is required to minimize the drift effect. This



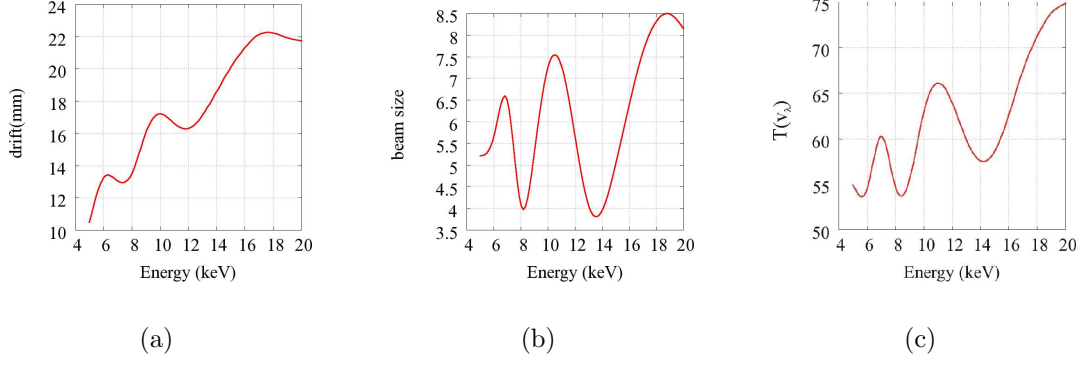


Figure 3.9: (a) Vertical position of the proton beam as a function of beam energy, (b) beam size in centimetre shows a dominance of a gyration motion, (c) transmission variation as function of energy, at output plane.

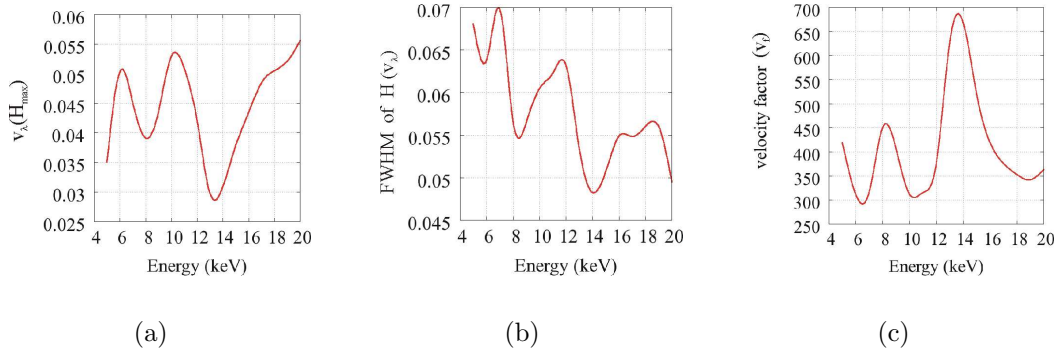


Figure 3.10: (a) Max. abundant  $v_\lambda$ , (b) FWHM variation and (c)  $v_f$  as function of energy for focused proton beam input.

explains the necessity of off axis injection at input plane for matching condition.

### 3.5.3 Beam properties with variable magnetic field

The beam can be guided well at higher magnetic fields. For simulations parallel beam with energy  $10\text{ keV}$  was injected for which the maximum transmission value is 63%. The drift curve shows an inverse dependence on a magnetic field. The vertical drift decreases with increasing magnetic fields, as seen in Figure 3.13(a). Transmission function increases with higher field levels (see figure 3.13(b)).

Figure(3.14) shows output particle distribution mapped according to  $v_\lambda$ . Here the defined  $x$ - axis corresponds to the vertical axis of curvature. As seen the beam drifts in horizontal  $y$ - axis as well. These simulations were performed at a constant ellipse injection angle was kept constant at  $0^\circ$ .

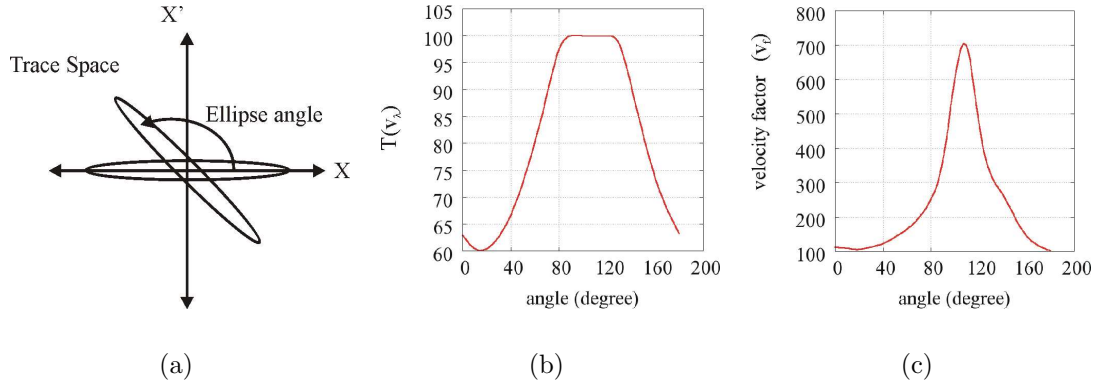


Figure 3.11: Transmission and  $v_f$  as function of ellipse angle.

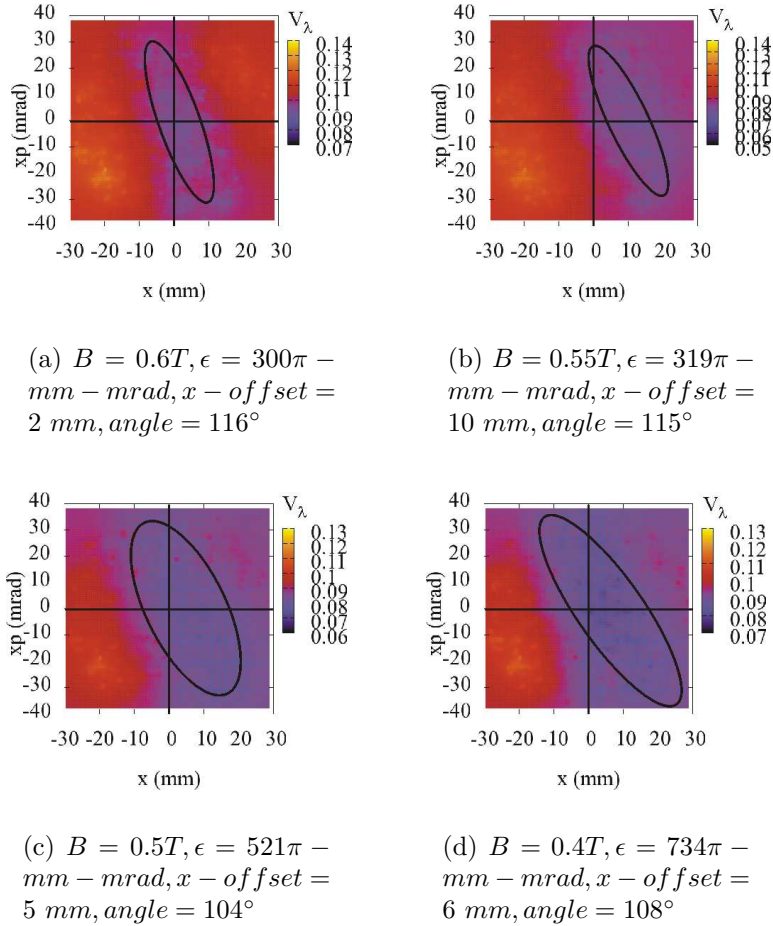


Figure 3.12: The map of  $v_\lambda$  against **input** trace space. The  $x$ -axis is vertical axis. The blue region gives the acceptance for particular magnetic field, the beam energy is  $10 keV$ .

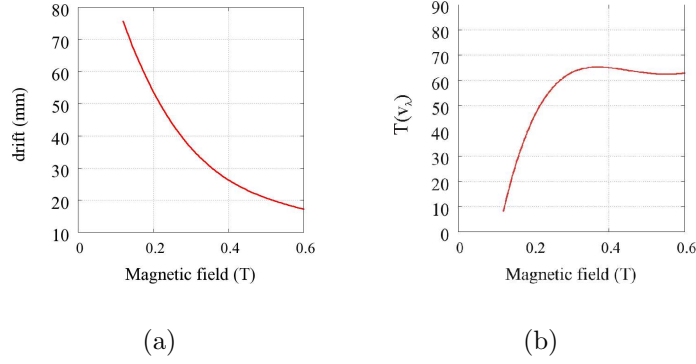


Figure 3.13: Vertical drift (in  $mm$ ) and transmission function (in  $\%$ ) as a function of toroidal magnetic field.

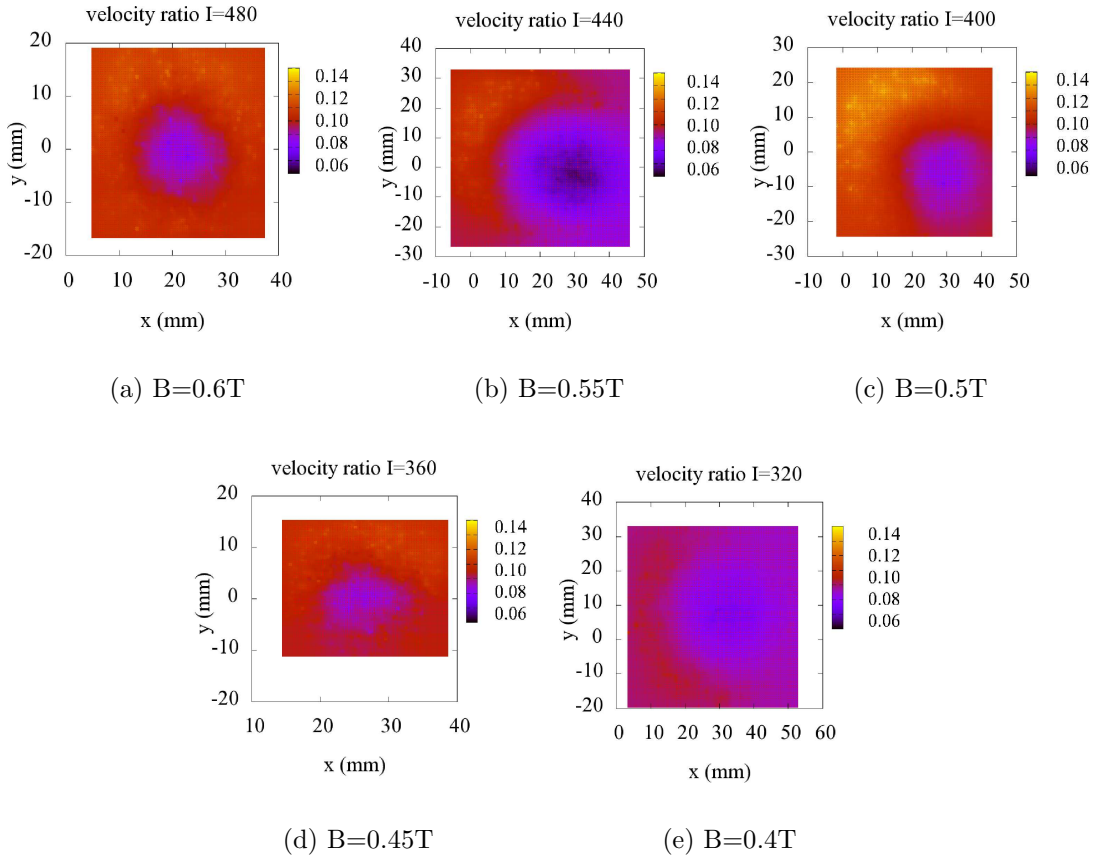


Figure 3.14: Map of  $v_\lambda$  against **output**  $x - y$  space. The blue region shows "good beam" at different magnetic fields with constant beam energy  $10\ keV$ . Ellipse injection angle was kept constant at  $0^\circ$ .

### 3.5.4 Effect of self fields

The Brillouin limit sets the theoretical limit on the maximum charge that can be transported into a magnetic field. To investigate the effects of self fields and

study the effects of Brillouin limit, a parallel proton beam with  $10\text{ keV}$  energy was injected into the magnetic field of  $0.6\text{ T}$ .

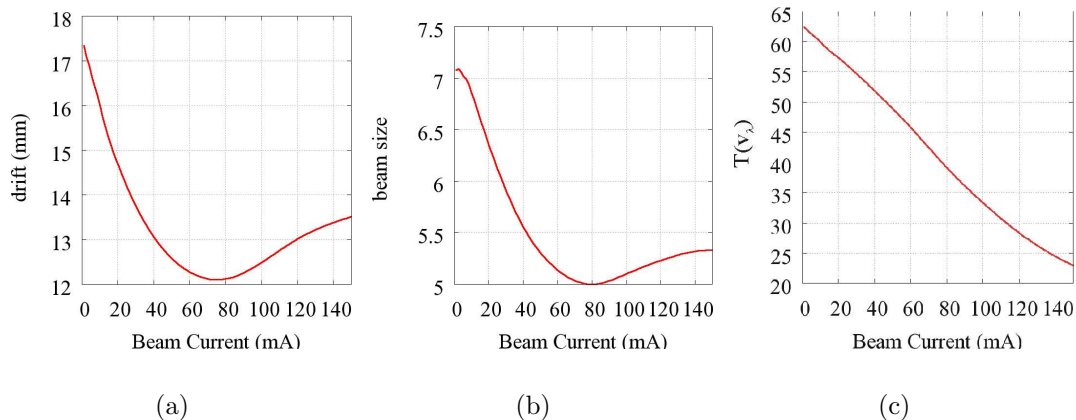


Figure 3.15: Simulated drift of beam (in  $mm$ ), beam size (in  $cm$ ) at **output** and transmission function (in  $\%$ ) variation as function of beam current at constant energy  $10\text{ keV}$  and magnetic field  $0.6\text{ T}$ .

Figure 3.15(a) shows that, the vertical drift decreases as a function of increasing current. Decreasing nature is observed till the current reaches the Brillouin limit which was  $80\text{ mA}$  in this case. This behavior has been experimentally observed [34]. A small influence of space-charge on the vertical drift was also observed in single segment transport experiments. Figure 3.15(b) shows the beam size as a function of the current. Lower than Brillouin limit particles are well guided by magnetic field. At higher self fields the electrostatic energy forces the particle to leave trajectory. Figure 3.15(c) shows that, transmission always decreases with additional self fields.

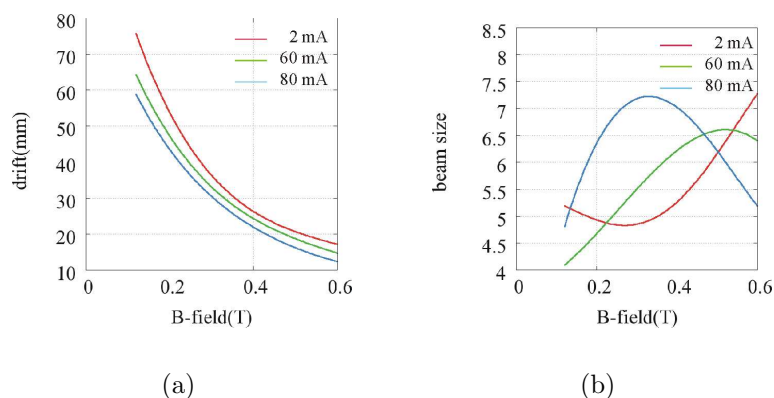


Figure 3.16: Simulated drift (in  $mm$ ) and beam size (in  $cm$ ) as function of magnetic field for different currents.

Figure 3.16 compares the behavior of vertical drift and beam size for three different cases  $2\text{ mA}$ ,  $60\text{ mA}$  and  $80\text{ mA}$ . At higher magnetic fields the drift does

not vary significantly, to dominate the change in beam size. The beam size as well changes in the same range.

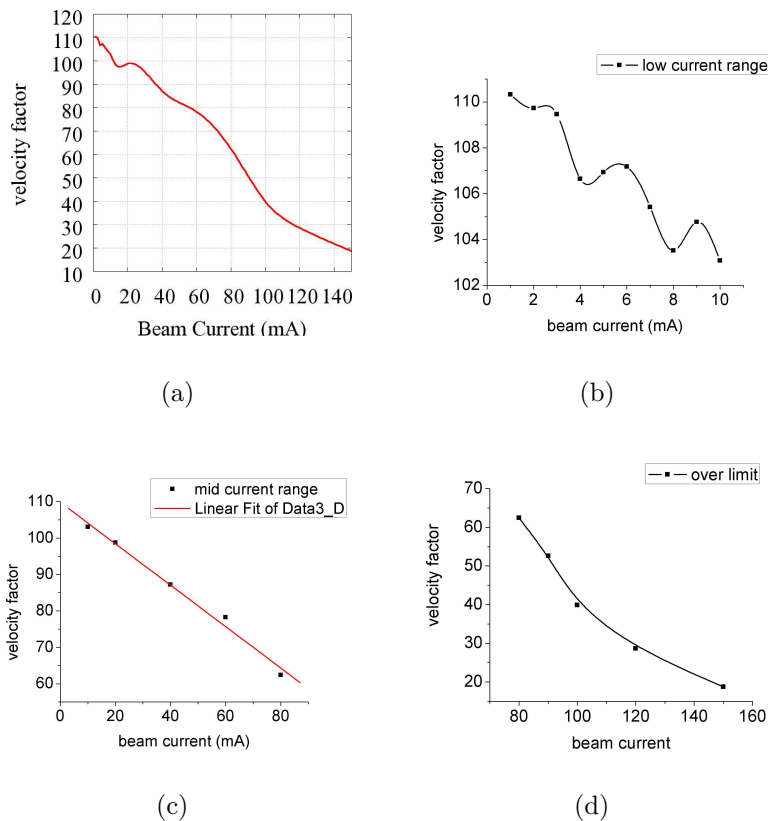


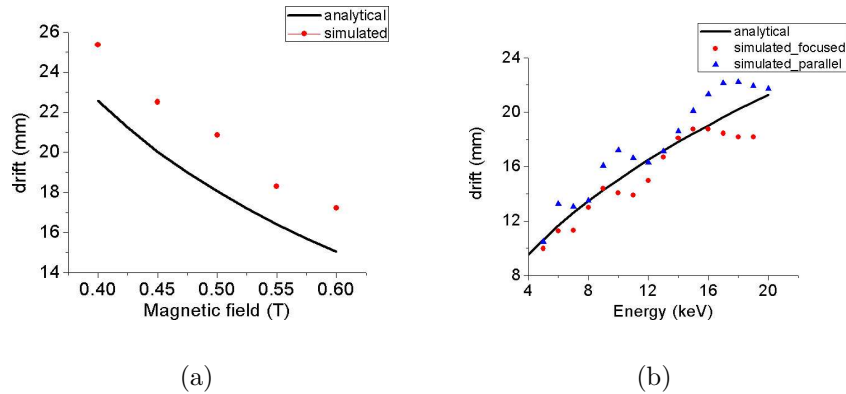
Figure 3.17: Velocity factor as function of beam current at three different scales of beam current. (a) full scale, (b) (0, 10  $mA$ ) range, (c) (10, 80  $mA$ ) range, (d) (80, 160  $mA$ ) range. Parallel proton beam was injected in toroidal field of 0.6  $T$ .

Figure 3.17(a) shows the plot of velocity factor  $v_f$  as a function of the beam current. The plot shows three distinct regions. Figure 3.17(b) shows that, at low currents, the  $v_f$  follow non functional behavior which corresponds to analytical beam size function. In the middle range figure 3.17(c),  $v_f$  is linear function of current. Above the Brillouin flow electrostatic energy overcomes magnetic energy and  $v_f$  rapidly falls down as seen in figure 3.17(c). In this case the magnetic field was defined at the maximum value of 0.6  $T$ .

Our experimental parameters lie at lower limit ends. The figure 3.16 shows that the system exhibit different nature for lower and higher current region, although the drift is shown to have same effect. In the case of 2  $mA$  beam current, the Brillouin limit lies at 0.015  $T$ . At this field level the drift is too high to detect the beam.

### 3.6 Comparison with analytical values

Figure 3.18 compares simulated values with the analytically calculated ones. For simulations a parallel beam with  $2\text{ mA}$  current was chosen. Figure 3.18(a) shows the drift as a function of the magnetic field. The analytically calculated values are almost  $2\text{ mm}$  higher than the simulated. The beam size is much larger than this difference. The deviation from analytical values can be reasoned as the effect of non-homogeneous fields.



---

Figure 3.18: (a) Drift as a function of the magnetic field. Black line is the analytical curve whereas red points are simulated, (b) vertical position as function of energy for two different input phase-space. Red points are for the focused beam, whereas blue points are for the parallel beam. Magnetic field was  $0.6\text{ T}$ .

Figure 3.18(b) shows the effect of input distribution. The vertical drift was plotted as a function of energy. The parallel beam experiences more drift than the focused beam.

For these simulations, a homogeneous distribution of particles was used. This analysis provides a theoretical basis for injection simulations. For precise calculations of the injection system experimentally measured distributions were required.

# Chapter 4

## Experiments

### 4.1 Characterization of Ion Source

The hot filament ion source was built to obtain an ion beam for beam transport experiments. The choice of volume type ion source was made due to stable operation, good emittance and to the existing experience of IAP [35]. A characterization of the source performance was required in terms of beam emittance, current and ion species. In the case of multi species, e.g. from hydrogen gas, the proton fraction that can be extracted depends on plasma properties. According to former measurements, with this type of ion source a maximum proton fraction of 40% can be expected [37].

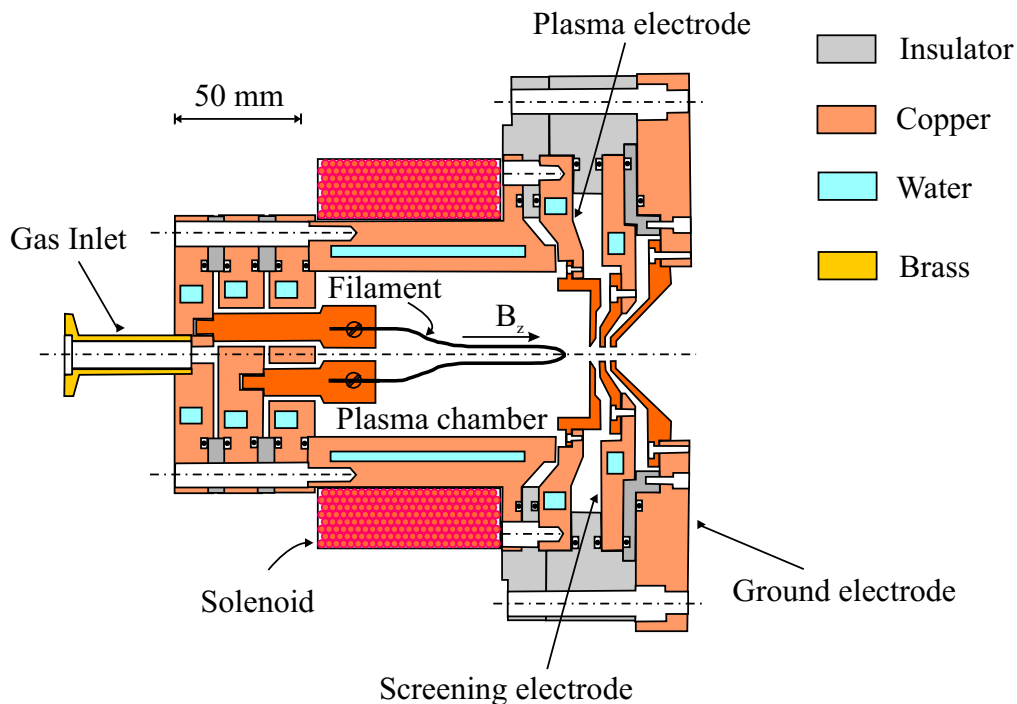


Figure 4.1: Cross sectional view of the ion source.

As shown in Figure 4.1 the source consists of a plasma chamber with heating filament and triode extraction system (see photograph A.11 in appendix). The

cathode is heated to emit electrons which are accelerated to the plasma chamber wall. Electrons are forced into cycloidal paths by an external solenoidal field, increasing their path lengths to the wall, thereby, increasing the probability of an ionizing collision with neutrals. The magnetic field produced by the solenoid was measured by a Hall Probe. As seen from Figure 4.2 about 40% of the maximum field level is present at extraction system. It was possible to produce  $0 - 23 \text{ mT}$  magnetic field at centre of plasma chamber by varying the coil current in range  $0 - 6 \text{ A}$ . The heating filament as well produces a comparable magnetic field around  $9 \text{ mT}$  which is heated by current of  $50 - 60 \text{ A}$ . This magnetic force does not have significant effect on ion beam, but does change plasma properties significantly.

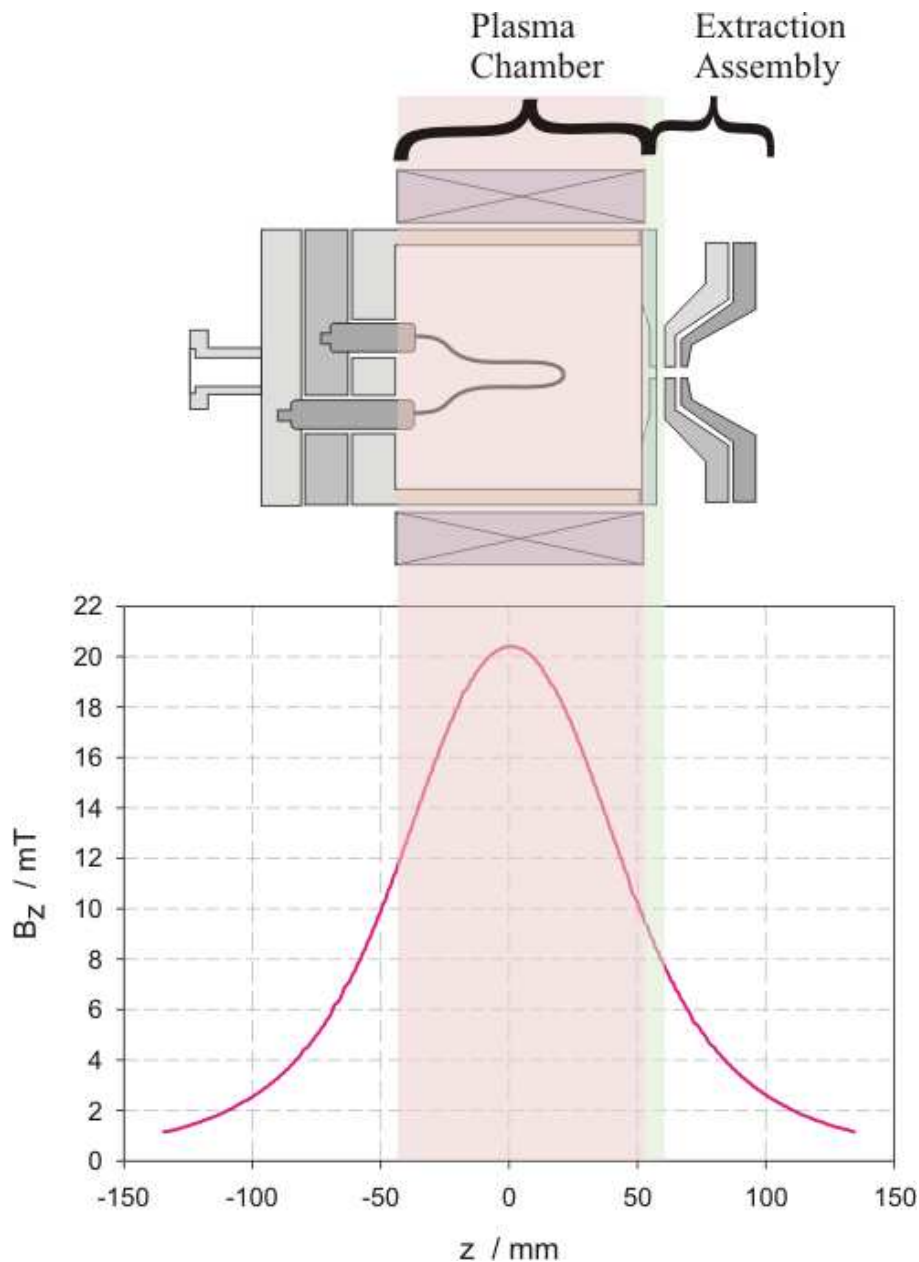


Figure 4.2: Magnetic Field from coils on plasma chamber.

A triode extraction system was used. The plasma electrode is held at positive potential, the screening electrode is held at negative potential at about 10% value



of the plasma electrode voltage and followed the ground electrode. Figure 4.3 shows a block diagram of circuit and source. The space charge dominated beam current is given by the Child Langmuir Law,

$$J = \frac{1}{9\pi} \sqrt{\frac{2e}{m}} \frac{V^{3/2}}{d^2}. \quad (4.1)$$

Where  $J$  is the current density,  $V$  is accelerating potential and  $d$  is the acceleration gap length. In the used source,  $d$  was 5 mm. Figure 4.4 shows the

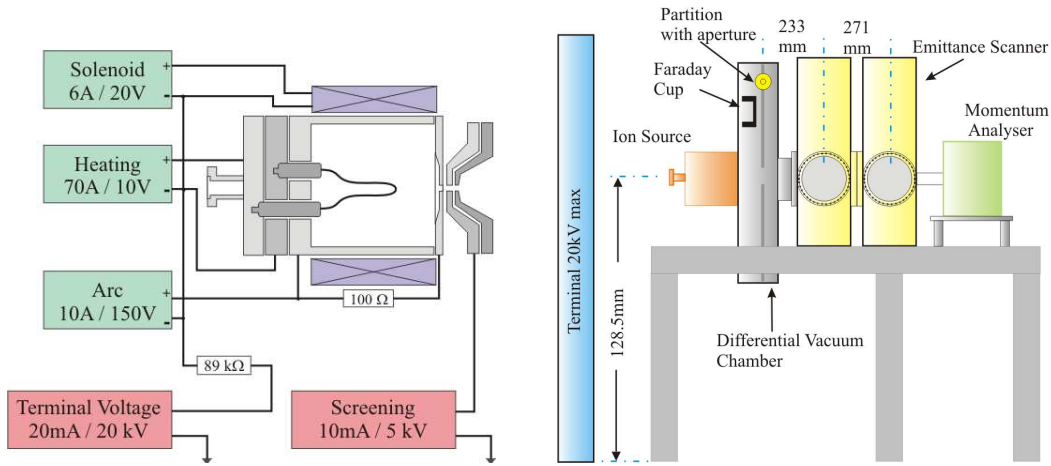


Figure 4.3: Circuit diagram and experimental test bench.

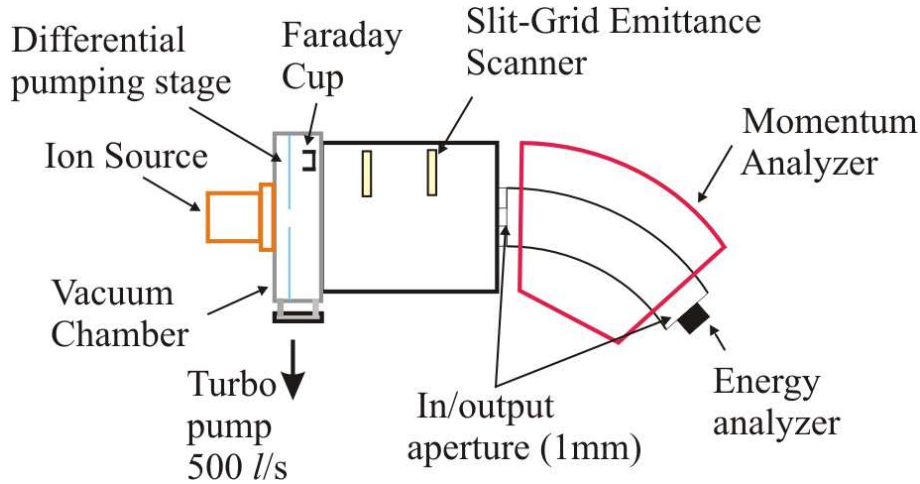


Figure 4.4: Top view of experimental test bench.

experimental setup used for characterization of ion source (see photograph A.12 in appendix). The source was mounted on differential pumping chamber with three turbo molecular pumps. Faraday cup was installed in the same tank for beam current measurements. Emittance scanner of grid slit type was mounted and further downstream of it a momentum analyzer (dipole magnet) was installed.

## Emittance Scanner and Beam parameters

To measure the phase-space distribution of ion beam an emittance scanner of slit grid type was used. The slit and grid are moved vertically by step motor to intercept the beam. The slit is moved in steps to record the signal on grid. Thus giving the distribution of particles in  $x - x'$ . The beam transport is characterized

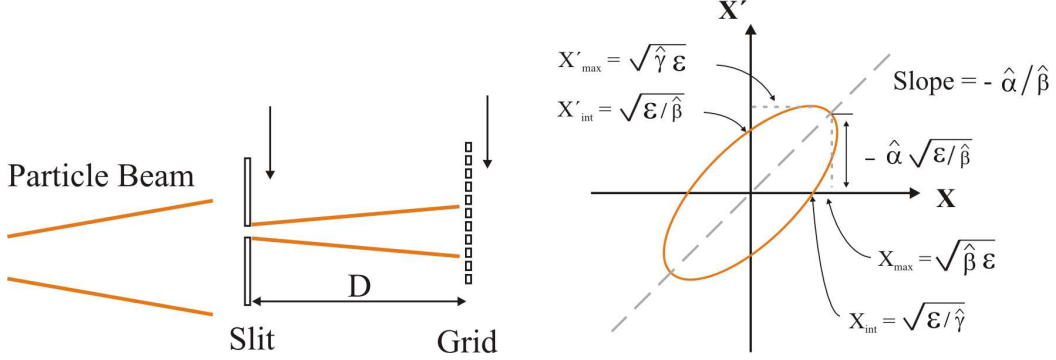


Figure 4.5: Slit and grid arrangement for emittance measurements (left). Twiss parameters and relationship with beam size and angle (right).

by transport parameters  $\hat{\alpha}$ ,  $\hat{\beta}$  and  $\hat{\gamma}$ . Also called the twiss parameters [38]. From these parameters the beam size and divergence angle can be determined. Their relations are schematically shown in figure 4.5.

The quality of the extracted beam is given by its *emittance*. The emittance is defined in terms of the area occupied by particles in phase-space.

$$\epsilon_x = \int \int dx dx'. \quad (4.2)$$

More precisely, the *rms emittance* is used to study the behavior of an ion distribution. In  $x - x'$ , it is defined as,

$$\tilde{\epsilon}_x = \left( \overline{x^2 x'^2} - \overline{x x'}^2 \right)^{1/2}, \quad (4.3)$$

or equivalently,

$$\tilde{\epsilon}_x = \tilde{x} \frac{\tilde{v}_{x,th}}{v_0}. \quad (4.4)$$

The factor  $\tilde{v}_{x,th}$  defines the transversal distribution to be random, thermal, or kinetic.

The another important variable *brightness* is defined as [36],

$$B = \frac{2I}{\pi^2 \epsilon_x \epsilon_y}. \quad (4.5)$$

### 4.1.1 $He^+$ beam

From  $He$  gas ion beam with the fourth lowest mass can be extracted. The helium beam consists of singly charged ion beam for used source type. So the ion source properties can be easily investigated.

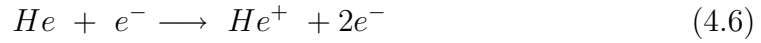


Figure 4.6 shows an example of a 1.2 mA  $He^+$  beam extracted at 9.2 keV. 9.0 mTorr gas filling pressure was used as standard settings.

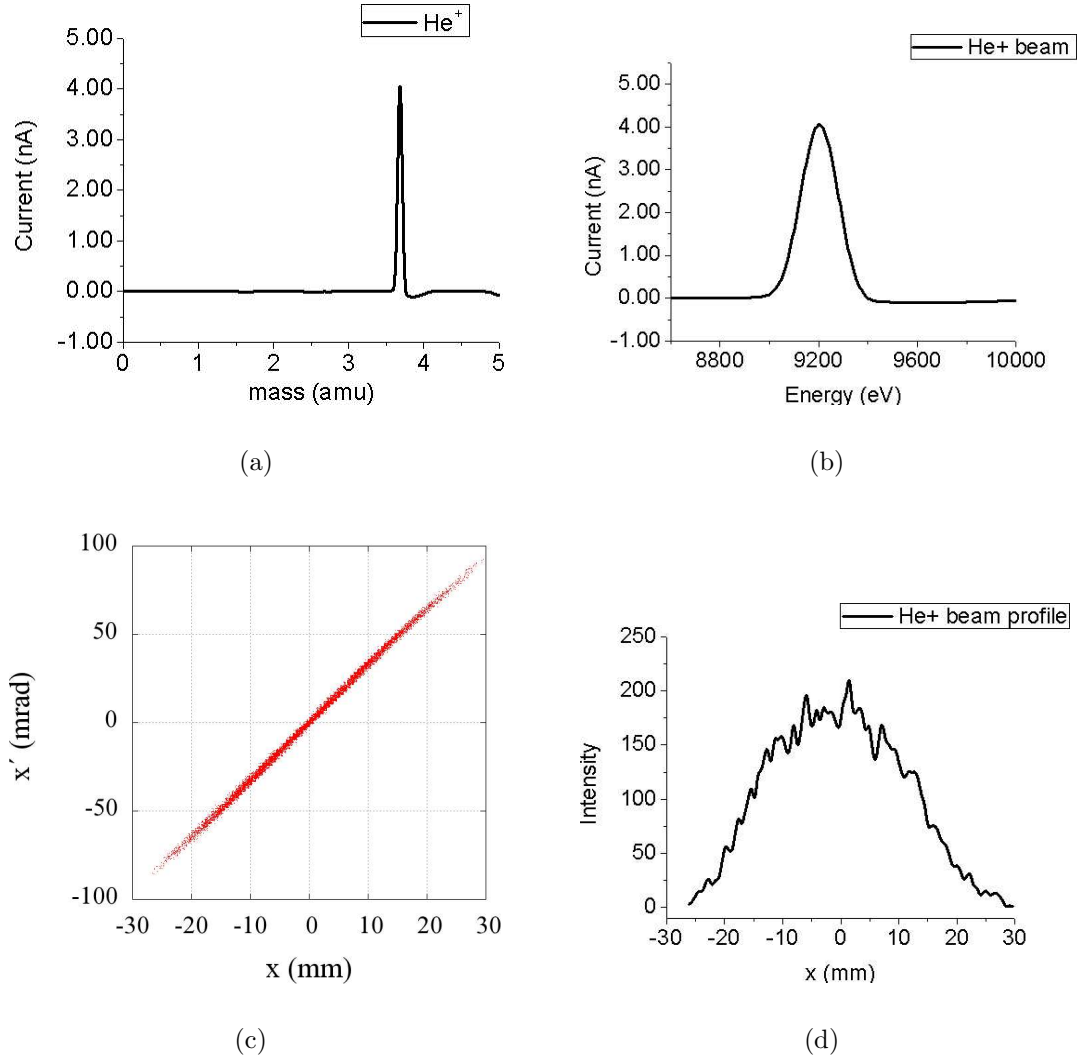


Figure 4.6: (a) Graph showing the single specie of mass 4  $amu$  (a shift in mass scale is due to calibration of mass 1  $amu$  at 10  $keV$ ), (b) Energy Spectra with energy spread  $\pm 100$   $eV$ , (c) the phase-space distribution measured using emittance scanner  $\epsilon_{rms} = 3.94 \times 10^{-2} mm - mrad$ , and (d) beam profile along transverse direction.

The terminal that was used can supply voltages up to 20  $kV$ . The beam current measured by Faraday cup ( $I - fc$ ) is plotted against energy. As seen in figure 4.7(a) at more than 9  $keV$  beam energy the beam current stays constant even when the

extraction current is increased. The excess of current is lost in the extraction gap. Figure 4.7(b) shows maximum transmission at 7 keV.

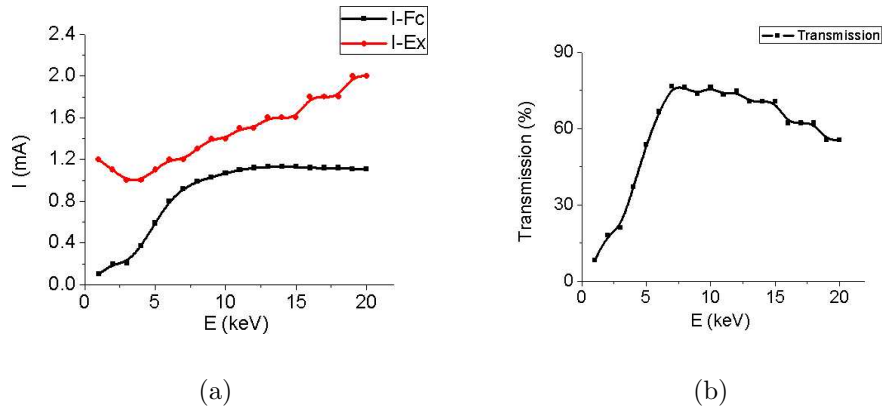


Figure 4.7: (a) Current-Energy curve for  $He^+$  beam, and (b) transmission curve showing matched case at 7 keV.

The source operation parameters define the plasma or especially the *plasma meniscus*. As shown in figure 4.8 the matched concave meniscus gives maximum extraction current. The current was measured as function of filling pressure,

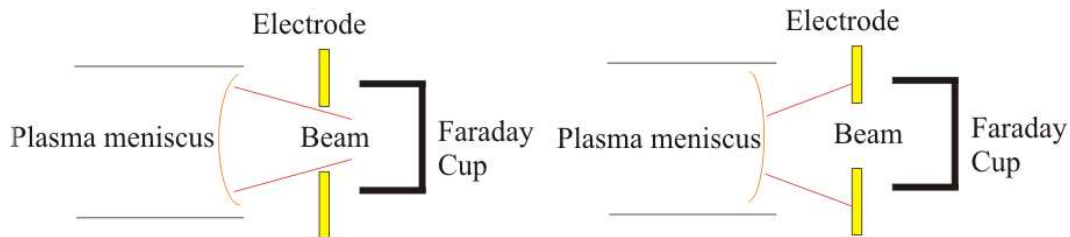


Figure 4.8: Effect of plasma *meniscus* on beam current. The concave shape in shown figure gives more current than convex.

solenoidal field, arc voltage and arc current shown in figure 4.9. The gas filling pressure does not show any significant effect on the beam current in Faraday cup. The variation of the solenoidal field shows maxima at particular settings. As the arc voltage is increased the beam current increases and reaches a maximum at 80 V. This also represents the fact that electron impact on  $He$  have maximum cross section at 80 eV. The arc current is related to plasma density. Thus the beam current is increased at increasing plasma density.

The matched beam is reached when a maximum current is extracted with maximum brightness and minimum emittance. This optimal setting was used for experiments (see figure 4.10).

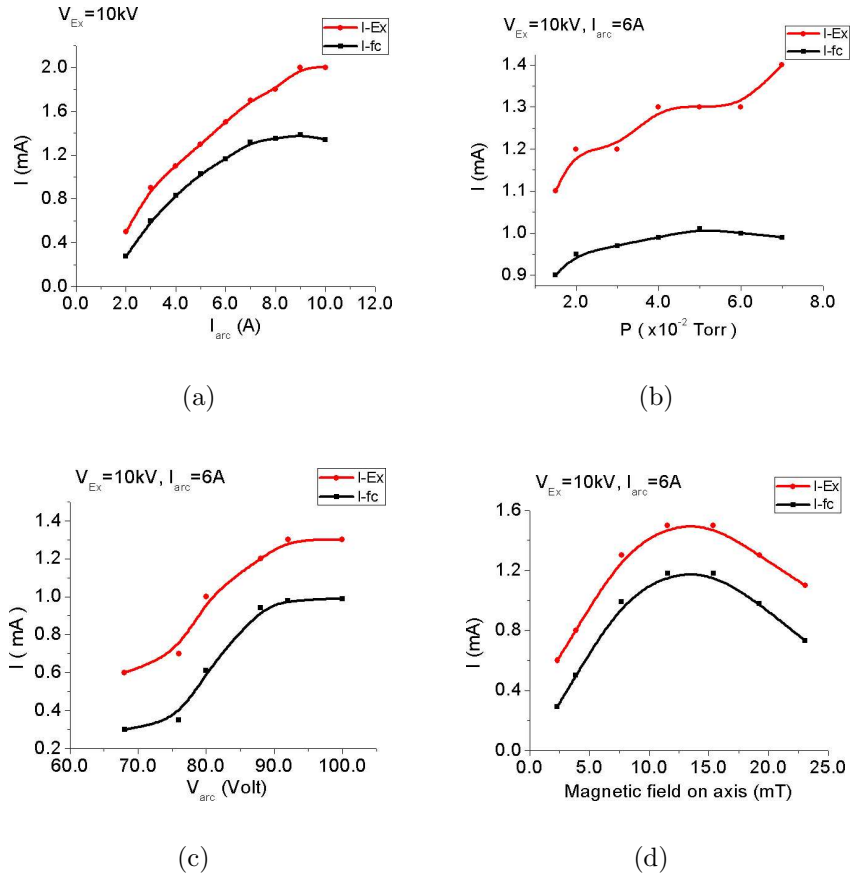


Figure 4.9: (a) Beam current as a function of arc current ( $I_{arc}$ ), (b) beam current as a function of filling pressure ( $P$ ) (c) beam current as a function of arc voltage ( $V_{arc}$ ), and (d) beam current as a function of magnetic field maximum magnetic field on axis.

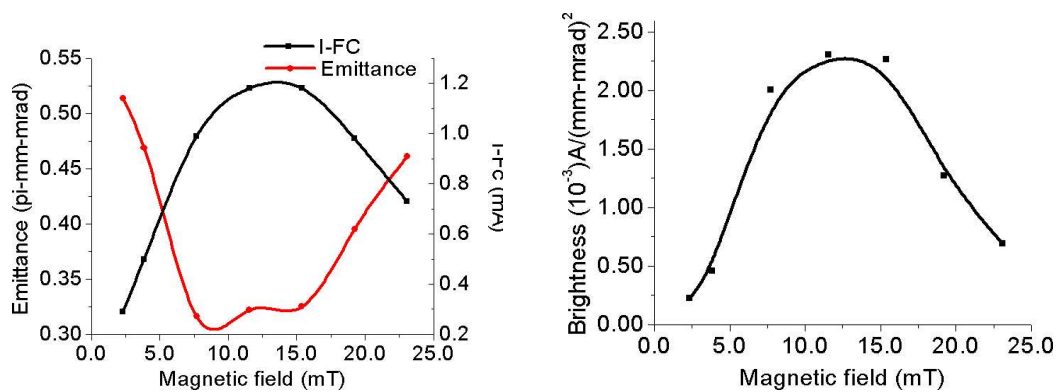
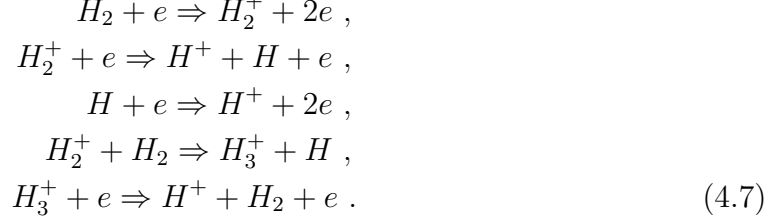


Figure 4.10: Variation of emittance and brightness as function of magnetic field showing the optimized case at 15.0 mT.

### 4.1.2 Proton beam

From Hydrogen gas proton beam with a lowest mass can be extracted along with  $H_2^+$  and  $H_3^+$  fractions. The proton beam is extracted by ionization of hydrogen gas. The key reactions involved are,



It is believed that the last two processes are important for an efficient production of protons [37]. Figure 4.11 shows an example of mixed proton beam at the energy of  $9.2 \text{ keV}$  with beam current  $2.2 \text{ mA}$ . It shows a relatively high amount of  $H_2^+$  and  $H_3^+$  fractions at normal plasma parameter setting.

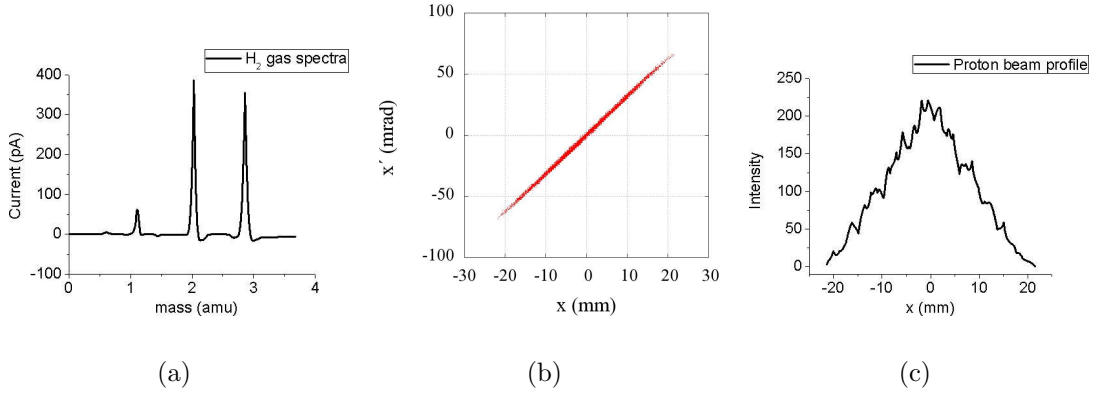


Figure 4.11: (a) Graph showing the three fractions of mass  $m = 1, 2$  and  $3 \text{ amu}$ , (b) the phase-space distribution measured using emittance scanner  $\epsilon_{rms} = 8.45 \times 10^{-2} \text{ mm} - \text{mrad}$ , and (c) beam profile along radial direction.

It was figured out that the proton fraction depends upon plasma parameters. Thus the whole parameter space of arc current ( $I_{arc}$ ) and magnetic field was scanned at four different values of arc potential ( $V_{arc}$ ) and three different values of filling pressure ( $P$ ) to find maximum proton fraction. To get the clear contrast in the plots let the relative occurrence ( $r_{occ}$ ) of particular specie (e.g. for  $H^+$ ) be defined as

$$r_{occ} H^+ = \frac{\eta_{H^+}}{\eta_{H_2^+} + \eta_{H_3^+}}, \tag{4.8}$$

where  $\eta$  is percent fraction of the specie. Similar way, the relative occurrence for  $H_2^+$  and  $H_3^+$  was defined. Figure 4.12 shows the relative occurrence of  $H^+$ ,  $H_2^+$  and  $H_3^+$  as function of arc current ( $I_{arc}$ ) and solenoidal current ( $I_{sol}$ ) at filling pressure of  $1.2 \times 10^{-2} \text{ mbar}$  and  $80 \text{ V}$  arc potential. At particular value of magnetic

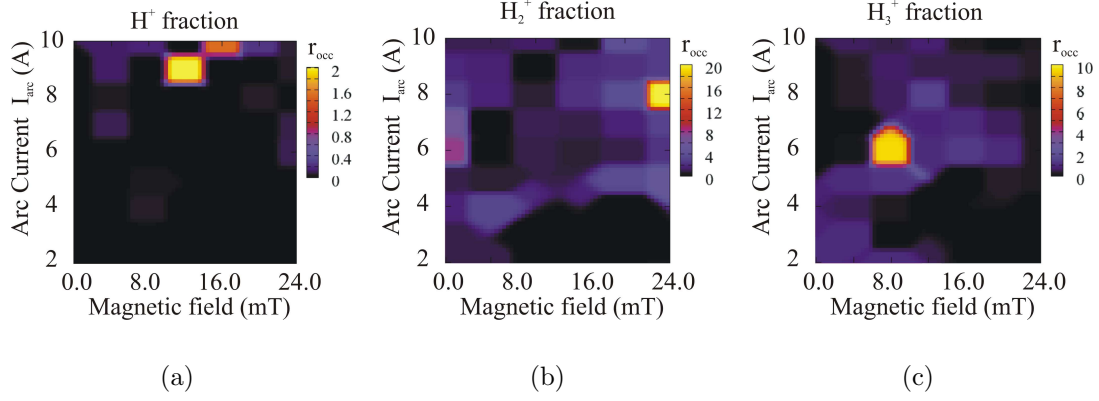


Figure 4.12: Graph of relative occurrence of (a)  $H^+$ , (b)  $H_2^+$ , and (c)  $H_3^+$ .

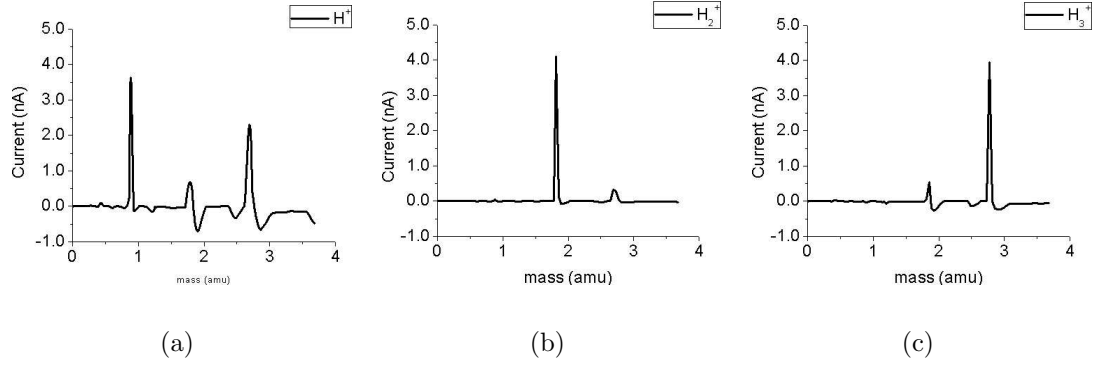


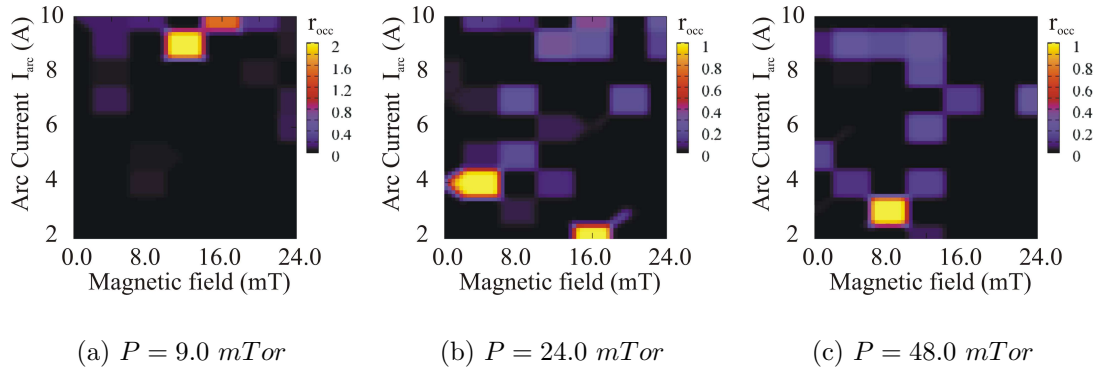
Figure 4.13: Graph of mass spectra of  $H^+$ ,  $H_2^+$ , and  $H_3^+$  at the position of island with respect to figure 4.12. Beam energy was held constant at  $9.2 \text{ keV}$ .

field and plasma density the relative occurrence of particular specie is very high. Thus the graph shows *island* kind structure.

Figure 4.13 shows the mass spectra at the optimum values of relative occurrence. It was seen at each of the separate optimum settings i.e. at position of *island*,  $\sim 58\%$  of proton fraction with  $3.04 \text{ mA}$  current,  $\sim 91\%$  of  $H_2^+$  fraction with  $2.84 \text{ mA}$  current and  $\sim 95\%$  of  $H_3^+$  fraction with  $3.05 \text{ mA}$  current was extracted at beam energy of  $9.2 \text{ keV}$ .

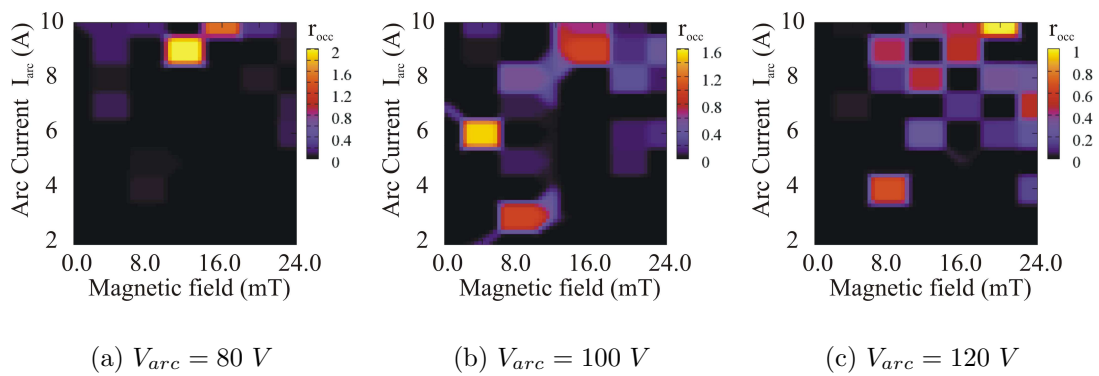
When these graphs were plotted for different filling pressure (see figure 4.14) or arc potentials (see figure 4.15) the peaks were observed to shift and intensity decreasing while retaining the island structure.

The maximum of  $58\%$  proton fraction with  $3.08 \text{ mA}$  at  $10 \text{ keV}$  energy can be successfully extracted from ion source at optimum settings. These were used for the further experiments.




---

Figure 4.14: Graph of relative occurrence of proton fraction for different gas filling pressure at constant arc potential  $80 \text{ V}$ .




---

Figure 4.15: Graph of relative occurrence of proton fraction for different arc potentials at constant gas filling pressure  $1.2 \times 10^{-2} \text{ mbar}$ .



## 4.2 Solenoidal Transport

An additional focussing element is required for transport of charged particle beam that can provide the required phase-space distribution. Solenoid was proposed on the merit of simple operation, cylindrical symmetry and availability. Figure 4.16 shows the setup used to measure the phase-space distribution (see photograph A.13 in appendix). The ion source was mounted on vacuum chamber which was connected to the solenoid. Downstream of solenoid the emittance scanner was installed. Table (4.1) lists some of the important physical properties of focussing solenoid used in experiments.

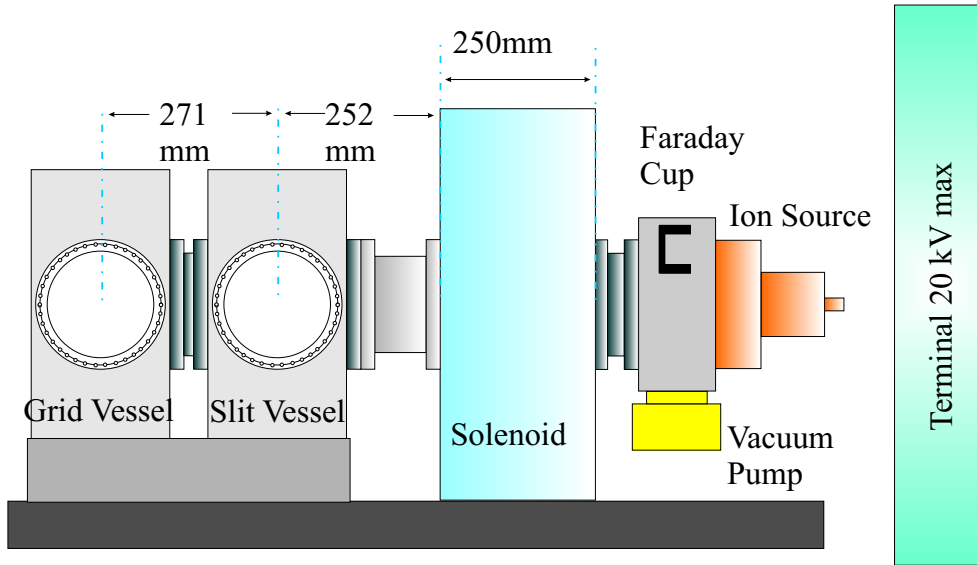


Figure 4.16: Schematic setup for solenoidal transport.

Table 4.1: Physical properties of Solenoid

No. of winding	280
Maximum Magnetic on axis field	0.72 T
Maximum Voltage and Current	32.5 V, 360 A
Length	250 mm
Diameter of aperture	106 mm
Magnetic Shielding	present

The focussing strength of a solenoid is given by [36],

$$k = \left( \frac{q^2 B^2}{8mW} \right)^{1/2}, \quad (4.9)$$

where  $B$  is magnetic field,  $W$  is the energy of beam and  $q$  is charge of the particle. The focal length is directly proportional to the magnetic field strength, and inversely proportional to the squareroot of mass.

### 4.2.1 Simulations with measured data

For simulation code a  $B_z$  component of magnetic field was measured as function of transversal and longitudinal space ( $r - z$ ). The 3d magnetic field distribution then can be completed using Maxwell's equations, namely

$$\nabla \cdot \mathbf{B} = 0. \quad (4.10)$$

For beam transport calculation the measured distribution was used. The one dimensional particle distribution was transformed in two dimensional phase-space distribution and back calculated at the point of ion source (see figure 4.17).

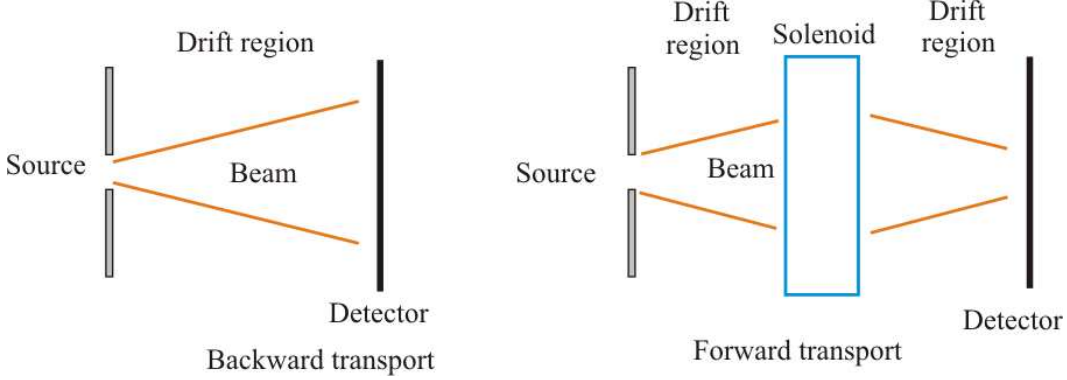


Figure 4.17: The phase-space distribution measured was transformed back till the aperture at extraction of source. And this back calculated distribution was used for forward transport through the solenoid.

The space-charge compensation degree was determined by matching the beam radius with aperture at source extraction.

In the case of proton beam three fractions are present. The space-charge forces for single specie were simulated by using concept of *perveance*. The perveance of the beam is given as,

$$K = \frac{1}{4\pi\epsilon_0} \sqrt{\frac{m_i}{2q}} \frac{I}{V^{3/2}}. \quad (4.11)$$

The space charge forces of beam is said to be equal when perveance of every species is equal. At optimal setting, single specie of  $H^+$  beam was calibrated to  $6.67 \text{ mA}$ ,  $H_2^+$  beam was calibrated to  $4.40 \text{ mA}$ ,  $H_3^+$  beam was calibrated to  $3.85 \text{ mA}$  at  $9.2 \text{ keV}$  energy.

### 4.2.2 $He^+$ beam transport through solenoid

When  $He^+$  beam was transported though solenoid, two distinct distributions are detected; a neutral beam distribution uninfluenced by magnetic field and deflected singly charged  $He^+$  beam. Figure 4.18(a) and 4.18(b) shows the distribution simulated and measured respectively, at solenoid current  $I = 150 \text{ A}$  for beam energy  $8 \text{ keV}$ . Offset is observed due to misalignment of solenoid with respect to beam axis.

Figure 4.18(c) shows two distributions overlapped. The error is around 23% in emittance measured and simulated. An additional error due to neutral beam

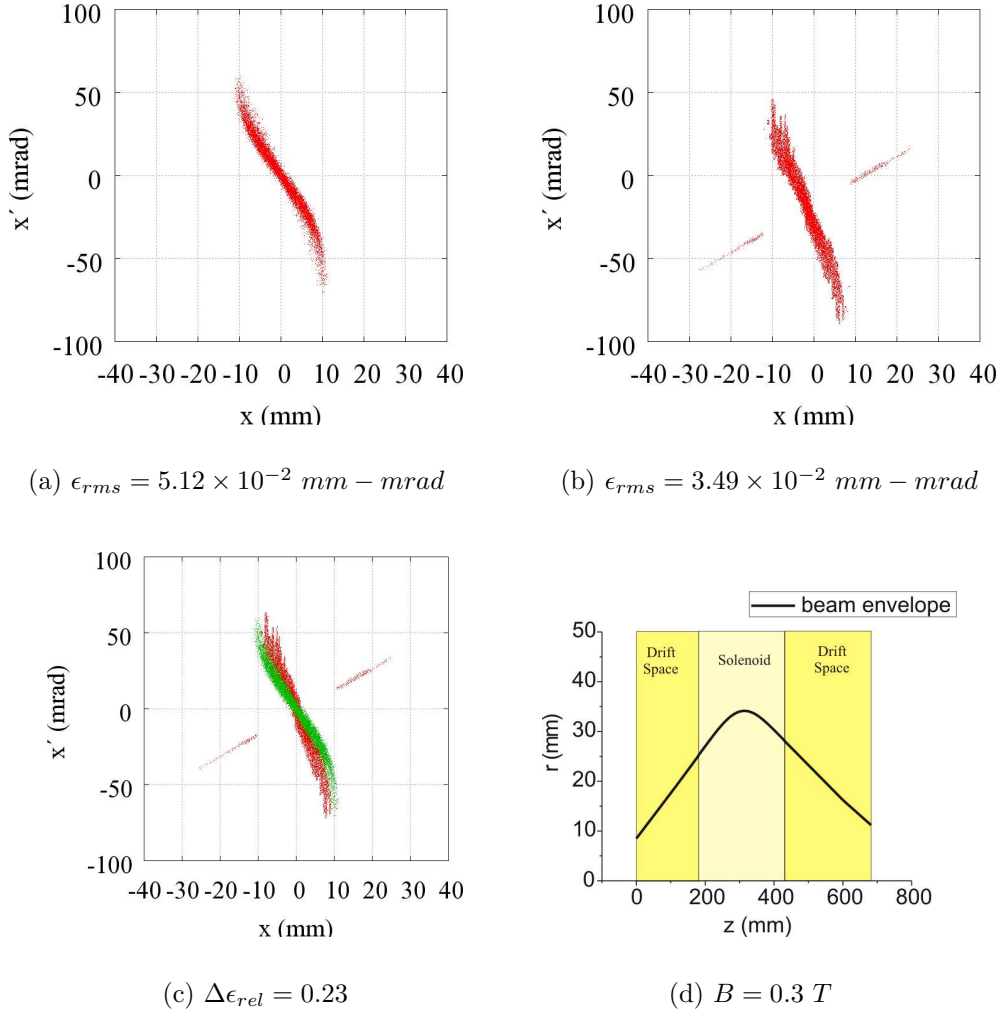


Figure 4.18: (a) Simulated and (b) measured phase-space for  $I = 150 \text{ A}$  corresponding to magnetic field of  $0.3 \text{ T}$  at energy of  $8 \text{ keV}$  beam energy. Off axis  $18 \text{ mrad}$  shift in output phase can be noticed. The neutral beam fraction was not simulated. (c) Overlapped distribution green is simulated and red the measured. (d) Corresponding beam envelope.

fraction is not taken into consideration for simulations purpose. Figure 4.18(d) shows an example of beam envelope for  $8 \text{ keV}$  energy.

At constant magnetic field beam size and divergence angles measured are plotted as function of energy in figure 4.19. The beam size is known to have parabolic dependence on  $k$  if measured before focus point [44]. Due to the limitations of experiments the beam size seems constant after certain energy in figure 4.19 on left. Thus in the figure 4.19 the parabolic nature is not clearly seen due to experimental limitations. The measured beam size for energy range  $6 - 12 \text{ keV}$  is compared with simulations in figure 4.20.

It was observed that the beam current had influence on the phase-space distribution. The beam current was varied using the arc current of filament in ion source shown in figure 4.21(a). Figure 4.21(b) shows size of the beam plotted as function of beam current. The difference in spot size in extremum case is around 15%.

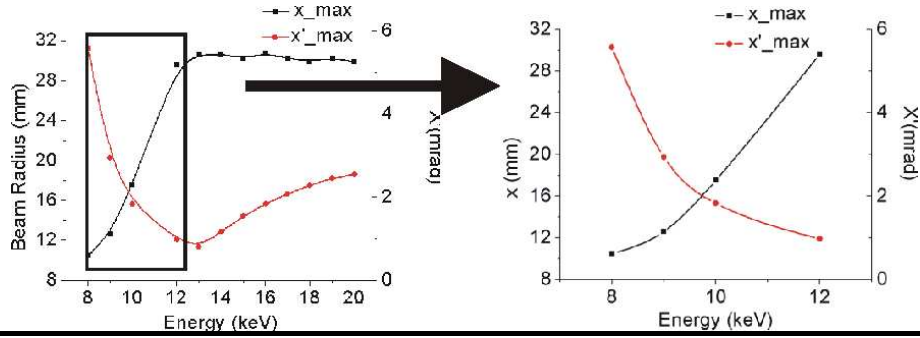


Figure 4.19: Beam radius and divergence dependence on energy and the plot at low energy.

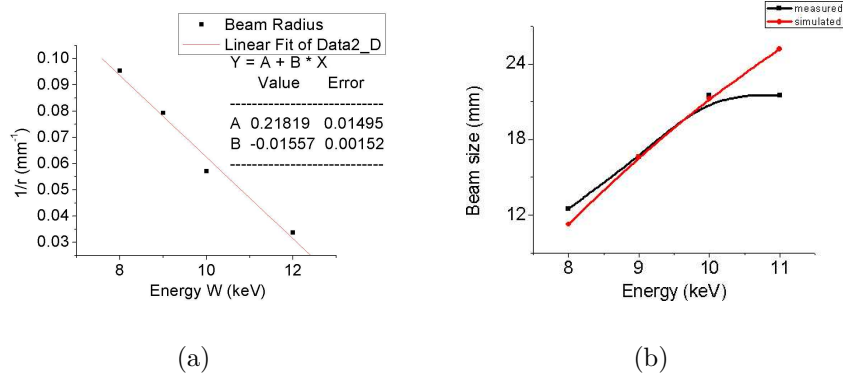


Figure 4.20: Figure (a) shows the linear behavior of inverse beam radius as function of energy and (b) compares the measured beam radius with the simulations. Magnetic field was held constant at 0.3 T.

### 4.2.3 Proton beam transport

The solenoidal magnetic field acts like filter when multi specie beam is transported, example  $H_2$ ,  $N_2$ . As shown in previous section the maximum of 45% proton fraction was measured to be delivered by ion source. Figure 4.22 shows example of simulated and measured beam transported through solenoid at energy 6keV with 0.14 T magnetic field

The beam transport was further simulated to get phase-space distribution which was used as input parameter for transport through single toroidal segment. The figure 4.23 shows the scheme used to simulate the beam phase-space. The outplane was chosen at distance 80 mm away from solenoid keeping the distance of solenoid to source same, a comparison with measurements is not possible.

Figure 4.24 which shows minima occurring at different positions of magnetic field. Higher the mass stronger the magnetic field required to focus particular fraction. Beam energy of 12 keV was used for the simulation.

When total beam size plotted it shows minima at around 0.28 T with minimum spot size of 27 mm. Figure 4.25 shows the phase-space distribution of total beam when the beam size is minimum. This distribution appears at 0.28 T. This

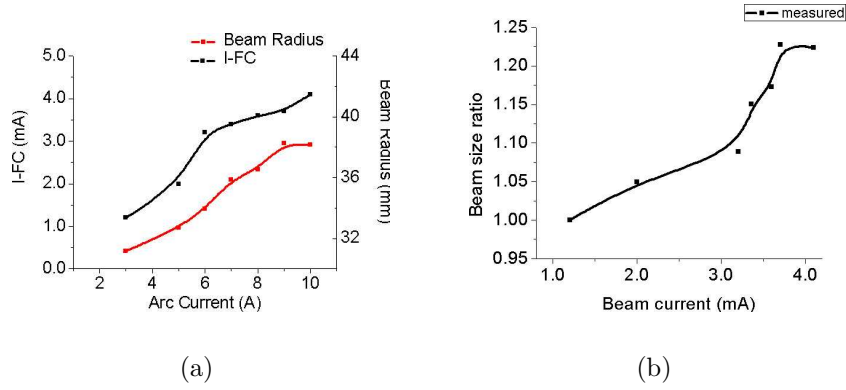


Figure 4.21: (a) Beam current in Faraday cup and beam size downstream of solenoid as function of arc current and (b) increased beam size as a function of beam current. Beam energy  $9.2 \text{ keV}$  and magnetic field of  $0.3 \text{ T}$  was used.

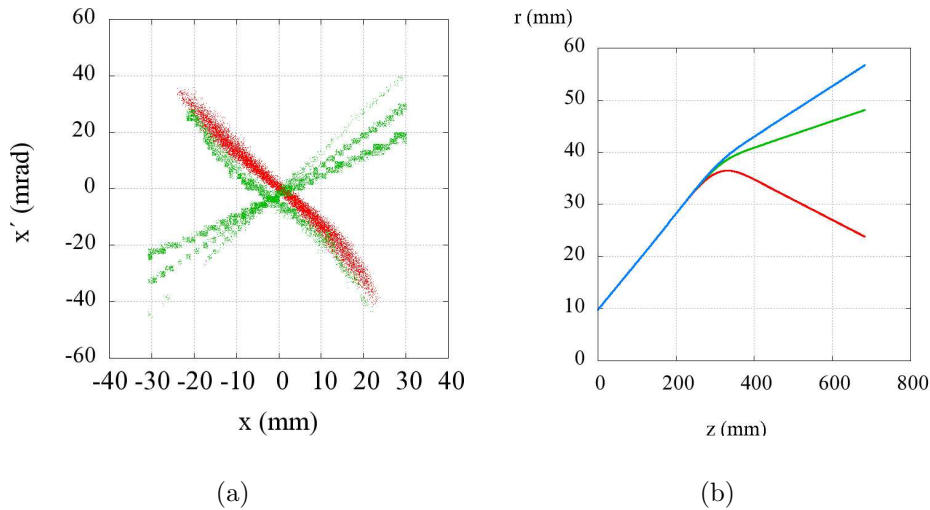


Figure 4.22: (a) Overlapped phase-space distribution simulated (red) and experimentally measured (green), (b) beam envelopes for different species. Red is  $H^+$ , green is  $H_2^+$  and blue is  $H_3^+$  fraction.

phase space distribution was taken as input for beam transport experiments and simulations in a single toroidal segment.

#### 4.2.4 Effect of magnetic field from toridal segment

The toroidal segment that was used in the experiments, has no magnetic shielding material. Thus lines of force are coupled with that of solenoid. The shielding material of solenoid found to have effect on the field in between two components, the solenoid and the toroidal segment. The simulation performed using Microwave

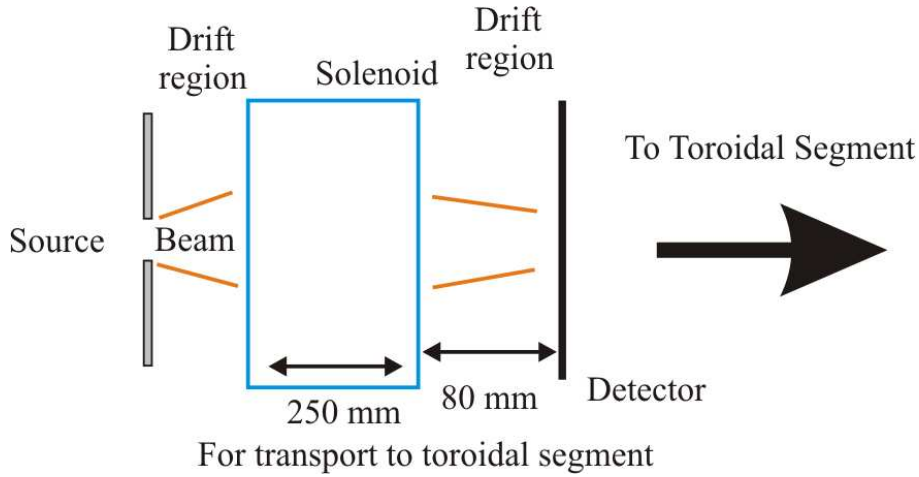


Figure 4.23: Simulation scheme for transport through solenoid for input parameters for further experiments.

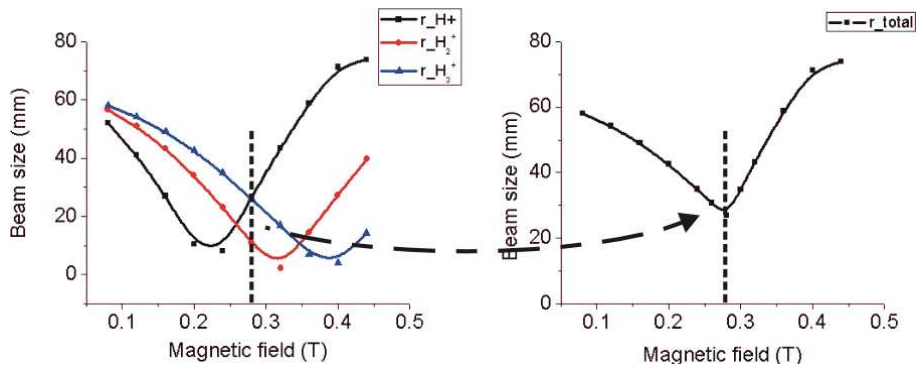


Figure 4.24: Beam size as a function of magnetic field for three different fractions (on left). The beam size as function of magnetic field for all fractions together. Beam energy  $12\text{ keV}$  was used.

**Studio** shows a definite amount of magnetic field level is superimposed on the solenoidal field. Figure 4.26(a) shows one of the example of magnetic field simulated with toroidal field and solenoidal field both having set at maximum values of  $0.6\text{ T}$  on axis. Around  $0.14\text{ T}$  magnetic field is present at the penetration region.

Figure 4.26(b) shows a small effect of toroidal magnetic field on the proton beam. The beam size was seen to be decreasing with respect to higher magnetic field.  $12\text{ keV}$  beam was simulated in this case. The solenoidal field was held constant at  $0.3\text{ T}$ . The addition effect of this field was seen in beam transport experiments. The experiments regarding this were carried out in detail.

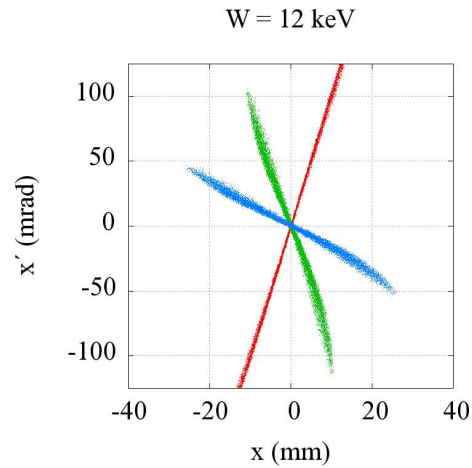


Figure 4.25: Phase-space distributions 80 *cm* downstream of solenoid showing the minima for the mixed beam. This distribution was calibrated for all energies and used further for simulation and measurements as a input distribution. Red is  $H^+$ , green is  $H_2^+$  and blue is  $H_3^+$  fraction. The proton fraction is chopped off with respect to the scanner acceptance.

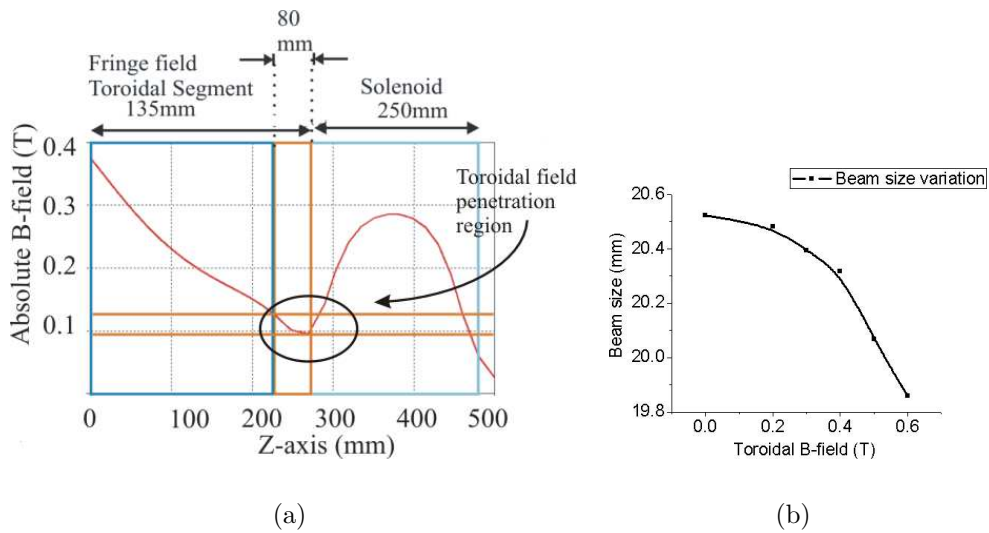


Figure 4.26: (a) Magnetic field distribution in between the region of solenoid and toroidal segment. It shows small effect of magnetic material of solenoid, creating valley. (b) Beam size downstream of solenoid as a function of toroidal magnetic field. The solenoidal field (0.3 T) and beam energy 12 *keV* was constant. Only proton fraction was simulated.

## 4.3 Transport through a toroidal segment

Figure 4.27 shows the experimental setup used for beam transport studies in single segment with a toroidal magnetic field. The setup is an extension of solenoidal transport experiments. A toroidal segment was installed at the end of the solenoid. The emittance scanner was installed downstream of the toroidal segment for beam diagnostics (see photograph A.13 in appendix). Table (4.2) lists the important physical properties of a single segment (BRUKER Toroid Nr. 705001).

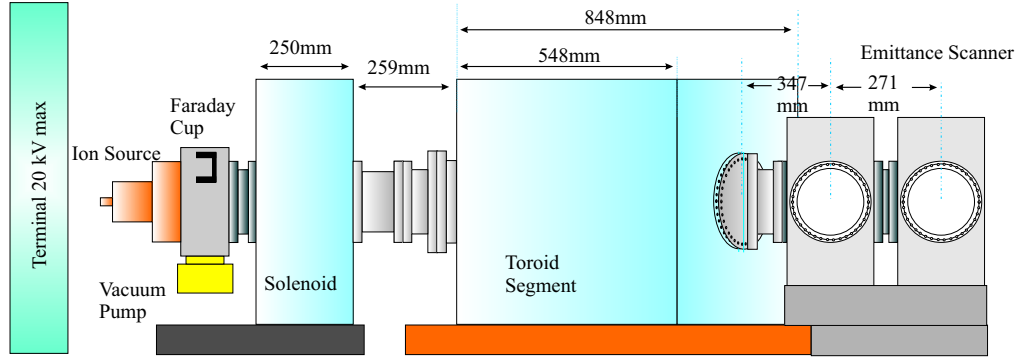


Figure 4.27: Experimental setup for investigation of beam transport in a single toroidal segment.

Table 4.2: Physical properties of Toroidal Segment

No. of winding	$33 \times 24$
Maximum Magnetic field on axis	$0.6 T$
Maximum Voltage and Current	$140 V, 480 A$
Major Radius $R_0$	$1300 mm$
Arc angle	$30^\circ$
Arc length	$680 mm$
Diameter of aperture	$200 mm$
Magnetic Shielding	absent
Cooling water	$70 l/min$
Weight	$1050 kg$

### 4.3.1 Input Parameter Space

The input phase space distribution was chosen in such a way that the composite beam size (including all fractions) for proton beam is minimum. The phase-space distribution for  $12 keV$  energy was shown in the previous section. The solenoidal field was calibrated to give the same distribution for all input energies. The energy



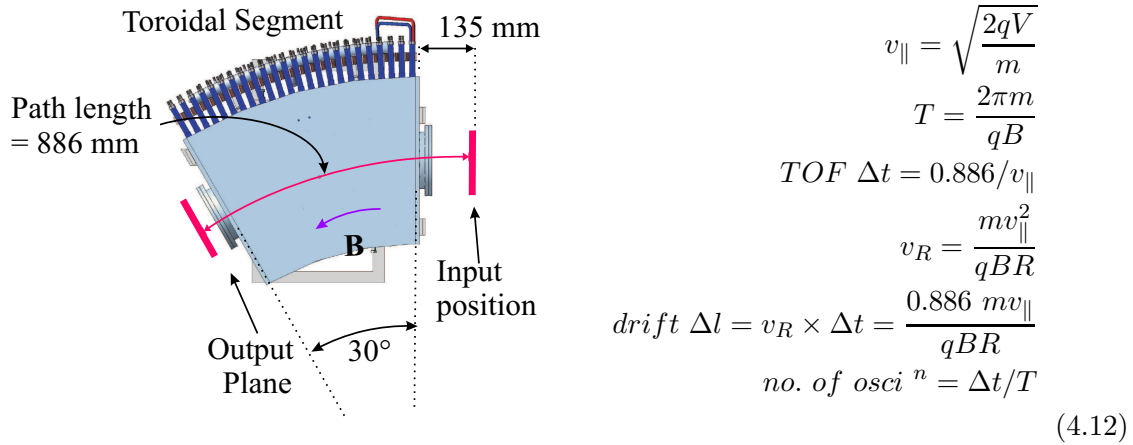


Figure 4.28: The schematic diagram and formulae for analytical calculation.

range was varied from 4 keV to 12 keV in 1 keV steps with magnetic field 0.4 T to 0.6 T in a 0.025 T step size.

Table(4.3) list the velocities for different fractions in a beam and table (4.4) lists the time period in longitudinal direction. The longitudinal arc length is 0.886 m. The drifts on millimetre scale calculated for this path length are tabulated in table(4.5). The number of oscillations are calculated by dividing the time of flight by gyro period, are listed in table (4.6). The fractional number in turn gives the phase of the beam at the output plane.  $A$  is the mass number of ions.

Table 4.3: Longitudinal velocities at different energies.

Energy	Velocity (m/s)		
	$A = 1$	$A = 2$	$A = 3$
4 keV	$8.78e + 05$	$6.21e + 05$	$5.07e + 05$
5 keV	$9.82e + 05$	$6.94e + 05$	$5.67e + 05$
6 keV	$1.08e + 06$	$7.60e + 05$	$6.21e + 05$
7 keV	$1.16e + 06$	$8.21e + 05$	$6.71e + 05$
8 keV	$1.24e + 06$	$8.78e + 05$	$7.17e + 05$
9 keV	$1.32e + 06$	$9.31e + 05$	$7.60e + 05$
10 keV	$1.39e + 06$	$9.82e + 05$	$8.02e + 05$
11 keV	$1.46e + 06$	$1.03e + 06$	$8.41e + 05$
12 keV	$1.52e + 06$	$1.08e + 06$	$8.78e + 05$

Figure 4.29 shows analytically calculated beam size as a function of energy and toroidal magnetic field. The beam size for each specie is calculated by considering oscillatory behaviour in beam diameter. The vertical drift is added separately for respective specie. The spot size is then calculated for the composite beam. The focal points are shown by the blue coloured region. At energy 8 keV two focal points exist in the given parameter space of a magnetic field.

Table 4.4: Gyro-period for different species at different magnetic fields.

B(T)	Gyro Period (s)		
	A = 1	A = 2	A = 3
0.400	$1.63e - 07$	$3.26e - 07$	$4.89e - 07$
0.425	$1.53e - 07$	$3.07e - 07$	$4.60e - 07$
0.450	$1.45e - 07$	$2.90e - 07$	$4.35e - 07$
0.475	$1.37e - 07$	$2.74e - 07$	$4.12e - 07$
0.500	$1.30e - 07$	$2.61e - 07$	$3.91e - 07$
0.525	$1.24e - 07$	$2.48e - 07$	$3.73e - 07$
0.550	$1.19e - 07$	$2.37e - 07$	$3.56e - 07$
0.575	$1.13e - 07$	$2.27e - 07$	$3.40e - 07$
0.600	$1.09e - 07$	$2.17e - 07$	$3.26e - 07$

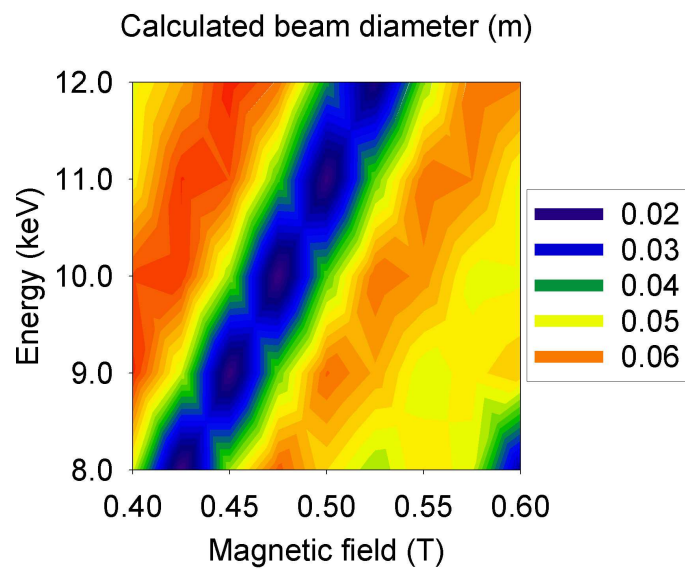


Figure 4.29: Analytical calculation for the beam diameter (colour-coded in metre) plotted as a function of energy and magnetic field. Blue points represent a beam waist.

Table 4.5: Vertical drift at different energies for different magnetic fields, all numbers in *mm*.

Energy=5keV				Energy=5 keV				Energy=6 keV			
B (T)	A = 1	A = 2	A = 3	B (T)	A = 1	A = 2	A = 3	B (T)	A = 1	A = 2	A = 3
0.400	15	21	26	0.400	17	24	30	0.400	19	26	32
0.425	14	20	25	0.425	16	23	28	0.425	17	25	30
0.450	13	19	23	0.450	15	21	26	0.450	16	23	29
0.475	13	18	22	0.475	14	20	25	0.475	16	22	27
0.500	12	17	21	0.500	13	19	24	0.500	15	21	26
0.525	11	16	20	0.525	13	18	22	0.525	14	20	25
0.550	11	15	19	0.550	12	17	21	0.550	13	19	23
0.575	10	15	18	0.575	12	17	20	0.575	13	18	22
0.600	10	14	17	0.600	11	16	20	0.600	12	17	21

Energy=7 keV				Energy=8 keV				Energy=9 keV			
B (T)	A = 1	A = 2	A = 3	B (T)	A = 1	A = 2	A = 3	B (T)	A = 1	A = 2	A = 3
0.400	20	29	35	0.400	21	31	38	0.400	23	32	40
0.425	19	27	33	0.425	20	29	35	0.425	21	30	37
0.450	18	25	31	0.450	19	27	33	0.450	20	29	35
0.475	17	24	29	0.475	18	26	32	0.475	19	27	33
0.500	16	23	28	0.500	17	24	30	0.500	18	26	32
0.525	15	22	27	0.525	16	23	28	0.525	17	25	30
0.550	14	21	25	0.550	15	22	27	0.550	16	23	29
0.575	14	21	24	0.575	15	21	26	0.575	16	22	28
0.600	13	19	23	0.600	14	20	25	0.600	15	21	26

Energy=10 keV				Energy=11 keV				Energy=12 keV			
B (T)	A = 1	A = 2	A = 3	B (T)	A = 1	A = 2	A = 3	B (T)	A = 1	A = 2	A = 3
0.400	24	34	42	0.400	25	36	44	0.400	26	38	46
0.425	23	32	40	0.425	24	34	41	0.425	25	35	43
0.450	21	30	37	0.450	22	32	39	0.450	23	33	41
0.475	20	29	35	0.475	21	30	37	0.475	22	32	39
0.500	19	27	34	0.500	20	29	35	0.500	21	30	37
0.525	18	26	32	0.525	19	27	33	0.525	20	28	35
0.550	17	25	30	0.550	18	26	32	0.550	19	27	33
0.575	17	24	29	0.575	17	25	31	0.575	18	26	32
0.600	16	23	28	0.600	17	24	29	0.600	17	25	31

Table 4.6: Number of oscillations (phase) at different energies for different magnetic fields.

Energy=5 keV				Energy=5 keV				Energy=6 keV			
B (T)	A = 1	A = 2	A = 3	B (T)	A = 1	A = 2	A = 3	B (T)	A = 1	A = 2	A = 3
0.400	6.19	4.38	3.57	0.400	5.54	3.92	3.20	0.400	5.06	3.57	2.92
0.425	6.58	4.65	3.80	0.425	5.88	4.16	3.40	0.425	5.37	3.80	3.10
0.450	6.97	4.93	4.02	0.450	6.23	4.41	3.60	0.450	5.69	4.02	3.28
0.475	7.35	5.20	4.24	0.475	6.58	4.65	3.80	0.475	6.00	4.24	3.47
0.500	7.74	5.47	4.47	0.500	6.92	4.89	4.00	0.500	6.32	4.47	3.65
0.525	8.13	5.75	4.69	0.525	7.27	5.14	4.20	0.525	6.63	4.69	3.83
0.550	8.51	6.02	4.91	0.550	7.61	5.38	4.40	0.550	6.95	4.91	4.01
0.575	8.90	6.29	5.14	0.575	7.96	5.63	4.60	0.575	7.27	5.14	4.20
0.600	9.29	6.57	5.36	0.600	8.31	5.87	4.80	0.600	7.58	5.36	4.38

Energy=7 keV				Energy=8 keV				Energy=9 keV			
B (T)	A = 1	A = 2	A = 3	B (T)	A = 1	A = 2	A = 3	B (T)	A = 1	A = 2	A = 3
0.400	4.68	3.31	2.70	0.400	4.38	3.10	2.53	0.400	4.13	2.92	2.38
0.425	4.97	3.52	2.87	0.425	4.65	3.29	2.69	0.425	4.39	3.10	2.53
0.450	5.27	3.72	3.04	0.450	4.93	3.48	2.84	0.450	4.64	3.28	2.68
0.475	5.56	3.93	3.21	0.475	5.20	3.68	3.00	0.475	4.90	3.47	2.83
0.500	5.85	4.14	3.38	0.500	5.47	3.87	3.16	0.500	5.16	3.65	2.98
0.525	6.14	4.34	3.55	0.525	5.75	4.06	3.32	0.525	5.42	3.83	3.13
0.550	6.44	4.55	3.72	0.550	6.02	4.26	3.48	0.550	5.68	4.01	3.28
0.575	6.73	4.76	3.88	0.575	6.29	4.45	3.63	0.575	5.93	4.20	3.43
0.600	7.02	4.96	4.05	0.600	6.57	4.64	3.79	0.600	6.19	4.38	3.57

Energy=10 keV				Energy=11 keV				Energy=12 keV			
B (T)	A = 1	A = 2	A = 3	B (T)	A = 1	A = 2	A = 3	B (T)	A = 1	A = 2	A = 3
0.400	3.92	2.77	2.26	0.400	3.73	2.64	2.16	0.400	3.57	2.53	2.06
0.425	4.16	2.94	2.40	0.425	3.97	2.80	2.29	0.425	3.80	2.69	2.19
0.450	4.41	3.11	2.54	0.450	4.20	2.97	2.42	0.450	4.02	2.84	2.32
0.475	4.65	3.29	2.68	0.475	4.43	3.13	2.56	0.475	4.24	3.00	2.45
0.500	4.89	3.46	2.83	0.500	4.67	3.30	2.69	0.500	4.47	3.16	2.58
0.525	5.14	3.63	2.97	0.525	4.90	3.46	2.83	0.525	4.69	3.32	2.71
0.550	5.38	3.81	3.11	0.550	5.13	3.63	2.96	0.550	4.91	3.48	2.84
0.575	5.63	3.98	3.25	0.575	5.37	3.79	3.10	0.575	5.14	3.63	2.97
0.600	5.87	4.15	3.39	0.600	5.60	3.96	3.23	0.600	5.36	3.79	3.10

### 4.3.2 Acceptance of an emittance scanner

Due to geometry of the used emittance scanner, limitations were imposed on the measurement of phase-space distribution along toroidal path. The curved magnetic field lines outside the magnetic segment hamper the ability of the emittance scanner. Figure 4.30 shows the simulated field lines. Particles which follow the field lines trace a curved path. The distance between the slit and grid was  $246\text{ mm}$ . A straight line formula  $\theta = \tan^{-1}(\delta x/D)$  then can not be used for angle estimation of the traced particles.

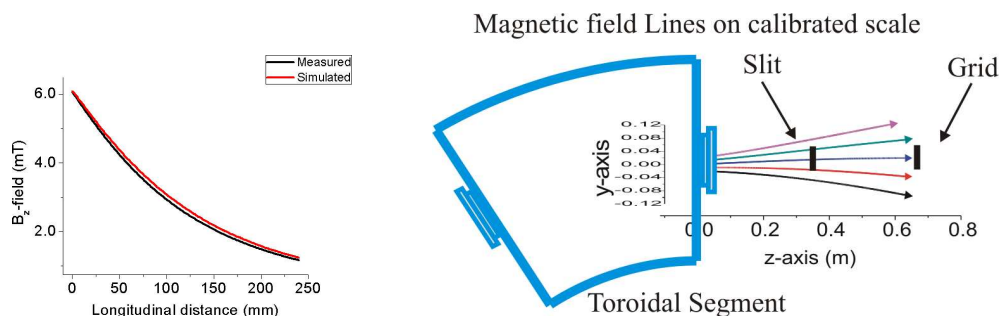


Figure 4.30: (a) Fringe field measured and compared at 10A field (b) scaled magnetic field line which demonstrates the field lines between slit and grid of emittance scanner.

The emittance scanner consists of a slit-grid arrangement that can move vertically, measuring the phase-space distribution in  $x - x'$  plane. Figure 4.31 shows a photograph of the emittance scanner. The slit can move vertically  $\pm 520\text{ mm}$  cutting the beam path. The slit is  $0.1\text{ mm}$  with  $60\text{ mm}$  width. A particle which possesses more than  $5.7^\circ$  angle in the  $y$ -direction can not be detected.

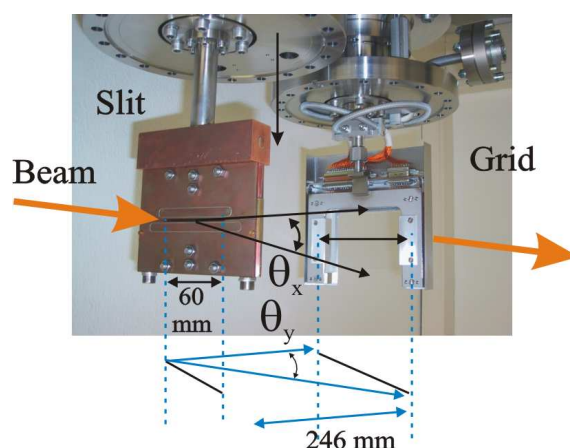


Figure 4.31: Grid-slit arrangement of an emittance scanner. The slit and grid moves vertically downward and cut the path of beam. The dimensions of the assembly are shown in figure.

Three species of ions were expected to be present in the input beam namely  $H^+$ ,  $H_2^+$  and  $H_3^+$ . The  $H_2^+$  fraction was expected to be negligible for the chosen setting of ion source. The drift and phase output of the beam due to toroidal magnetic field is different for different masses. The drift increases with mass and the output angle changes with respect to gyro-frequency. Moreover, the solenoidal field produces the different phase-space distribution for different species. This causes one of the beam specie to hit the wall at some settings. When beam is hit on the wall, produces secondary electrons giving rise to high noise. High noise to signal ratio influences the measurement of beam phase-space.

### 4.3.3 Measurement with emittance scanner

Due to the stated limitations, the readings from the emittance scanner cannot be directly compared with the simulated results.

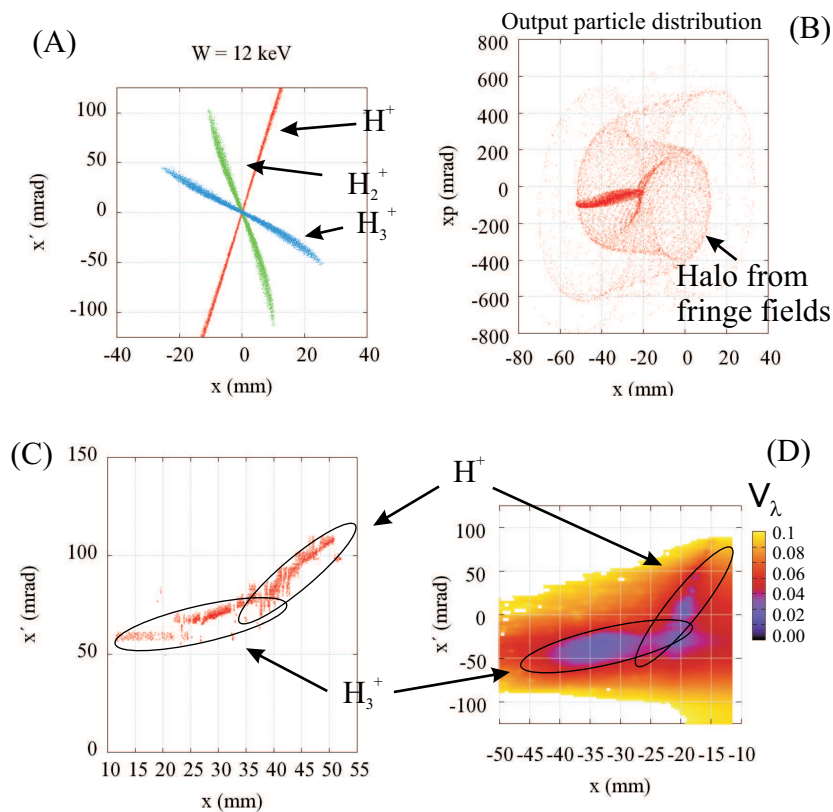


Figure 4.32: Comparison between simulations and emittance scanner data. (a) input phase space distribution red  $H^+$ , green  $H_2^+$ , and blue  $H_3^+$  fraction, (b) simulated output phase-space distribution showing halo particles, (c) measured phase-space distribution, (d) phase-distribution simulated by applying the emittance scanner limitations and encoded with velocity ratio  $v_\lambda$ . In this example input parameters for the ion source were set to give negligible  $H_2^+$  fraction, hence was not detected at output.

Figure 4.32(a) shows the input and output distribution simulated and compared with measurements, at an energy of  $12$  keV with magnetic field of  $0.6$  T. The input distribution represents a focal point of composite proton beam at a distance

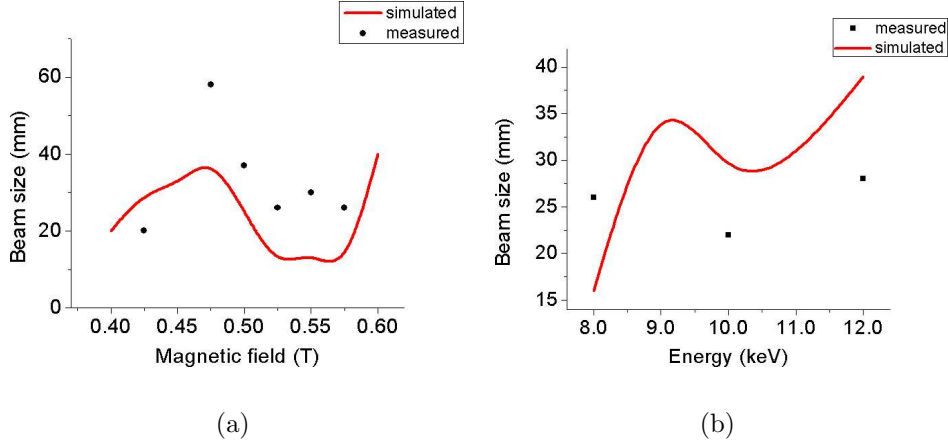


Figure 4.33: Beam size as a function of the magnetic field at energy  $10 \text{ keV}$  (on left) and as a function of energy at a magnetic field  $0.425 \text{ T}$  (on right). The arc length was about  $1.2 \text{ m}$ .

of  $80 \text{ mm}$  from the solenoid. The arc distance from this input plane ( $135 \text{ mm}$  in front of the face of toroidal segment) to the position of the slit, phase shift is  $0.65\pi$ . This gives maximum probability of detection of particles, with a given slit-grid scanner. Figure 4.32(b) shows the phase-space of a beam, that consists of halo particles and a core at the centre. When particles possessing an angle more than  $5.7^\circ$  in  $y$ -direction are filtered out, we get an output graph as shown in Figure 4.32(d). The  $v_\lambda$  value is colour coded. This is then directly compared with Figure 4.32(c). One can see that the measured beam size is similar to the size predicted by simulation.

Figure 4.33(a) shows the plot of beam size measured as a function of magnetic fields. The energy of the beam in this case was  $10 \text{ keV}$ . Although the absolute values are far from simulated curve, they show similar functional behavior. As shown in figure 4.33(b) only in three cases a clear signal was observed. Hence direct comparison is not possible. Since the noise level is not the same in all cases, all data files cannot be analyzed on the same level or compared directly with simulations. Due to this reason only three points are shown in the graph in one series.

#### 4.3.4 Optical diagnostics assembly

Phosphor screen can be used for detection of charged particle beams. It works on the principle of phosphorescence, a type of photoluminescence effect. A phosphor screen composed of  $(Zn, Cd)S : Ag$  known as  $P20$  was used on the merit of wavelength range of emitted light. It emits light with a range of  $470 \text{ nm} - 670 \text{ nm}$  and with a peak emission at  $550 \text{ nm}$ , a yellow-green colour. This is within a visible range and efficient for detection with normal digital camera chips.  $P20$  screen is also easy to produce on large scale, with low production cost.

Due to the presence of fringing fields ( $0.27 \text{ T}$  at the screen position) CCD camera can not be used. The magnetic field puts serious limitations on efficiency of a CCD chip. And due to its large size shielding is difficult as it results in

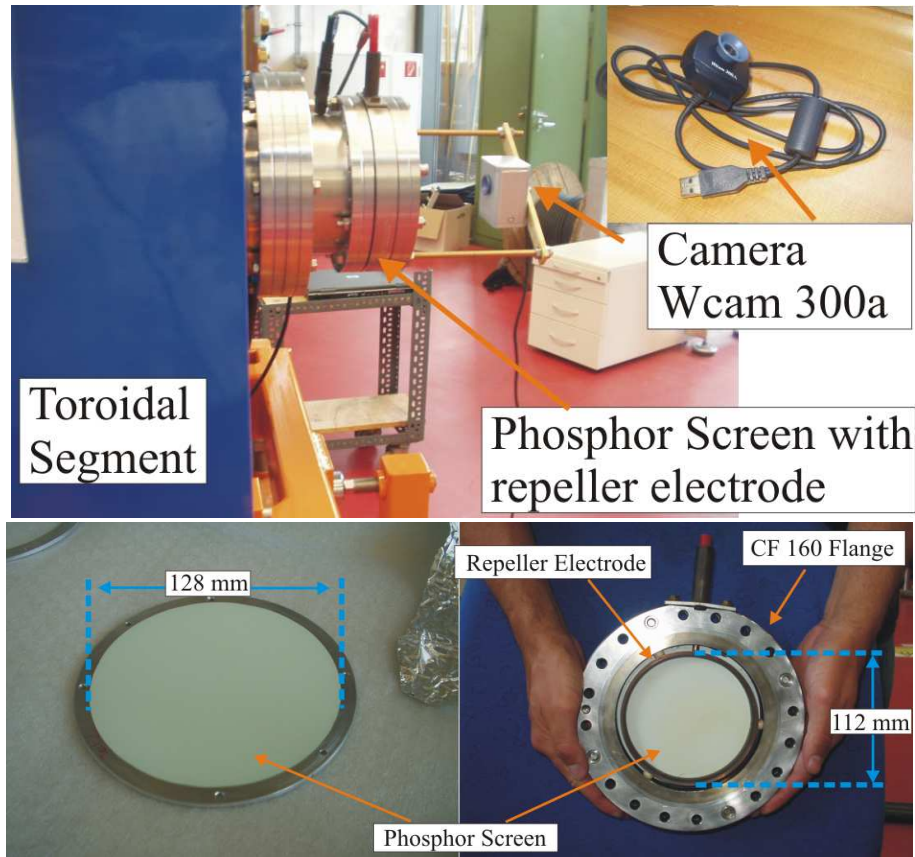


Figure 4.34: An optical assembly: photograph showing a camera and its mounted position within an iron shielded case. Lower picture shows phosphor screen mounting along with a repeller electrode. The screen is located at an arc length of  $0.886\text{ m}$  from input plane.

stronger forces. A simple digital camera was used for image detection due to its small size and cost effectivity. A small case made up of iron was designed for magnetic shielding for camera chip. Due to the small size of camera smaller shield is sufficient which do not disturb the field lines at the screen position. In front of the phosphor screen repeller electrode was installed to repel any secondary electrons produced (see figure 4.34).

The image produced by webcam was in `jpeg` format having dimensions of  $320 \times 240$  pixels with resolution of 96dpi. The image can be online recorded and videos can be made. A subroutine was written to analyze the image, which gives pixel intensity at every pixel position. Thus the beam position and size can be determined. Image calibration is discussed in the appendix A.5. The camera has chip with 8-bit storage memory. The maximum bit range is 0 – 256. Thus it was observed that for more than 8 W beam power, the chip goes into saturation mode.

The phosphor screen itself places another limitation. The screen can be exposed to a maximum of  $1.0\text{ W/cm}^2$  power. At the focused point the beam can have a diameter of 10 mm i.e. area of  $7.85 \times 10^{-3}\text{ m}^2$ . Thus maximum allowed power at focus can be 7.85 mW, which is too low to be detected by the web camera. Hence moderate energy of 6 – 10 keV at current 1.6 mA gives best measurement range



for comparison with simulations.

Figure 4.35 shows examples of the image captured for different settings. The phosphor screen is insensitive to the mass of the particles which it hit by. Thus it emits light by collision of positive particles in a beam or by electrons. The source of electron production may be

- ion beam collision with rest gas molecules ( $W_{electron} < 50 \text{ eV}$ )
- ion beam collision with wall vessel or flanges or a repeller electrode itself ( $W_{electron} < 50 \text{ eV}$ )
- ion beam collision with phosphor screen itself ( $W_{electron} < 50 \text{ eV}$ )
- electrons produced in source ( $W_{electron} < eV_{sc}$ )

In the first three cases the electrons may have energy in the range  $10 - 50 \text{ eV}$ . In the last case the electrons are produced in extraction assembly. These may have energy around the screening potential. In standard settings this potential is 10% that of extraction energy, i.e.  $400 - 1200 \text{ eV}$ .

One should also consider, the effect of image sticking. Static charge may develop on screen as phosphor is a bad conductor. This generates a ghost image that can influence the consequent image. However due to high magnetic field this effect is negligible.

Figure 4.35 shows typical behavior of images from a phosphor screen at an arc length  $0.886 \text{ m}$ . Figure 4.35(a) shows a well defined beam at low energy ( $4 \text{ keV}$ ). Due to low efficiency the halo produced by trapped proton is not detected by the digital camera. Figure 4.35(b) shows the typical picture when secondary electrons produced at a flange within the beam path are detected on the screen. A small spot at the centre is produced by electrons which are reflected back into the toroidal segment by screening electrode. This also helps to find a magnetic centre of the system. Figure 4.35(c) shows an example of the beam hitting the repeller electrode producing electrons which are accelerated to the phosphor screen, due to negative potential on the repeller electrode.

A camera (WCAM 300A) type was used due to its effectivity in a magnetic field. But the efficiency of converting light into digital signal is very low. At a lower power beam, the light emitted by the phosphor screen was too low to be detected by the camera. A ring pattern developed on the phosphor screen due to halo beam at low energy, visible to naked eyes or (other the better resolution camera), were undetectable for the camera. On the other hand when intensity of the beam is too high the data acquisition chip of the camera goes into saturation mode. Thus when picture in figure 4.35(d) is analyzed it shows intensity plateau at the beam centre. Figure 4.35(e) shows an example of an ideal image that can be analyzed well. It shows three beam fractions with different vertical drifts.

### 4.3.5 Measurements with phosphor screen

Figure 4.37(a) shows the behavior of the vertical drift as a function of energy. The drift is expected to grow with higher energy. Also, the drift is lower as the magnetic field is increased.

The effect of a magnetic field is plotted in Figure 4.38(a). The vertical drift decreases as the magnetic field is increased. It was observed that when the beam is transported through a single segment it experiences a shift in the horizontal

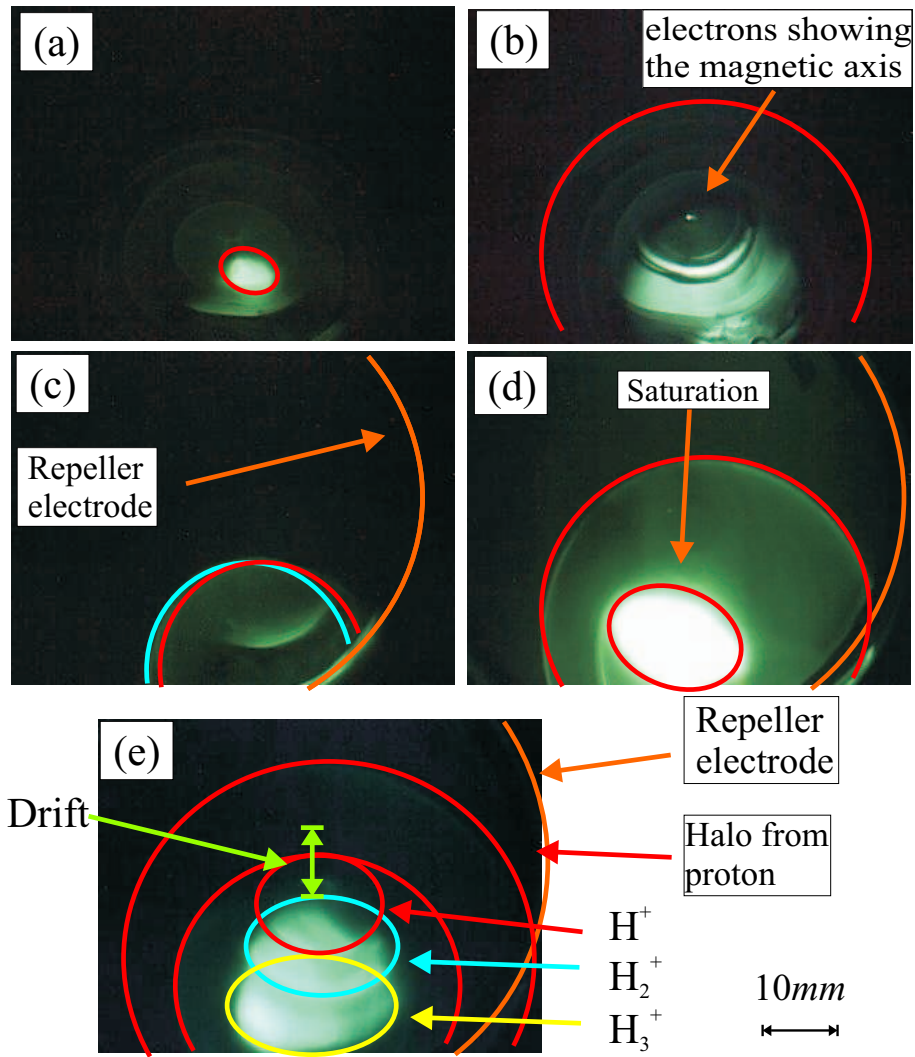


Figure 4.35: Properties of image produced by optical assembly.

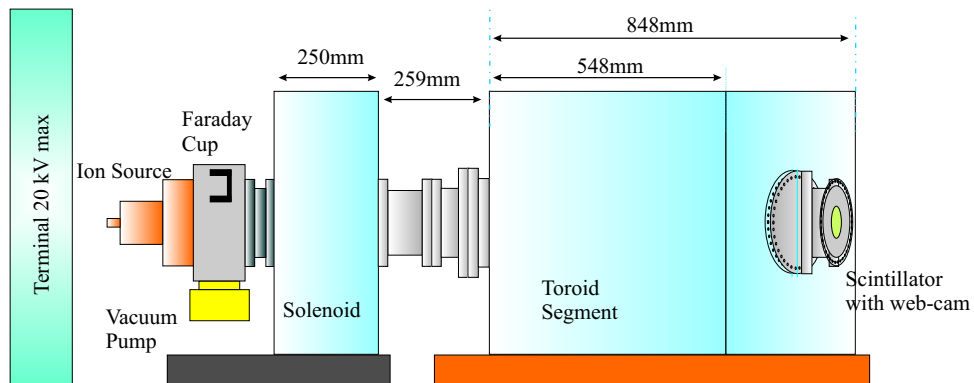
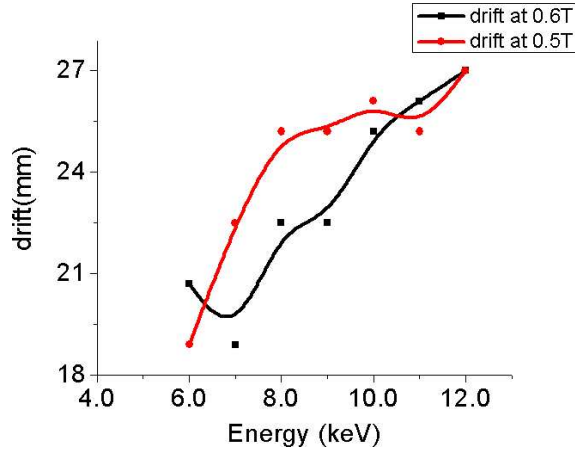
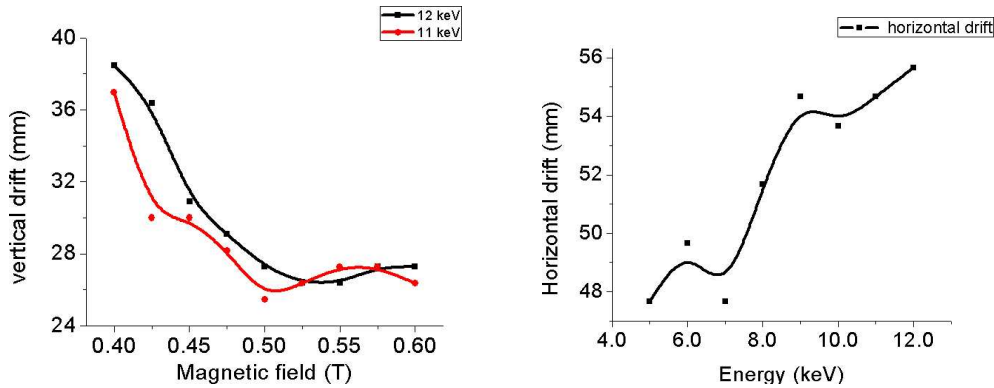


Figure 4.36: Experimental setup for measurements with optical assembly. The arc length was about 0.886 m.



(a)

Figure 4.37: Results from beam measurements from Phosphor screen. Absolute vertical drift as a function of energy for two different magnetic fields.



(a)

(b)

Figure 4.38: Dependence of vertical drift and horizontal drift on magnetic field.

direction. This drift is observed due to the conservation of the magnetic moment. The horizontal drift is seen to increase with increasing energy as shown in Figure 4.38(b). Oscillatory behaviour can be directly compared with simulation (see figure 3.9(a)). Due to the coupling of horizontal and vertical planes, in fringing field region particles receive horizontal kick proportional to the vertical position. This results in the same functional behaviour of the measured horizontal drift as that of simulated vertical drift inside the toroidal segment.

In Figure 4.39(a) the intensity is plotted as a function of energy and the magnetic field. At higher energy it shows an intense beam without much influence of the magnetic field. Figure 4.39(b) shows the intensity is normalized with respect

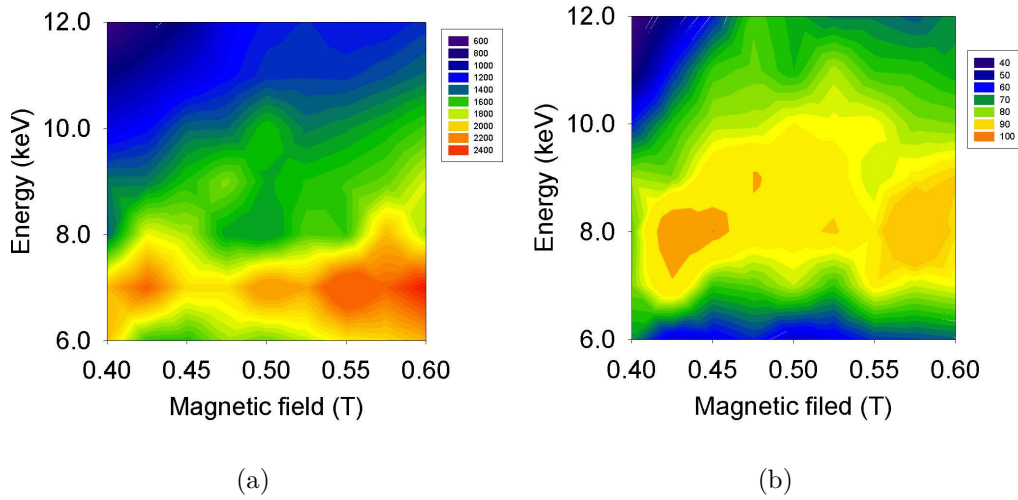


Figure 4.39: (a) Intensity on the Phosphor screen (colour-coded) as function of energy and magnetic field. (b) Averaged power density of the spot. These graphs can be compared with figure 4.29.

to beam size and power of the beam. Thus at an energy of  $8 \text{ keV}$  and magnetic field of  $0.425 \text{ T}$  we get the smallest spot size representing a focal point over the total arc length. This can be directly compared with the analytical value. The second focal point is located at  $0.575 \text{ T}$  for the same energy. This focal point is for the mixed beam.

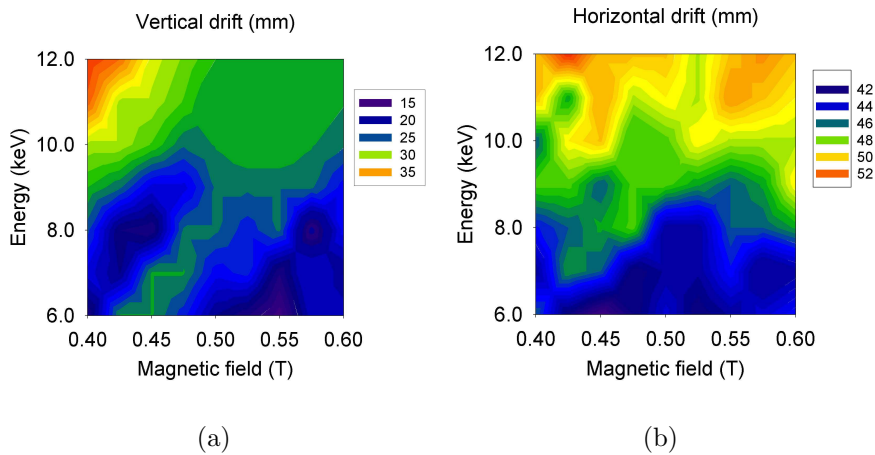


Figure 4.40: (a) Vertical drift (colour-coded) as a function of energy and toroidal magnetic field. (b) Horizontal drift (colour-coded) as a function of energy and toroidal magnetic field.

Figure 4.40 shows the plots of drift measured as a function of energy and

magnetic field. Figure 4.40(a) and Figure 4.40(b) show behavior of vertical and horizontal drift as a function of energy and magnetic field. The vertical drift is divided into four regions. Higher drift at higher energy and low magnetic field and lower drift at low energy and higher magnetic field. The horizontal drift due to vertical drift and fringing fields at the toroid exit is seen as a function of energy alone without much influence of the magnetic field.

### 4.3.6 Self field effect

Secondary electrons are produced due to the collision of beam with the vessel in the beam path. To repel these electrons a ring electrode was installed before the phosphor screen which can hold up to 1.2 kV potential. For the measurements above shown this electrode was held at a potential same as that of the screening electrode, thus forming a trap for electrons. This neutralizes the beam potential.

The space charge extent can be varied by changing the potential on the repeller electrode. Figure 4.41(a) shows vertical drift behavior with space-charge ( $V_{repel} = 0$  kV) and without space-charge ( $V_{repel} = V_{screening}$ ). Vertical drift is lower when the beam is transported with self fields.

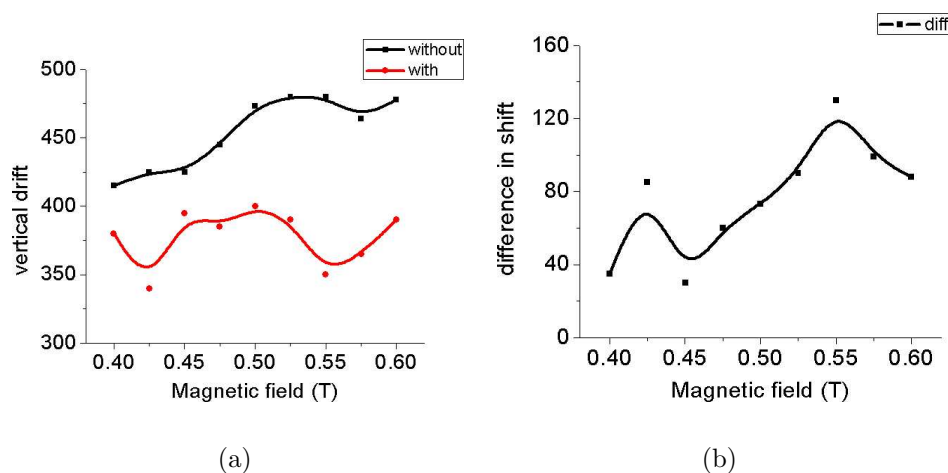


Figure 4.41: (a) Measured vertical drift (in arbitrary unit - Pixels) as function of magnetic field for with space charge (red) and without space charge (black). (b) Graph showing the difference (in arbitrary unit - Pixels) in both cases as a function of magnetic field.

The lower drift due to the higher space charge is credited to the  $\mathbf{E} \times \mathbf{B}$  drift. This has been also seen in in case of  $He^+$  beam. The oscillatory behaviour is due to the phase shift.

The effect of repeller potential was also observed on the beam size. When negative potential is applied to the electrode, the electrons are repelled. Figure 4.42(a) shows behavior of beam size for two case with space charge and without. Figure 4.42(b) shows their ratios as a function of magnetic field.

Figure 4.42 shows the beam size as a function of magnetic field in the case of repeller potential applied and set to zero. When potential is not present the gyro motion seems to be the dominating compared to another case.

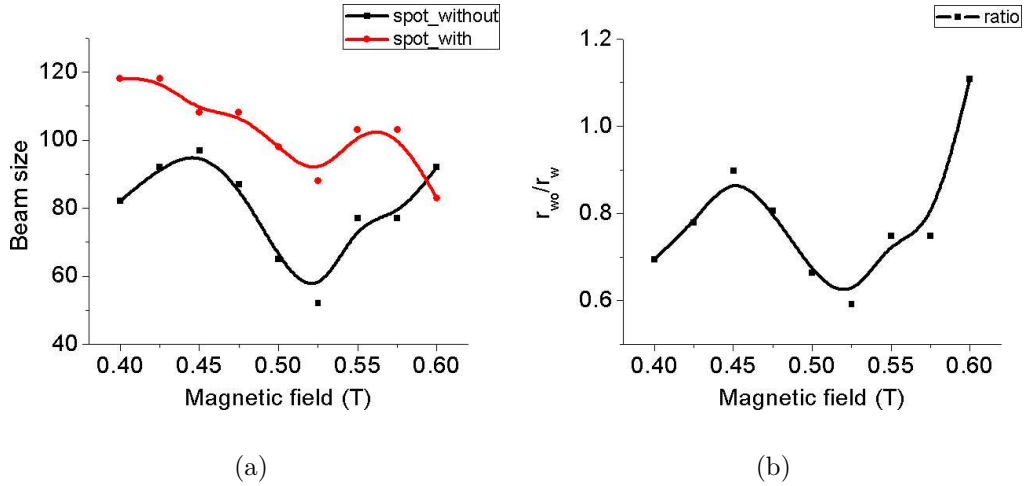


Figure 4.42: (a) Measured beam size (in arbitrary unit - Pixels) as function of magnetic field for with space charge (red) and without space charge (black). (b) Graph showing the ratio as a function of magnetic field.

### 4.3.7 Comparing the simulations with measurements

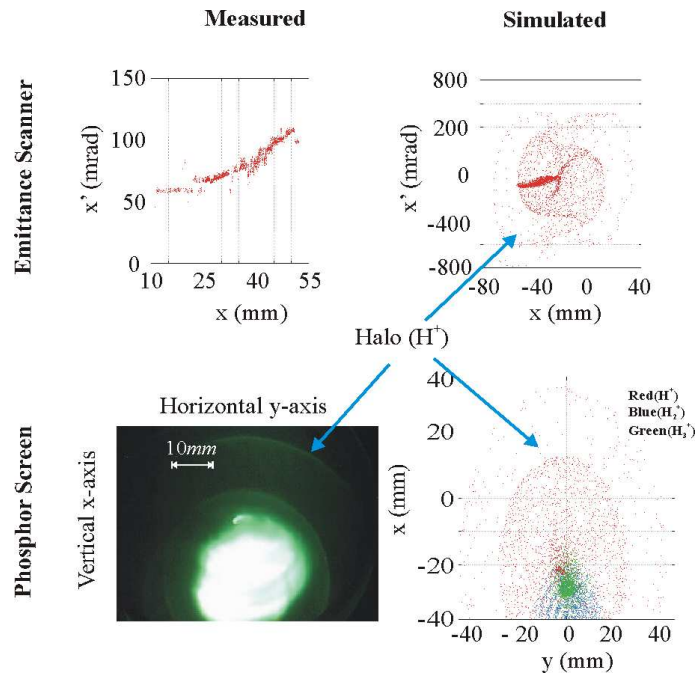


Figure 4.43: Figure showing simulated phase-space and measurements with emittance scanner and optical assembly.

Figure 4.43 shows an example of 12 keV beam in 0.4 T magnetic field detected with the emittance scanner and with the phosphor screen. The readings from the emittance scanner can only be compared with simulation when the phase-space

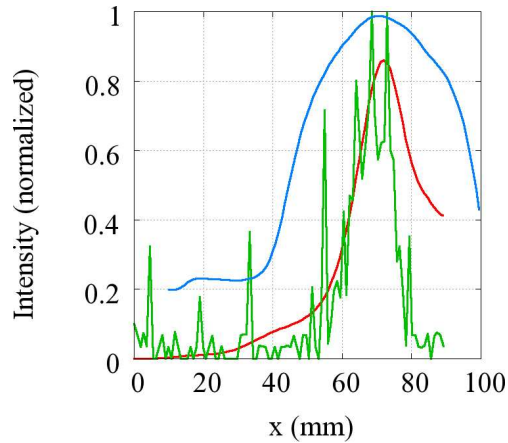


Figure 4.44: The vertical  $x$ -profile for intensity normalized to the peak of beam position. Red is the simulated curve, green is from the emittance scanner and blue is a measurement from an optical image. The geometric centre lies at  $x = 45 \text{ mm}$

is cut with respect to the acceptance of the scanner. The image of the optical assembly can be directly compared with the  $x - y$  plane. Figure 4.44 shows a comparison between the intensity profiles. The intensity is integrated in vertical  $x$ -direction. It can be seen Figure 4.44 that the drift beam position is the same for the both measurement devices and simulation. But the noise level of the emittance scanner varies vastly. The intensity profile is normalized.

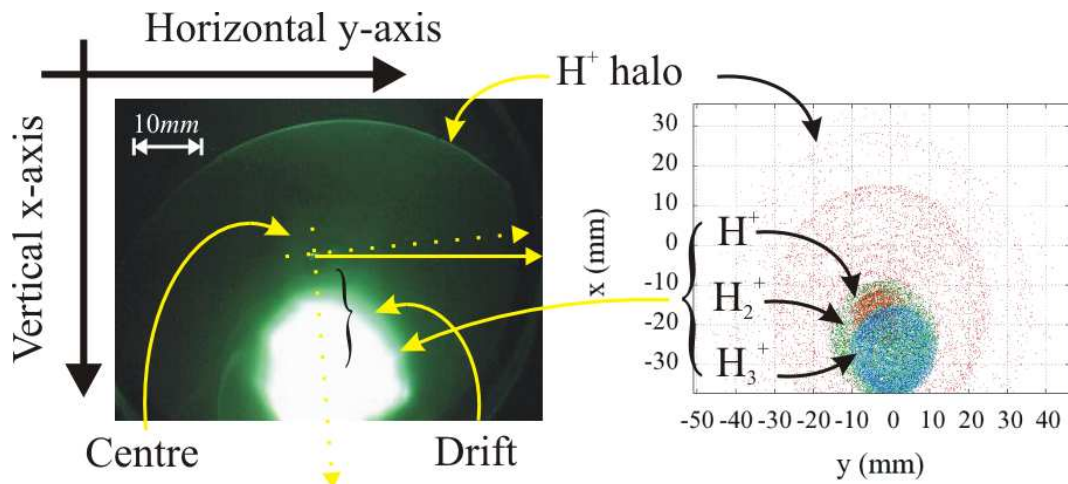


Figure 4.45: Figure showing measurements with phosphor screen and simulated distribution in  $x - y$  plane. A typical image consist of a core with three fractions and a halo from  $H^+$  particles.

Figure 4.45 shows the image from a phosphor screen that can be used for direct comparison. The intensity profile in both directions can be used for analysis. The vertical  $x$ -profile was used to find the drifted beam position and the horizontal  $y$ -profile was used for determination of the beam size. Calibration and scaling is shown in appendix. Figure 4.46 shows an example of intensity profile in horizontal

direction used to find a beam size. The profile was normalized and  $FWHM$  was taken as beam diameter.

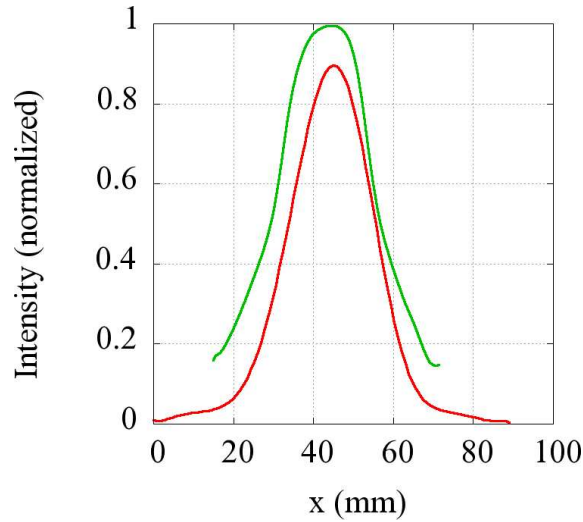


Figure 4.46: The horizontal beam profile comparison. Green is the measured one and red is the simulated curve. The geometric centre lies at  $x = 45 \text{ mm}$

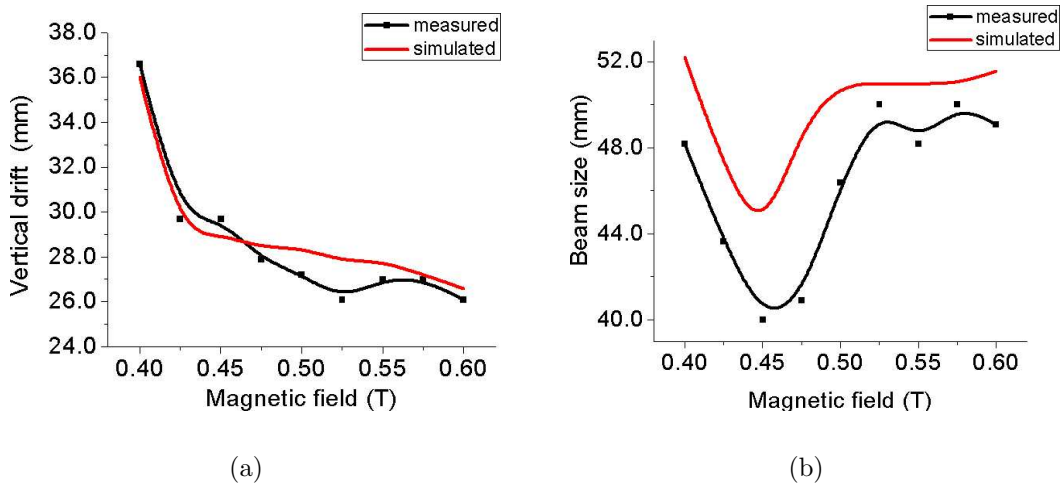


Figure 4.47: (a) Figure showing comparison between simulated and measured vertical drift and (b) beam size comparison as a function of the magnetic field.

Figure 4.47(a) shows the comparison of vertical beam drift as a function of a magnetic field. The difference between measured and simulated is negligible. In figure 4.47(b) the beam size is plotted as a function of the magnetic field. At  $0.45 \text{ T}$  the beam waist is located. In both cases beam energy was  $12 \text{ keV}$ . Small positive difference is observed in spot size. The simulated spot size is bigger than the measured. This can be attributed to effect of electrons produced near wall.



### 4.3.8 $He^+$ beam

Since  $He^+$  beams consist of a singly charged particle beam properties can be studied in details. The drift for  $He^+$  beam is four times higher compared than a proton beam. So only low energy  $He^+$  beams can be investigated with strongest possible ( $0.6 T$ ) toroidal field. In the third chapter effect of phase-space distribution is discussed which shows for particular beam divergence the transmission is the highest. To investigate this property a solenoidal field was varied for fixed toroidal field at beam energy of  $8 keV$ .

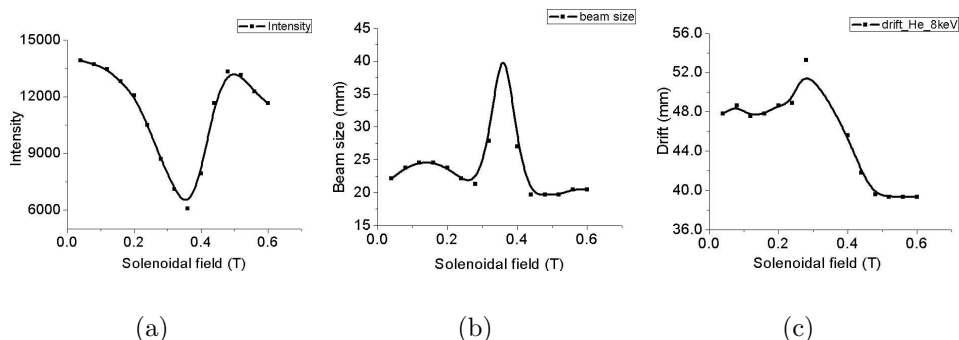


Figure 4.48: (a) Intensity as a function of solenoidal field, (b) variation of beam size as a function of solenoidal field, and (c) the vertical drift variation with solenoidal field strength.

Figure 4.48 shows the behavior of output intensity and beam size as a function of solenoidal field. At  $0.32 T$ , the beam size is the maximum with minimum intensity. At this magnetic field the phase-space distribution is the ellipse rotated with slope around  $120^\circ$  which was predicted theoretically. Figure 4.48(c) shows a behavior of vertical drift as a function of solenoidal field. The graph shows some unexpected jump. The variation is within  $\pm 4 mm$  range was observed in drift with variation in solenoidal field.

Figure 4.49 shows the effect of repeller potential on the intensity and drift of the ion beam. The graph of intensity shows a sudden drop for positive potential. When negative potential is applied it forms longitudinal trap for electrons. When positive potential is applied to repeller electrode electrons are absorbed and ion beam is decelerated. This seems to reduce intensity. Another effect due to electrons can be observed in terms of horizontal drift. Due to higher mass the vertical drift of  $He^+$  particles hit the flange producing electrons. These electrons along with repeller potential induce  $\mathbf{E} \times \mathbf{B}$  near the wall. Figure 4.49(b) shows horizontal drift as function of repeller potential Horizontal drift increases with increasing potential.

Figure 4.50 shows the effect of self-fields. For beam energy of  $8 keV$  beam current was varied using arc current. Magnetic field was set at maximum  $0.6 T$ . From figure 4.50(a) intensity curve shows a minima at  $0.6 mA$ . Also at this position, as seen in the figure 4.50(b), the beam size is maximum. Although both graphs show one to one relationship in the behavior, one can see, symmetry breaks at the end points for curve of beam size. This behavior is typically contributed to the  $\mathbf{E} \times \mathbf{B}$  effect. When the drift is higher part of the beam is lost on the wall,

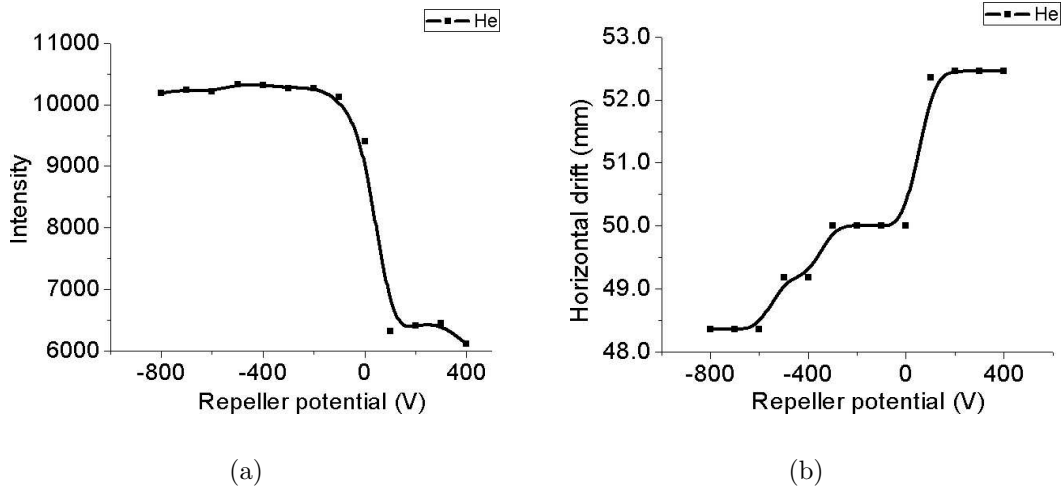


Figure 4.49: (a) Intensity and (b) beam size as a function of repeller potential for beam energy  $8\text{ keV}$ .

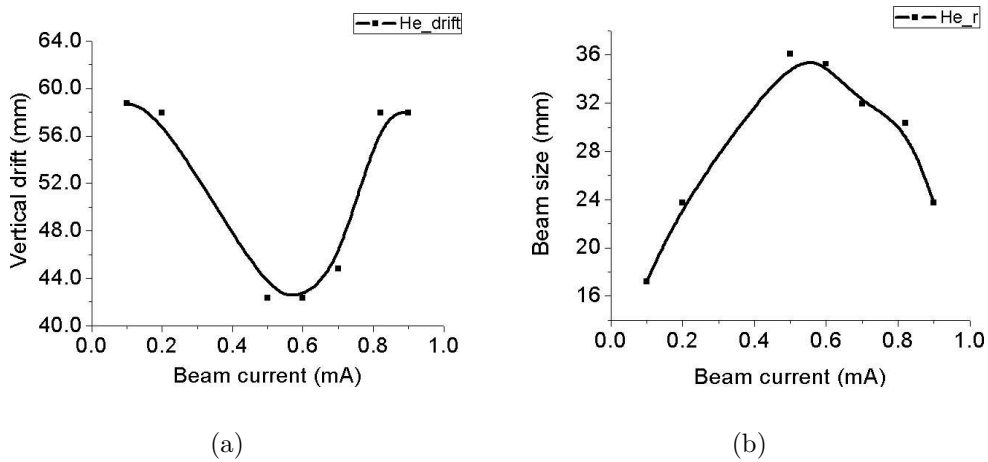


Figure 4.50: Vertical drift and beam size as a function of beam current.

producing secondary electrons. Actual size of the beam is larger in those cases. When beam current higher, more secondary electrons are produced, which leads to the higher  $\mathbf{E} \times \mathbf{B}$  drift near beam boundary. The overall effect is then increase of beam size. Thus at higher beam currents the drop of beam size is lowered.

### 4.3.9 Electron beam

Electron beam with an energy of  $3\text{ keV}$  was extracted. Figure 4.51 on the left shows a small spot representing a small beam spot. For electron beam at this energy vertical drift is  $0.31\text{ mm}$ . Thus it provides practically a position of magnetic centre.

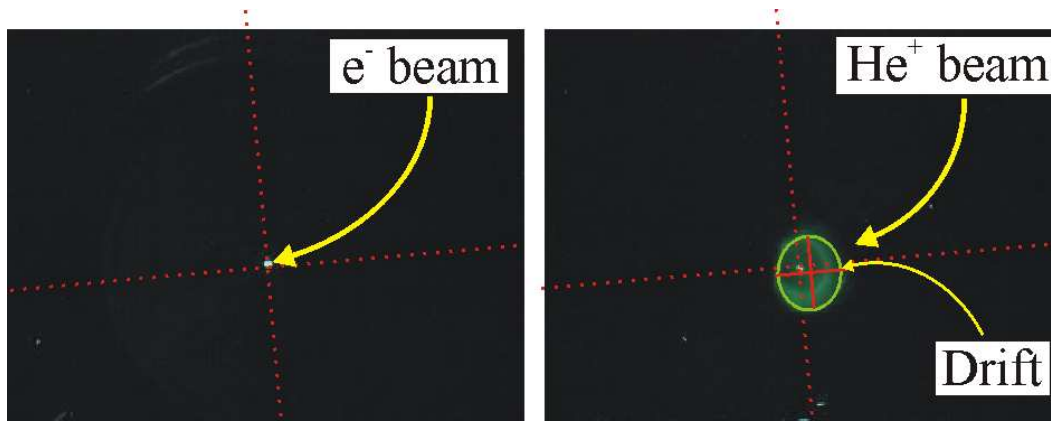


Figure 4.51: Figure on left shows spot of electron beam at  $3\text{ keV}$ , and on right shows  $He^+$  beam. A drift of  $2.8\text{ mm}$  is shown with respect to this electron spot. Axis are shown with respect to camera tilt.

The picture on the right shows the  $He^+$  beam at  $6\text{ keV}$  energy with vertical drift  $2.8\text{ mm}$  with a good comparison to the analytical value of  $3.2\text{ mm}$ . Secondary electrons are also produced by beam collision with the phosphor screen (see figure 4.52). These electrons are repelled back from screening electrode of ion source. The screening electrode is normally hold at 10% value of extraction potential. The time of flight can be estimated in the range of  $4 \times 10^{-7} - 8 \times 10^{-7}\text{ s}$ . Thus when beam energy is low and drift is significant (beam not overlapping centre), one observes a spot produced by secondary electrons. The effect of these electrons is very low on the analyzed results. On arbitrary scale the maximum pixel intensity of electron beam in picture above is 93, whereas that from ion beam is in the range of 23000. Thus intensity from these electrons is less than 1% level that of ion beam.

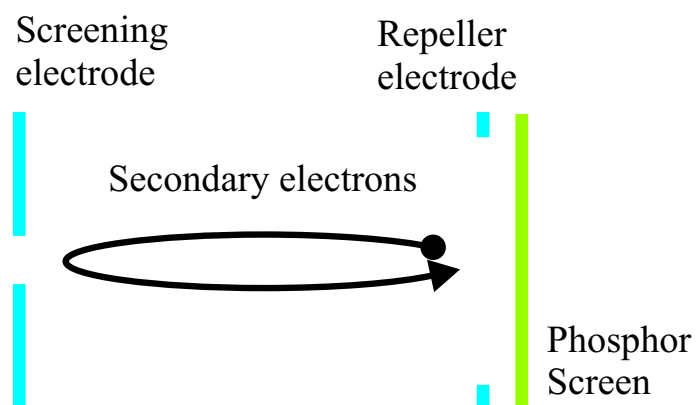


Figure 4.52: Path of secondary electrons produced on Phosphor screen.

# Chapter 5

## Injection System

The proposed storage ring with a toroidal magnetic field is to be operated with positive ion beams. These intensive ion beams should be transported into the strong magnetic field from the outside region. Issues to be dealt are reflection of injecting particles from field lines, confinement capability for higher currents and ring acceptance. Further problems like field ripple of the toroidal structure and the effect of the fields at the injection area on the circulating beam are to be addressed.

In conventional accelerator systems different injection schemes are used with fast kicker systems. A stripping mechanism is used with gas, foil or Laser stripping for  $H^-$  beam injection e.g. in SNS or ESS projects [45][46]. The kicker systems are used, to position beamlets in the desired phase-space. It may consist of bump magnets, septum magnets and/or electric fields. Multiturn systems are used to fill the phase-space of the circular machine by painting concepts with a low emittance beam from an injector linac [47][48][49][50].

Simple injection experiments with toroidal magnetic fields were investigated earlier. An inductive charging method for electrons was used in the late 1970s involving filaments[51]. A time varying magnetic field (1.5 kG) along with electric fields from space-charge produces an  $\mathbf{E} \times \mathbf{B}$  drift. This results in a drift along a radial direction towards the centre. A density of electrons up to  $4 \times 10^9 \text{ cm}^{-3}$  was achieved.

Experiments with a relativistic electron beam were carried out by Gilad at the Cornell University in magnetic fields of 1 – 4 kG [52]. A 500 keV intense electron beam produced by a Marx generator inside the ring was measured to have an injection efficiency of 60%. The main problem of heating filaments near the border of the vessel, is that the particles reach back to the injection point leading to losses. Similar effects were observed in the CNT machine, which produces an electron plasma in a stellarator configuration [53]. A retractable emitter was proposed to solve this problem.

Publications on an injection system for the PROTO-RT emphasize the possibility of injection of charged particles generated outside the trap region. The PROTO-RT consists of a toroidal vessel with a central conductor generating a poloidal magnetic field component. An electron beam with an energy of 2 keV is injected near the X-point - cross point of separatrix where the poloidal magnetic field  $B_p = 0T$  [54].

In the present scenario, magnetic field configurations were studied which represent a  $60^\circ$ -sector of the storage ring. The same space-charge routines and simulation techniques were used as those for the beam transport studies in a single

toroidal segment. In the first step, an injection scheme with simplified fields was investigated. A special coil configuration was later designed for experiments with room temperature toroidal segments. A multiturn-like scheme was simulated to investigate the two beam interaction in a longitudinal magnetic field.

## 5.1 Simplified field model

A magnetic field using a single layer toroidal coil was defined at the beginning to save numerical efforts in design studies. This model was especially used to study beam reflections from field lines and the redistribution of mechanical momenta (pitch) in the fringing fields in detail. Due to a single layer, the coupling of fields in comparison with the real structure was underestimated. The toroidal segments were separated by a distance of 500 *mm* at the beginning. Near the face of the output plane which is also the input plane for the second toroidal segment, an auxiliary magnetic field was defined. This auxiliary magnetic field produces a small region at the input into the second toroid with curved field lines (see figure 5.1). Proton beams up to 20 *keV* were simulated along the auxiliary field and the transmission to the end of the second toroid was calculated.

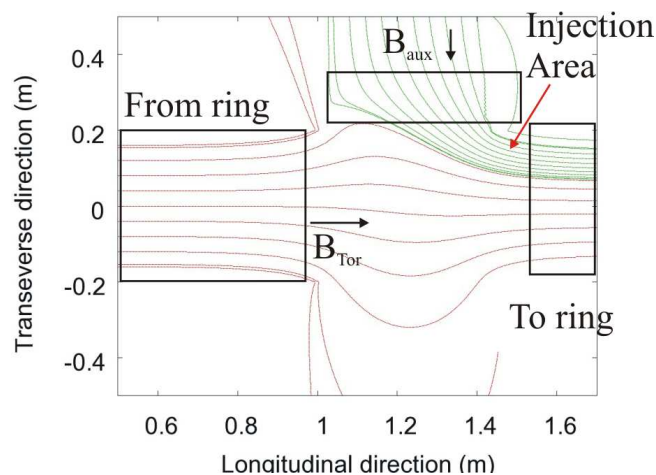


Figure 5.1: Cross sectional view of the injection scheme with simulated magnetic field lines. Proton beams were injected along the auxiliary field.

The beam energy and the toroidal magnetic field influence very much the injection efficiency. Figure 5.2(a) shows that for confined proton beams (less than 15 *keV* energy) the particle losses have a maximum around 0.5 *T* toroidal field. Whereas for the 20 *keV* case the loss rate increases linearly even at high magnetic field. This can be explained by the fact that for higher energy the time of flight in the injection section is low. Hence beam does not undergo one complete gyration and is not confined.

Figure 5.2(b) shows the auxiliary field effect for different toroidal field settings. For this case a 10 *keV* proton beam was injected. The graph shows generally the same behaviour in different toroidal field configurations. At a magnetic field of 0.15 *T* transmission is the maximum for all toroidal fields.

A useful parameter  $g$  was defined as a combination of transmission function  $T(v_\lambda)$  and output pitch angle  $\arctan(v_\lambda)$  at the output plane (see figure 5.4 ),

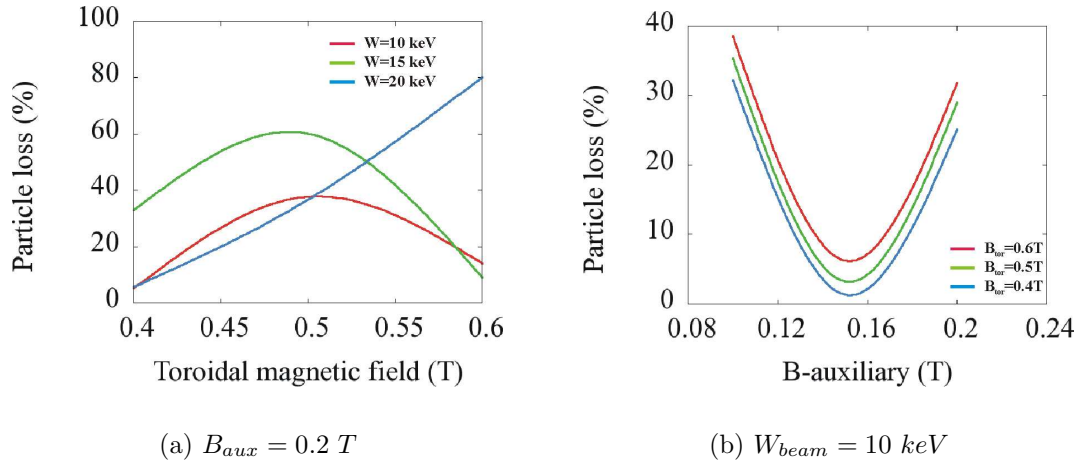


Figure 5.2: (a) Particle loss of the injected beam as a function of toroidal magnetic fields. (b) Particle loss as a function of auxiliary magnetic field.

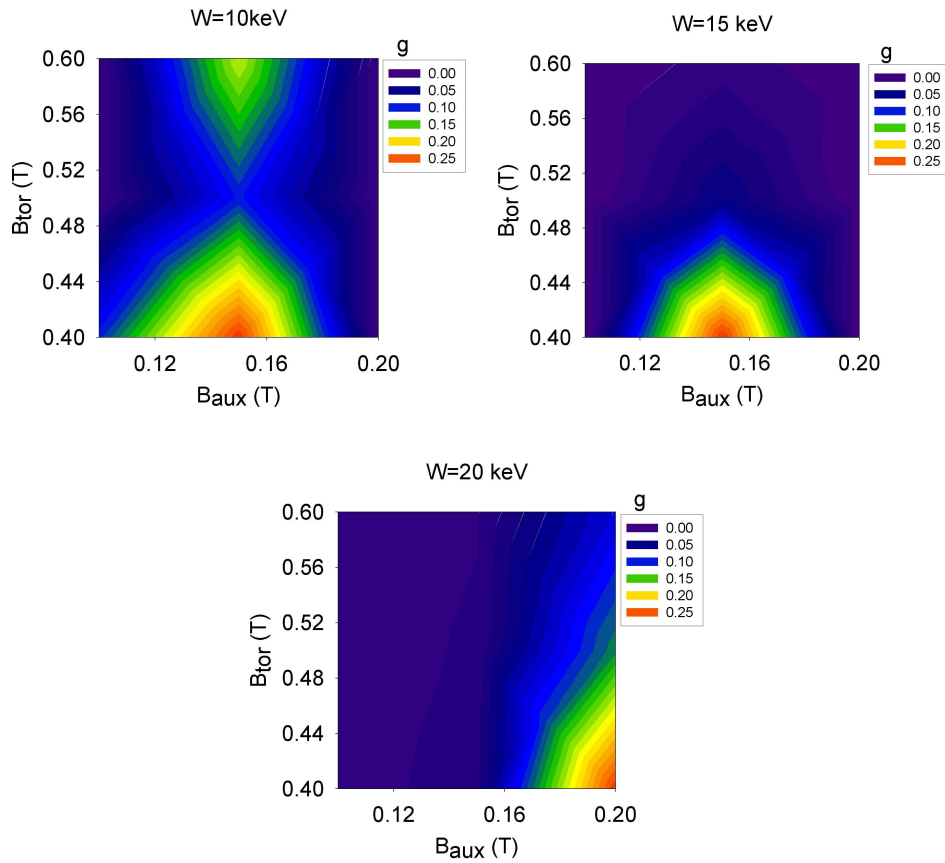


Figure 5.3: Operational parameter space for three different beam energies. The ' $g$ ' values are colour coded.

$$g = \frac{T(v_\lambda)}{\arctan(v_\lambda)}. \quad (5.1)$$

Figure 5.3 shows the operational parameter space for three different beam energies.  $g$  is plotted as a function of toroidal magnetic field ( $B_{tor}$ ) and auxiliary magnetic field ( $B_{aux}$ ).

It shows two possible operational regions (red colour) in case of the 10 keV beam energy. A first one is located at  $B_{aux} = 0.15 T$ ,  $B_{tor} = 0.4 T$  and a second at  $B_{tor} = 0.6 T$ . For 20 keV energy much higher auxiliary field is required for confinement, as seen in the graph.

## 5.2 Magnetic field design for injection experiments

From simplified model investigations, it was understood that for every configuration, there exists a solution for which the maximum transmission function can be gained for given beam parameters. In the consideration of experiments with two toroidal segments, a realistic magnetic field distribution was taken into account including fringing fields. All operational parameters were calculated with respect to the proton beam at an energy of  $10\text{ keV}$ .

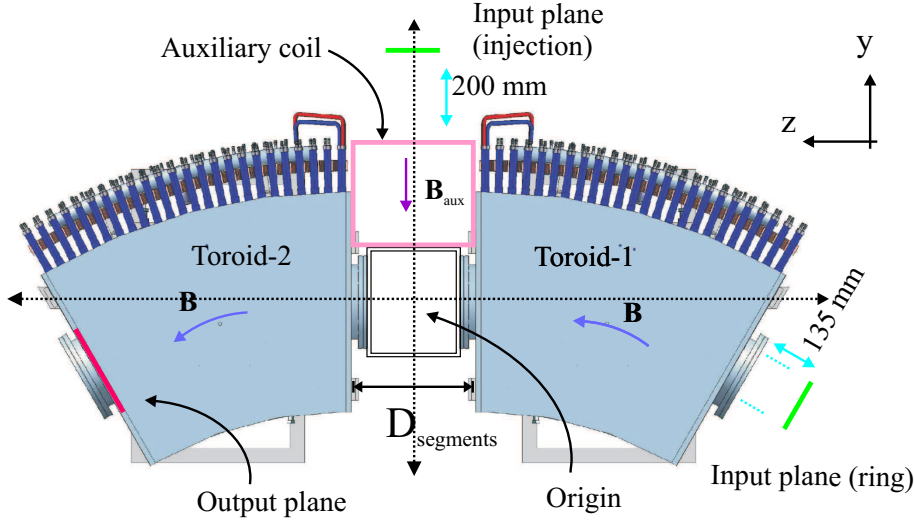


Figure 5.4: Top view of the injection system with real toroidal segments.

Figure 5.4 shows the general layout under investigation. Two beams were simulated; one representing an injected beam and another corresponds to the circulating ring beam. A large geometry and parameter space was investigated to obtain maximum injection efficiency for both beams. At the output plane, the  $v_\lambda$  value for particles is calculated which gives the guiding quality for an injected and a ring beam.

### 5.2.1 Optimization for the circulating beam

The geometry of the experimental setup was optimized with respect to the circulating beam. When this beam is transported from the first segment to the second one a magnetic field drop happens. This gives rise to a periodic magnetic ripple along the ring.

The  $v_\lambda$  for the ring beam was simulated over various distances ( $D_{segments}$ ) between two segments (see figure 5.4). Figure 5.5(a) shows  $v_\lambda$  at three different magnetic fields.

As the distance between two segments is increased the beam gains transversal momentum which leads to the higher velocity ratio at the output plane. Three curves show  $v_\lambda$  for different magnetic fields. The  $10\text{ keV}$  beam energy at the maximum magnetic field  $0.6\text{ T}$  and a distance about  $300 - 340\text{ mm}$  between two segments gives an acceptable pitch range  $v_\lambda < 0.1$ . At these settings the magnetic



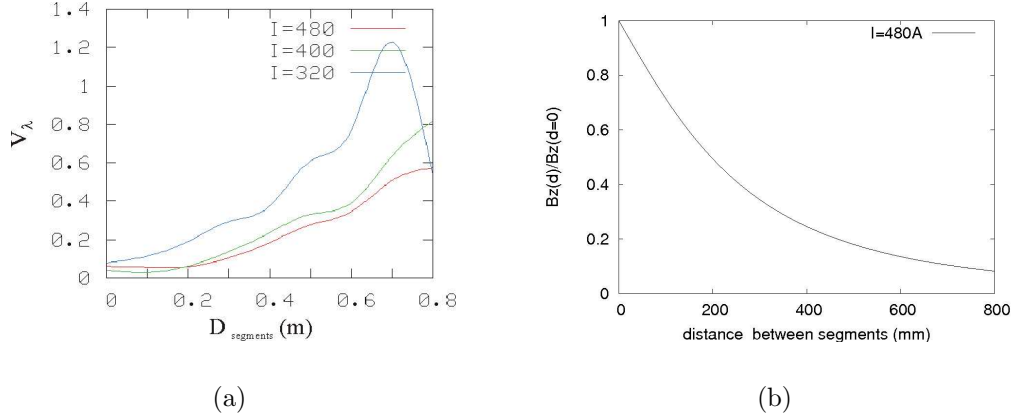


Figure 5.5: (a) Graph of  $v_\lambda$  at the output plane as a function of distance between two segments at the beam energy of  $10 \text{ keV}$ .  $480 \text{ A}$  corresponds to  $0.6 \text{ T}$  magnetic field on axis. (b) Fall of magnetic field strength at the origin as a function of  $D_{segments}$ .

field strength decreases to about  $28\% \sim 30\%$  of the maximum value (see figure 5.5(b)) which is a reasonable coupling of segment fields.

Remark: The angle between the two toroidal segments can also be varied. It provides more space for the injection coil, to be accommodated between two segments. The maximum angle (at  $D_{segments} = 300 \text{ mm}$ ) that can be chosen is  $11.5 \text{ degree}$  as toroidal segments have to be arranged on the circular path. With respect to the velocity ratio ( $v_\lambda$ ) of the ring beam this angle is limited to  $6.0 \text{ degree}$  as analysed by simulations. In the wake of technical realization this angle may be troublesome and is not investigated further.

## 5.2.2 Optimization for injection coil

A suitable magnetic field is required for a beam that can be injected under  $90^\circ$  into the toroid. As shown in the Figure 5.6 the auxiliary magnetic field will push the ring flux and introduce new field lines on which the injection beam can be inflected into the second toroidal segment. A small region (green) is generated inside the auxiliary coil which follows a curved region between the coil and second segment. Injection beam will follow this green path. Maximum transmission can be achieved when the coil configuration is optimized, as described in the following.

### Geometry of the auxiliary coil

It includes the length of the coil as well as inner and outer radii, which define the magnetic field distribution. The outer radius is ultimately limited by the distance between two segments to  $300 \text{ mm}$ . A smaller inner radius allows a higher number of coil turns. This also reduces the current required for a particular magnetic field strength. On the other hand the usable phase-space for particle injection is reduced rapidly due to the field superposition with the toroidal field. The optimum parameters are listed in the table (5.1). The maximum on axis field was  $0.29 \text{ T}$  in the auxiliary coil, so that it does not shift the ring beam into an unstable regime.

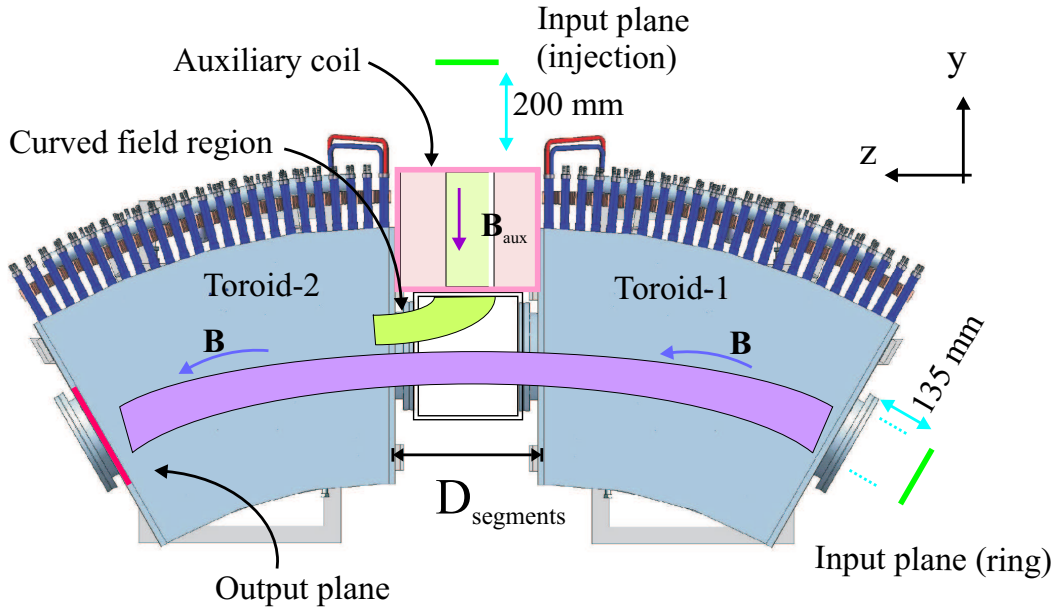


Figure 5.6: Region of interest for injection beam and ring beam.

Table 5.1: Parameters for injection coil

Quantity	Circular coil
No. of turns	40
layers	5
Inner diameter (mm)	240
Outer diameter (mm)	300
wire thickness (mm)	6.0
length (mm)	240

### Coil positioning

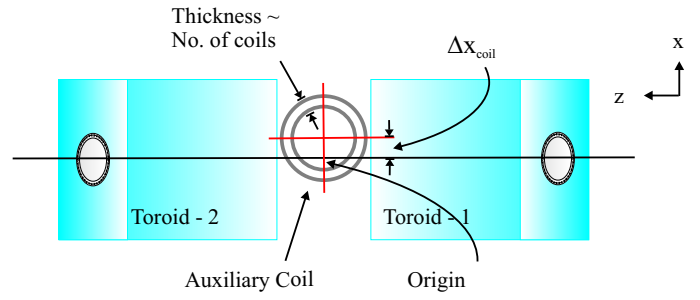
The origin  $(0, 0, 0)$  was defined in the middle of two segments. The position of the auxiliary coil can be varied in  $x - y$  plane. The  $z$ -axis position has no versatility due to the compact structure.

The  $y$ -directional positioning changes the strength of magnetic field in the curved region and determines the effect on the ring beam. The  $x$ -positioning defines the curvature of magnetic field near injection area and influences the drift of the injected beam. For the positive magnetic field, the curvature drift is downward along the  $x$ -axis. Therefore a vertical of the coil is required for drift compensation.

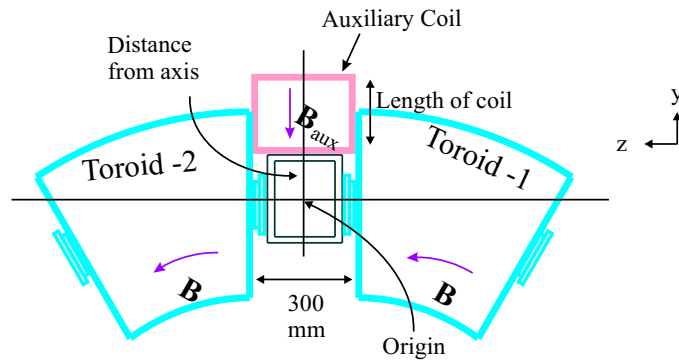
### Position of an injected beam

It was observed that the injected beam requires a proper transversal kick in the fringing field of the auxiliary coil. This kick from fields gives a required gyration phase and longitudinal momentum to the beam. For every setting there exists one solution for an injection trajectory along which  $v_\lambda$  tends to become 0. But the system acceptance largely depends upon the field configuration.

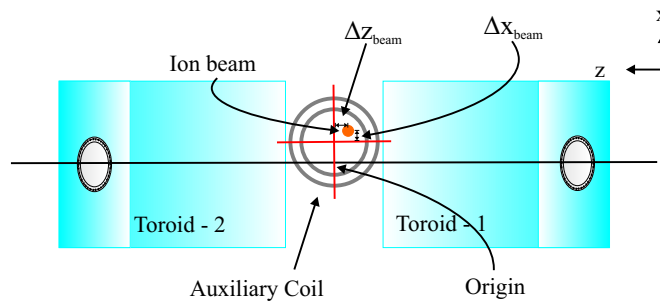
To compare effects of different factors on the beam transport,  $v_\lambda$  at the output plane was plotted as a function of the input  $x - z$  positions in colour coded maps.



(a)



(b)

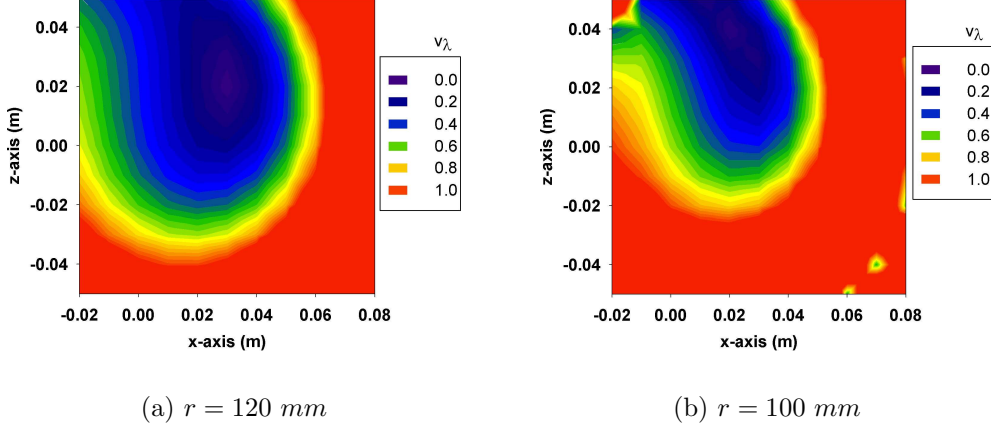


(c)

Figure 5.7: Parameter space for optimization of auxiliary field. (a) A lateral view of the injection system showing coils and its positioning in  $x - z$  plain. For simulations the toroidal field was taken right to left with auxiliary field lines coming up vertically. (b) A top view of the scheme depicting a coil length, and positioning in  $y - z$  plane. (c) The position of the injection beam. For every setting a new optimum position should be calculated using mapping technique.

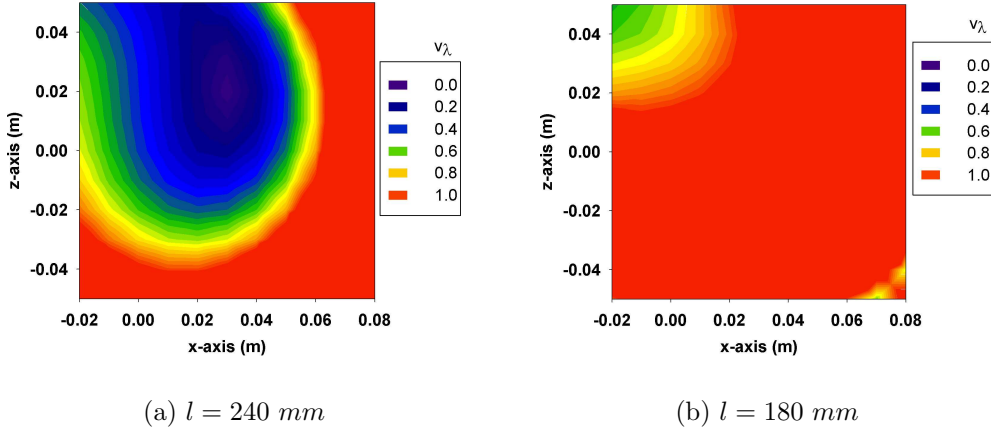
The input plane was chosen  $y = 0.2 \text{ m}$  away from the front plane of the auxiliary coil (see figure 5.4), with an injection angle perpendicular to the toroidal axis.

Figure 5.8 shows a comparison for two coil designs with different inner radii. The blue region depicts the "good beam" region. As the inner radius decreases, the "injection channel" reduces in size. One can also observe that the relative position of the "injection point", shifts upward. Hence for every setting, a different "field kick" is required for minimum  $v_\lambda$  values.




---

Figure 5.8: Colour coded velocity ratio mapped on the  $x - z$  input plane for two different inner coil **radii**. The toroidal field was set at maximum  $0.6 T$ . The auxiliary coil field level was kept constant at  $0.29 T$ ,  $l = 240 \text{ mm}$ ,  $\Delta x_{coil} = 140 \text{ mm}$ .

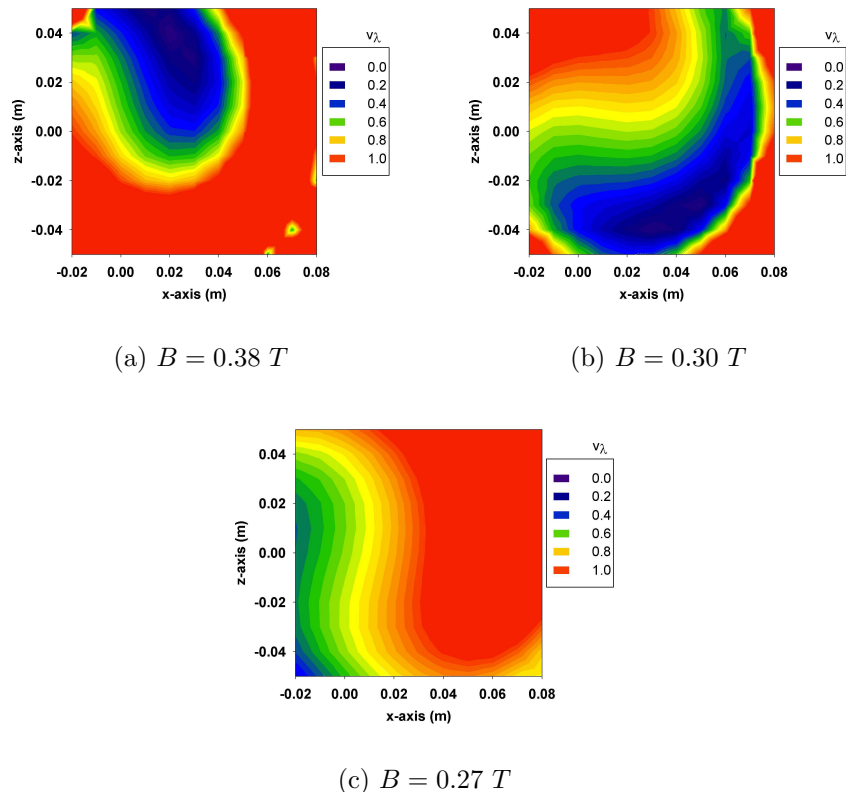



---

Figure 5.9: Colour coded velocity ratio mapped on the  $x - z$  input plane for two different coil **lengths**. The toroidal field was set at maximum  $0.6 T$ . The auxiliary coil field level was kept constant at  $0.29 T$ .  $r = 120 \text{ mm}$ ,  $\Delta x_{coil} = 140 \text{ mm}$ .

Figure 5.9 demonstrates the effect of coil length, which is coupled with the undergoing gyro phase. The phase shift and momentum transfer from ( $y$ -component to  $z$ -component) is achieved by off axis injection at the input plane. The beam undergoes about half a gyro rotation in proposed system. Hence a longer coil leads to the extra phase difference and can be gained by injecting the beam more from the periphery. This in turn reduces the space acceptance of the system at

$l = 240 \text{ mm}$ . Figure 5.9(b) shows the dark area is pushed towards the upper left corner.




---

Figure 5.10: Colour coded velocity ratio plotted as a function of position for different magnetic fields. The toroidal field was set at maximum  $0.6 \text{ T}$ . Auxiliary coil was defined inner radius  $0.1 \text{ m}$ , length  $240 \text{ mm}$  and at the position  $(x, y, z) = (0.14, 0.12, 0.0) \text{ m}$

Figure 5.10 compares the effect of the magnetic field level of auxiliary coil on the beam transport. The drift in injection channel depends on both the curvature of radius and the magnitude of magnetic field due to the  $|(\mathbf{R} \times \mathbf{B})|$  drift. As the field strength changes both the curvature drift and the required field kick change. One observes a shift in injection position and reduction in "good beam" area with respect to the decrease in magnetic field.

Figure 5.11 shows the penetration depth ( $P_d$ ) of the injected beam into the "ring acceptance" which depends on the magnetic field strength. It is defined as the distance from aperture circumference to the position where the beam hits the entrance plane of the second toroid. With higher auxiliary magnetic field the beam can be pushed deeper into the ring field region. On the other side, it also pushes the magnetic flux of the ring leading to a disturbance in the circulating beam finally. Thus, for a moderate depth  $15 \text{ mm}$ ,  $0.29 \text{ T}$  auxiliary magnetic field is required.

To get graph (5.11(b)), the beam position was varied in every setting to get a minimum  $v_\lambda$  value. The injection direction was chosen perpendicular to the toroidal axis.

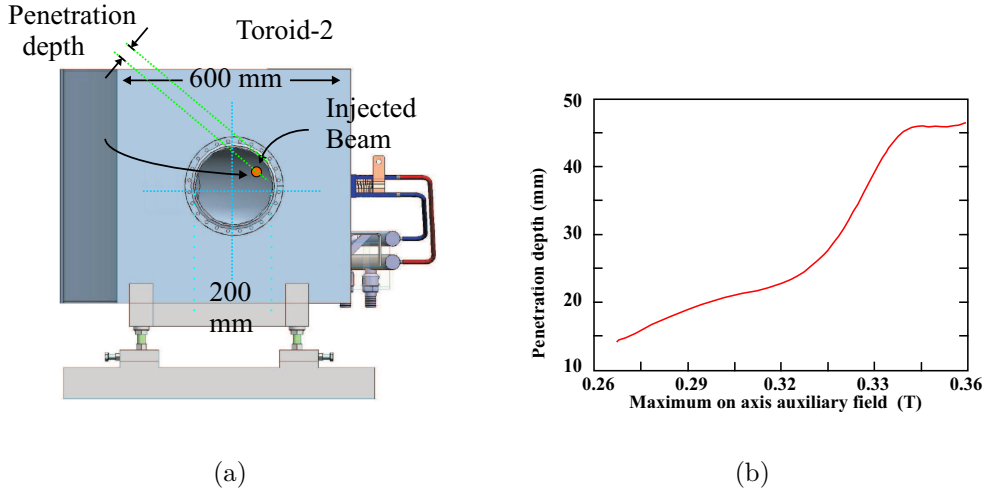


Figure 5.11: Penetration depth of the beam into the toroid aperture at different auxiliary field levels with  $B_{tor} = 0.6 T$ .

### 5.2.3 Phase-space acceptance

A thick parallel beam at  $10 keV$  energy with no divergence was injected to find the acceptance area ( $x$ - $y$ ) with respect to the  $v_\lambda$  parameter. Figure 5.12(a) shows a plot of  $v_\lambda$  at the output plane (see figure 5.4) plotted as function of particle position at the input plane. One sees, that a parallel beam with a diameter  $10 mm$  can be injected into the second segment with the "good beam" condition satisfied. Both segments were set at maximum magnetic field  $0.6 T$ .

To find the phase-space acceptance, additionally injection angles were investigated. The  $v_\lambda$  value was then plotted against input phase-space distribution. Figure 5.12(b) shows an ideal acceptance ellipse ( $x - x'$ ) plane.

### 5.2.4 Self field effect

Self fields induce a rotation around the axis in longitudinal magnetic field. Additionally, the whole beam gyrates around gyro radius when injected off axis. A complex beam behaviour is caused by the overlap of both effects.

Figure 5.13 shows the dependence of  $v_\lambda$  and of the transmission ( $T(v_\lambda)$ ) as a function of the injected beam current. The injection position and auxiliary coil settings as optimized for zero current were kept constant.

### 5.2.5 Effect of energy variation

The injection system under investigation was optimized for the beam energy of  $10 keV$ . As mentioned above an off axis injection is required. The "field kick" depends upon the canonical momentum of the beam. Therefore it is necessary to investigate injection properties with respect to energy variation.

Figure 5.14 shows a variation in  $v_\lambda$  with respect to the desired injection energy. Since time of flight is smaller for higher energies, the increase in  $v_\lambda$  at the high

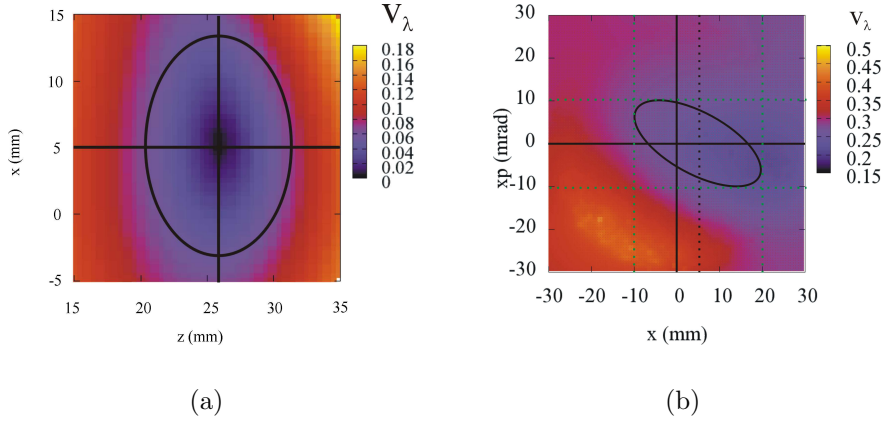


Figure 5.12: Acceptance of the injected beam for the given system. (a)  $v_\lambda$  plotted on the  $x - z$  plane, (b)  $v_\lambda$  plotted on the  $x - x'$ . The blue region is good beam region. Both plots are on different scale.

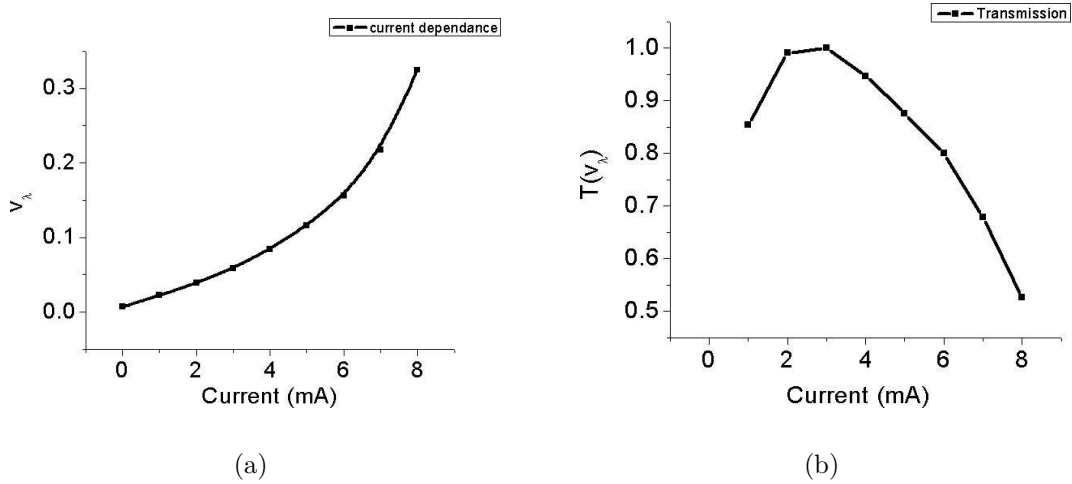


Figure 5.13: (a)  $v_\lambda$  plotted as a function of the beam current, and (b) transmission plotted as a function of the beam current.

energy end is slower compared to the low energy end. In both cases the system is mismatched, which results in higher  $v_\lambda$ -values.

The ion source to be used for experiments introduced a longitudinal energy spread of  $120 \text{ eV}$ . When compared to simulation, it becomes clear, that this source of energy spread does not much affect the  $v_\lambda$  behaviour.

## 5.2.6 Misalignment errors

In high magnetic fields, attraction and repulsion forces may disturb the mechanical stability of the system. The auxiliary coil would then experience torsional force

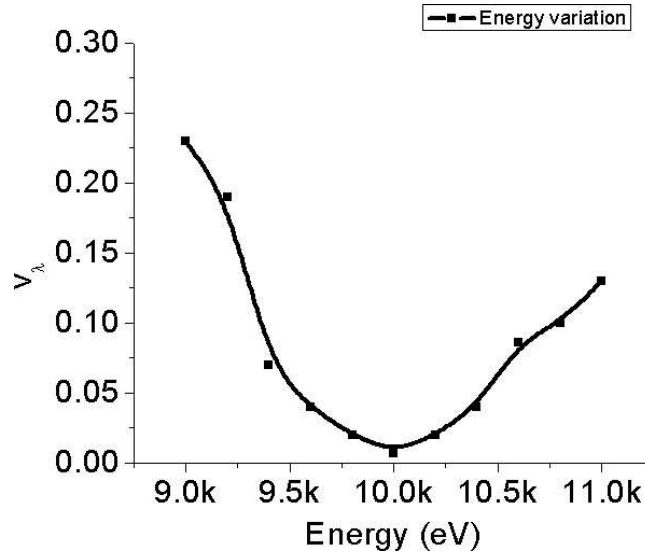


Figure 5.14: Effect on  $v_\lambda$  with changes in the beam energy. With the condition  $v_\lambda < 0.1$ , acceptable energy range of  $9.3 \text{ keV} - 10.8 \text{ keV}$  can be estimated, which is quite large against typical beam parameters.

causing errors in alignment leading to possible beam deterioration. A quality factor  $v_f$  was simulated taking into consideration such errors (see equation (3.3)).

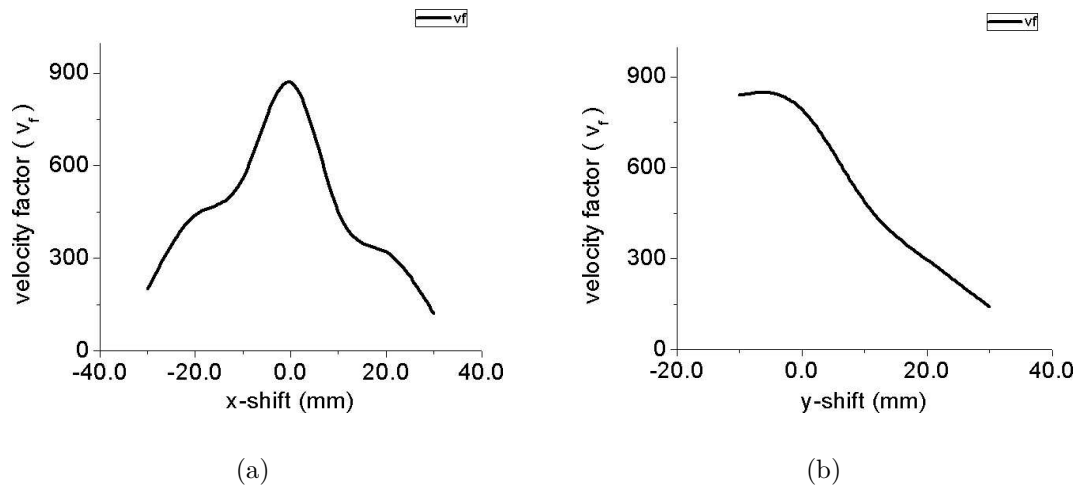


Figure 5.15: Velocity factor  $v_f$  plotted for horizontal and vertical shift in the auxiliary coil position.

The graph in Figure 5.15(a) shows  $v_f$  as a function of  $x$ -shift of the auxiliary coil and Figure 5.15(b) shows its dependence from  $y$ -shift, respectively. One observes that  $y$ -shift is more harmful. The  $v_f$  decreases to half of its maximum value over the range of one centimetre.



### 5.3 Kicker system for injection

In the context of the complete ring, the magnetic field lines form a magnetic surface. Any extra field flux from auxiliary coils will not constitute the closed ring field flux. The particles which are guided through the auxiliary coils tend to be lost on the wall. Hence a kicker system is required to force the injected particles from auxiliary field lines to the ring field lines as shown schematically in Figure 5.16(a).

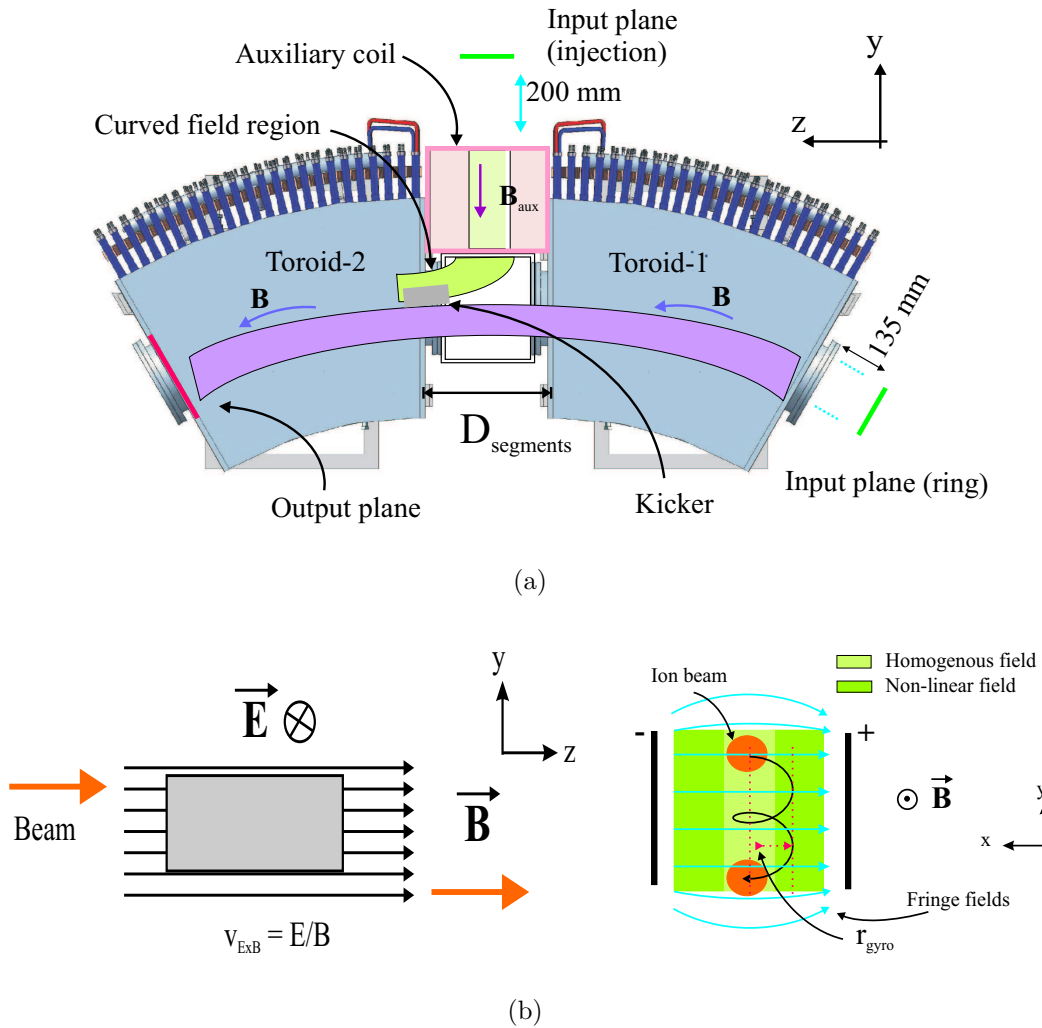


Figure 5.16: (a) A kicker system for injection to move the beam towards the ring axis, and (b) demonstration of  $\mathbf{E} \times \mathbf{B}$  force with drift motion in  $y$ -direction.

This can be achieved by forming crossed electromagnetic fields in a small region of the injected beam path. Figure 5.16(b) shows when beam passes through crossed fields, it is drifted vertically downwards. In a half gyro period beam accelerates and decelerates on helical path.

### 5.3.1 $\mathbf{E} \times \mathbf{B}$ drift

Equations (2.18-2.20) define the drift velocity in the presence of external electric field. This drift velocity is independent of particle mass and charge.

Integrating the equation of motion for a charged particle in crossed electric-magnetic fields, for  $x - y$  components we get, with  $B = B_z$

$$x = \frac{1}{\omega}(v_{x0} - \frac{E_y}{B})\sin \omega t - \frac{1}{\omega}(v_{y0} + \frac{E_x}{B})\cos \omega t + \frac{E_y t}{B} + C_3, \quad (5.2)$$

$$y = \frac{1}{\omega}(v_{x0} - \frac{E_y}{B})\cos \omega t + \frac{1}{\omega}(v_{y0} + \frac{E_x}{B})\sin \omega t - \frac{E_x t}{B} + C_4, \quad (5.3)$$

where  $C_3$  and  $C_4$  are constants. Putting initial conditions  $x(t = 0) = x_0$  and  $y(t = 0) = y_0$  we get,

$$x = x_0 + \frac{1}{\omega}(v_{x0} - \frac{E_y}{B})\sin \omega t + \frac{1}{\omega}(v_{y0} + \frac{E_x}{B})(1 - \cos \omega t) + \frac{E_y t}{B}, \quad (5.4)$$

$$y = y_0 - \frac{1}{\omega}(v_{x0} - \frac{E_y}{B})(1 - \cos \omega t) + \frac{1}{\omega}(v_{y0} + \frac{E_x}{B})\sin \omega t - \frac{E_x t}{B}. \quad (5.5)$$

Without space charge,  $E_y = 0$  and the component  $E_x$  is only from external applied electric field. Then we get for a single particle with  $v_{x0} = v_{y0} = 0$

$$v_x = \frac{E_x}{B}\sin \omega t, \quad (5.6)$$

$$v_y = \frac{E_x}{B}\cos \omega t - \frac{E_x}{B}. \quad (5.7)$$

therefore the positions are given by,

$$x = x_0 + \frac{1}{\omega}\frac{E_x}{B}(1 - \cos \omega t), \quad (5.8)$$

$$y = y_0 + \frac{1}{\omega}\frac{E_x}{B}\sin \omega t - \frac{E_x}{B}t. \quad (5.9)$$

Choosing a correct length of the plate which is directly related to the phase  $\omega t$  we can control the output velocities with an external electric field for the given magnetic field, e.g. if  $l$  is the length of plates and  $\omega t = (2n - 1)\pi$  then  $t = l/v_z$  gives,

$$l = \frac{(2n - 1)\pi v_z m}{qB}. \quad (5.10)$$

The periodic dependency of radial velocity on the plate length is shown in the Figure 5.17.

For example, a proton beam is subjected to a homogeneous longitudinal magnetic field  $B_z = 1.0 T$  and a crossed electric field  $E_x = 10 kV/cm$ , as shown in the figure 5.17 on the left. A beam with an energy of  $20 keV$  was transported along different plate-lengths. A plot of the output beam angle against plate-lengths shows a sinusoidal behavior (figure 5.17 right) as stated by equation (5.10).

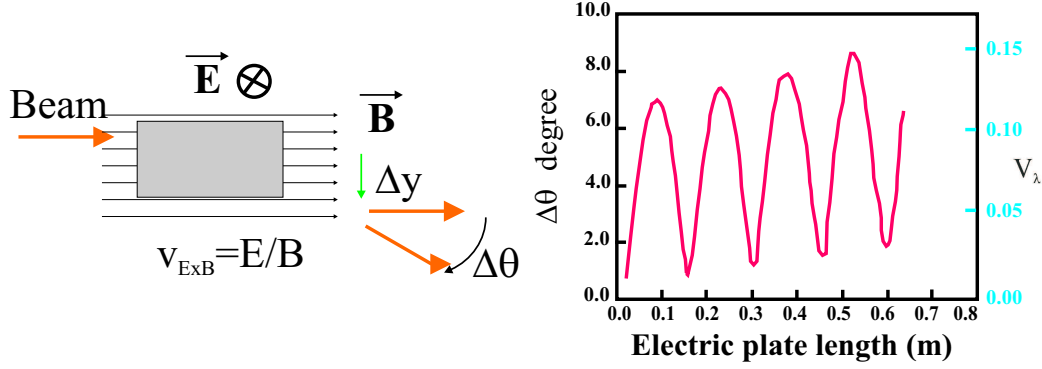


Figure 5.17: Left: At the output the beam gets a kick and rotates around  $B_z$  at an angle  $\Delta\theta$ . Right: Dependence of output pitch angle ( $\Delta\theta$ ) of the beam on the plate length, which can also be expressed by a corresponding  $v_\lambda$ .

### 5.3.2 Beam simulations in a kicker system

The properties of the kicker system were investigated with respect to the geometry, fields and beam parameters. Figure 5.18 shows the simplified scheme employed to study the kicker system. A cylindrical mesh was designed for a first investigation. A magnetic field was calculated by defining solenoidal coils, 0.5 m long, that produce a maximum on axis field of 0.6 T. Electric plates were designed with a starting point 10 cm inside of the coils. The input and output planes were defined well away to incorporate the fringing fields.

When the positive ion beam is injected, it will be accelerated transversally ( $x$ -direction) to one of the electric plates. Hence there will be a non zero transversal velocity. Due to the longitudinal magnetic field the whole beam starts to gyrate and drift in vertical  $y$ -direction. The gyro radius of the beam depends on the plate voltage. The number of gyro oscillations, the beam performs in the crossed electro-magnetic fields depends up on the energy of particles and the magnetic field. Increasing electric field levels may destroy the beam, as it drifts too near to the plates. An additional drift also is due to the fringe fields.

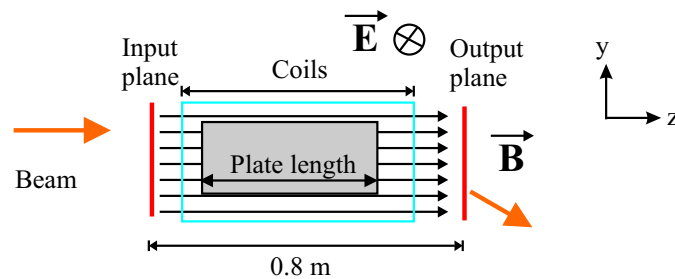


Figure 5.18: Scheme used to study the beam transport in kicker section.

A  $p$ -beam was chosen for simulations exclusively. Figure 5.19 shows the effect of the plate length on the beam. A 10 keV beam was injected into a 0.6 T magnetic

field with a plate voltage of 1000 V. Figure 5.19(a) shows linear increase in the vertical beam drift of beam as a function of the plate length.

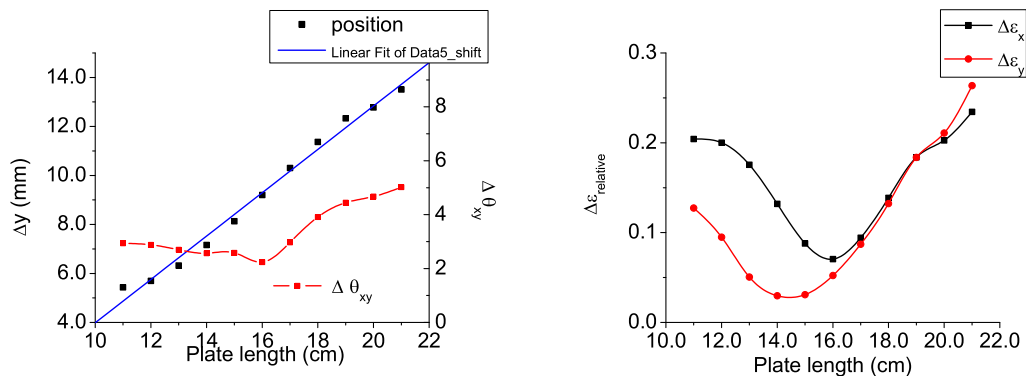


Figure 5.19: Effect of a plate length variation on the output angle (in *degree*), drift and emittances ( $E = 12.5 \text{ kV/m}$ ).

The relative change in emittance ( $\Delta \epsilon$ ) is defined as  $\Delta \epsilon = (\epsilon_{out} - \epsilon_{in})/\epsilon_{in}$ , where  $\epsilon_{in}$  and  $\epsilon_{out}$  are the emittances at input and output planes, respectively. The smallest growth is observed at the plate length between 14 – 16 mm in figure (5.19(b)).

In the next step the influence of energy variation was studied. Electric plates were held at constant potential 1000V with a length of 15 cm. The distance between both plates was kept constant at (80 mm). The beam energy varied around 10 keV. One can see in figure 5.20(a) that the vertical drift decreases as the time of flight decreases. The output angle of the beam initially decreases and then stays constant.

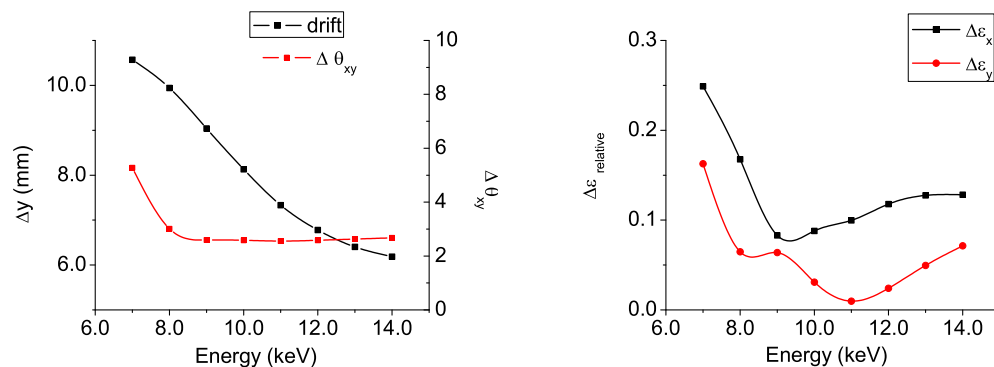


Figure 5.20: Effect of energy variation on the vertical drift and on the emittances. Potential 1000V, plate width of 80 mm and length of 150 mm were held constant.

Since  $\mathbf{v}_{\mathbf{E} \times \mathbf{B}}$  is directly proportional to the electric field, the vertical drift is a linear function of plate voltage as seen from figure 5.21(a). The term  $\mathbf{E}/\mathbf{B}$  in

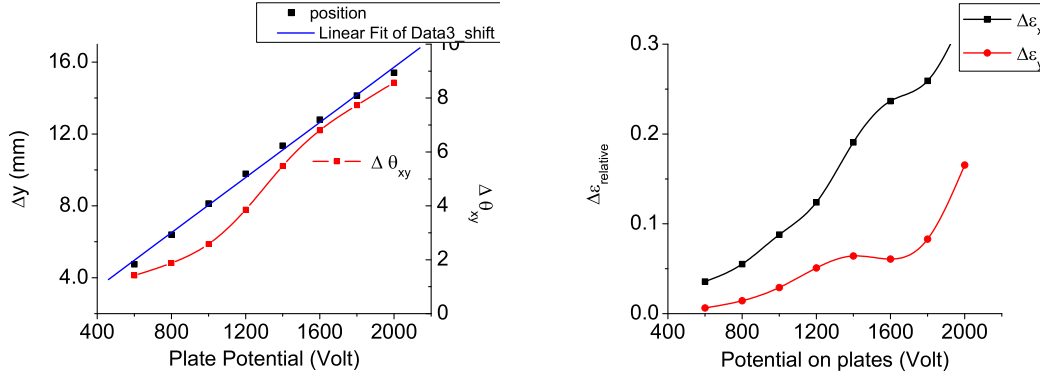


Figure 5.21: Effect of potential on the drift and output phase of the beam. Plate length of 150 mm and plate distance 80 mm were kept constant.

equations (5.4) and (5.5) implies increasing voltage also increases the gyro radius. A higher electric field accelerates particles more towards the electric plates in the transverse direction. This destroys beam quality rapidly, increasing the beam emittance as shown in figure 5.21(b). Hence a moderate field has to be applied so that the injected beam can move smoothly.

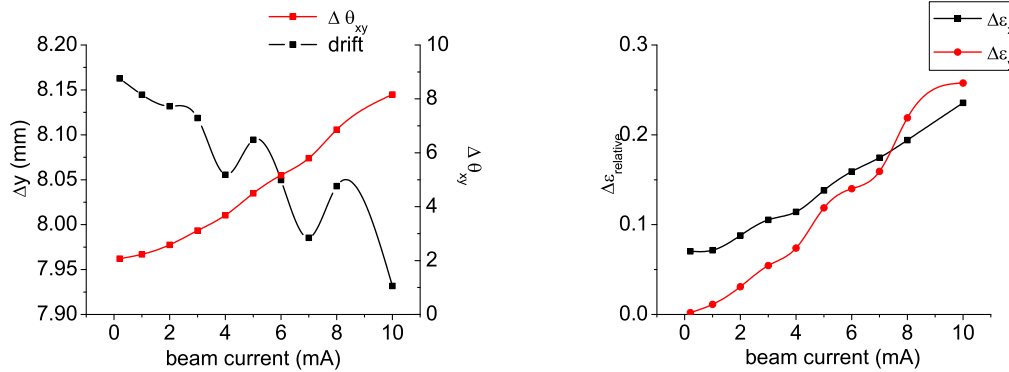


Figure 5.22: Effect of beam current on the vertical drift and the phase at output. A 10 keV proton beam was injected with plate length  $l = 150$  mm and potential  $V = 1000$  V.

Figure 5.22 shows the effect of the beam current. While the drift  $\Delta y$  is nearly independent from  $I_b$ , the output pitch angle is shifted and an emittance growth in both transverse phase space planes happens, if the conditions originally were optimized for  $I_b = 0$  A (see figure 5.22).

### 5.3.3 Effect of fringing fields on the injected beam

It is important to show the effect of the injection system (external forces) on the injected beam during many turns, especially with the consideration of electric

fringe fields. As an approximation the injected beam is considered coming back to the injection area without a rotational transform.

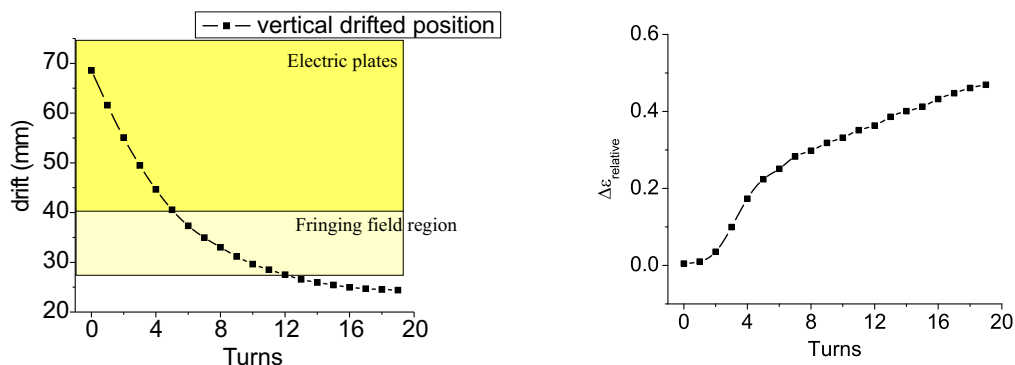


Figure 5.23: Effect of kicker plates on the ring beam. Approximately beam is shifted through  $45 \text{ mm}$  distance in vertical direction. In this case plate length was  $l = 150 \text{ mm}$  and the height was  $40 \text{ mm}$  defined with potential  $V = 1000 \text{ volt}$ .

Figure 5.23(a) shows a drifted position of the injected beam. At the input plane the beam was defined at  $y = 70 \text{ mm}$  distance from main beam axis. After first 4 turns the beam passes through fringe fields of the electric plates. Since at these positions, the gyro radius does not match with the plate length the output angle of the beam changes. The beam drifts in transverse direction towards the plates in consecutive turns. This leads to the steep increase in emittance in turn 4 – 7 mainly. Eventually the beam escapes the fringe fields and  $\Delta\epsilon$  tends to stabilize.

## 5.4 Two beam simulation

Figure 5.24 shows the possible configuration that can be used for experiments. Two toroidal segments are positioned on the circumference at a distance of  $300 \text{ mm}$  between each other. Two beams, one representing the injected beam and the other being the ring beam, were simulated. The input plane for the injected beam was chosen  $200 \text{ mm}$  outside of the auxiliary coil and that for the ring beam at  $135 \text{ mm}$  in front of the first toroid.

The configuration was designed for protons with  $10 \text{ keV}$  energy, for both beams. Electric plates with  $l = 150 \text{ mm}$  were defined at the entrance of the second toroid with a plate voltage of  $1.6 \text{ kV}$ . The toroidal magnetic field was defined at  $0.6 \text{ T}$ , and the auxiliary field at  $0.29 \text{ T}$ .

The matched condition for the ring beam was found as follows. A shifted injection position is required for optimized transmission of the ring beam. Two beams were transported through the system simultaneously with space charge forces. Figure 5.25(a) shows a phase-space distribution at the output plane. One sees two distinct blue spots indicating the good beam region. The ring beam, on average is more displaced due to vertical  $\mathbf{R} \times \mathbf{B}$  drift in the both segments. A small distortion can be seen inter beam region due to self fields.

The velocity factor  $v_f$  which is the quality factor for the whole beam in terms of  $v_\lambda$  is plotted as a function of the longitudinal arc distance in figure 5.25(b).

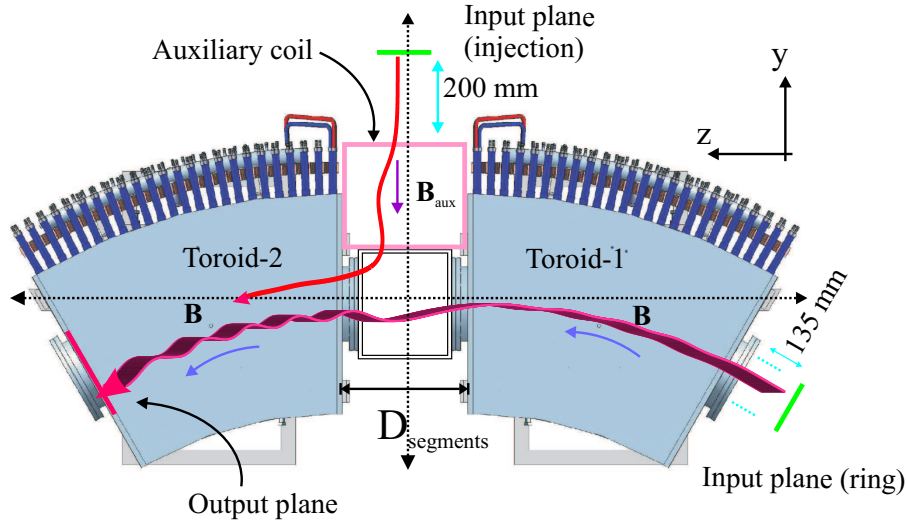


Figure 5.24: The simulation scheme for a transport along two segments. The simulated beam paths are shown in the figure. The  $x$ -axis is perpendicular to the plane of paper with direction coming out.

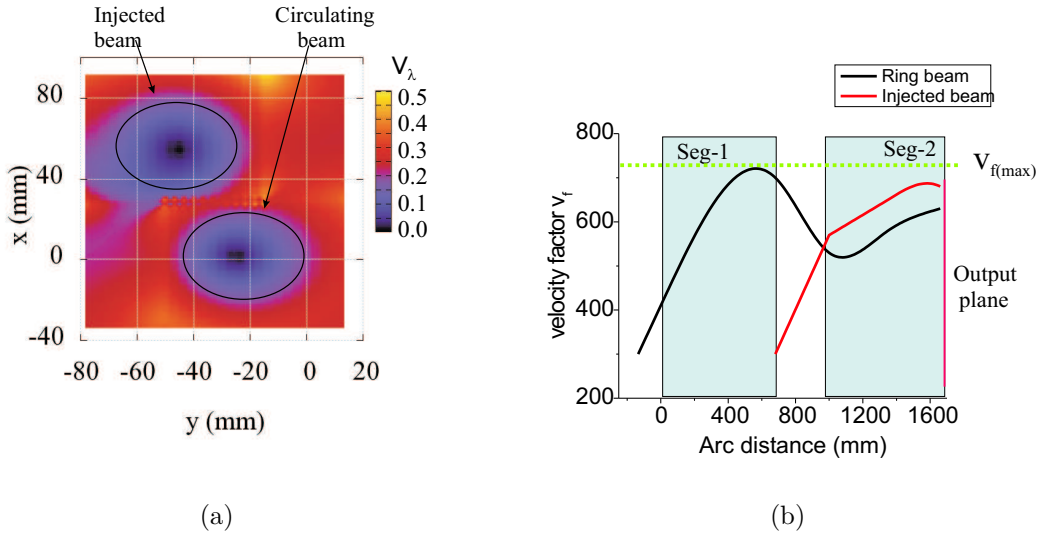


Figure 5.25: (a) Output  $x - y$  distribution for two beams with colour coded  $v_\lambda$ . (b) Velocity factor  $v_f$  (arbitrary units) plotted as a function of longitudinal arc position. Both beams have the same energy of  $W_{beam} = 10 \text{ keV}$ .

The maximum  $v_f$  that can be achieved is 720 on arbitrary scale which corresponds to the maximum transmission. At the end of the first segment  $v_f = 700$  for ring beam. The effect of external fields can be seen on ring beam decreasing the velocity factor. The velocity factor generally increases as transported in second segment.

# Chapter 6

## Conclusions

In the framework of this thesis the intense low energy ion beam transport was investigated. Especially, the beam transport in toroidal magnetic field configurations was discussed, as it may allow the accumulation of high intensive beams in the future. One of the specific tasks will be to design an injection system that can be used for the proposed low energy accumulator ring.

A simulation code (TBT) was written to describe the particle motion in curved segments. Particle in Cell techniques were utilized to simulate a multi particle dynamics. This code allows the user to generate different particle distributions as input parameter. A possibility of reading an external data file was made available so that a measured distribution can be used to compare simulation results with measured ones. A second order cloud in cell method was used to calculate charge density and in turn to solve Poissons equation. The circular toroidal coordinate system was used.

The drift motion and gyrating motion was proved to be consistent with analytical values. The single particle dynamics without space-charge simulations was proved within  $\pm 0.17\%$  error range. A parameter  $v_\lambda$  was introduced in chapter 3 to describe the guidance of a charged particle along the curved magnetic lines. Three dimensional maps were plotted to describe the beam like nature of the particle distributions under consideration. Further simulations were performed to study the self field effects on beam transport.

The experiments with single toroidal segments find niche in the work. The experiments were performed to compare the simulation results and gain practical experience. The toroidal segment has similar dimensions (major axis  $R = 1.3 m$ , minor axis  $r = 0.1 m$ , arc angle  $30^\circ$ ) as envisaged for a full scale ring design. The main difference lies in the magnetic field strength. The available segments can be operated at room temperature producing  $0.6 T$  on axis maximum magnetic field, while for the storage ring design this value is in the range of  $5 T$ .

The preparatory experiments consisted in the characterization of the ion source in a first step. Along with the momentum spectrometer and emittance scanner the beam properties were studied. Low mass ion beams  $He^+$  and mixed  $p$ ,  $H_2^+$ ,  $H_3^+$  beams were analyzed. The proton beam consisting of a 48%  $H^+$  fraction was extracted regularly and used for further experiments. A moderate beam energy of  $10 keV$  was chosen as operational energy for which  $3.08 mA$  proton beam current was measured.

In the second stage, beams were transported through a solenoid and the phase space distribution was measured as a function of the magnetic field for different beam energies. The phase-space as distributions measured in a first stage were



simulated backward and then again forward transported through the solenoid. The simulated results were then compared with the measured distribution and were within a 17% error range. The LINTRA transport program was used [57]. The phase-space distribution was further simulated for transport experiments in a toroidal magnetic field.

The experiments with a single toroidal segment give basic results necessary to compare the results between transport code and measurements. The optical diagnostic provides measurements which can be well compared with the simulated results. A digital camera with a magnetic shield was used to record images in jpeg file format. A subroutine was written to analyze a image file to give the intensity distribution of a given image file. The integrated profile in vertical and horizontal direction was used to calculate the vertical drift and the beam size. The simulated values were in good agreement with the measured ones.

The injection system needs most care. The transport program that was used to simulate the beam in the toroid was also used to design the injection system. The injection system with its special field configurations was designed to perform experiments with room temperature segments. The main point to tackle was to smoothly bring the charged particles generated outside the trap into the acceptance of the ring. The designed system consists of two sources, one representing a ring beam and the other one the injection beam. While simulations showed a clear way, how to inject the particle beam via a well positioned solenoid and in combination with a transverse electric field element causing an  $\mathbf{E} \times \mathbf{B}$  drift into the main ring acceptance, it was not yet possible to demonstrate this step experimentally with two beams in parallel. After construction of these injection elements it will be very important to measure the robustness of such a system with respect to the beam stability- especially of the injection channel.

# Appendix A

## A.1 Poisson Solver with FFT

Starting from the charge densities assigned to grid points, we want to obtain the potential and electric fields on grid points, from the Maxwell's equations. The differential equations to be solved are,

$$\mathbf{E} = -\nabla\Phi, \quad (\text{A.1})$$

or

$$\nabla\cdot\mathbf{E} = \frac{\rho}{\epsilon_0}, \quad (\text{A.2})$$

which are combined to get

$$\nabla^2\Phi = -\frac{\rho}{\epsilon_0}. \quad (\text{A.3})$$

One approach here is to solve finite difference equations using grid

$$E_j = \frac{\phi_{j-1} - \phi_{j+1}}{2\Delta x}, \quad (\text{A.4})$$

$$\frac{\phi_{j-1} - 2\phi_j + \phi_{j+1}}{(\Delta x)^2} = -\frac{\rho_j}{\epsilon_0}. \quad (\text{A.5})$$

Here one dimensional cartesian system is considered. This can be written in matrix form as

$$\mathbf{A}\phi = -\frac{(\Delta x)^2}{\epsilon_0}\rho. \quad (\text{A.6})$$

We use  $\rho_j$ 's known from  $x_j$ 's, to obtain unknown  $\phi_j$ 's and then  $E_j$ 's, for  $j$  running from 0 to  $L/\Delta x$  where  $L$  is the length of the system of  $N_G$  points. By applying boundary conditions at  $x = 0, L$  we have as many equations as unknowns; hence the problem is solvable. An approach for periodic system is to use a discrete fourier series for all grid quantities. This provides a spatial spectral information on  $\rho$ ,  $\phi$ , and  $E$  which allows smoothing over spectrum of field quantities. It is assumed that, in the problem,  $\rho(\mathbf{x})$  and  $\phi(\mathbf{x})$  have Fourier transforms,  $\rho(\mathbf{k})$  and  $\phi(\mathbf{k})$ , where  $\mathbf{k}$  is the wave vector in Fourier transform kernel,  $\exp(-i\mathbf{k}\cdot\mathbf{x})$ . This allows us to obtain  $\phi(\mathbf{k})$  from  $\rho(\mathbf{k})$  in the Poisson's differential equation directly as, in one dimension,  $\nabla^2$  is replaced by  $-k^2$ ; that is,

$$\phi(k) = \frac{\rho(k)}{\epsilon_0 k^2}. \quad (\text{A.7})$$

We then take the inverse Fourier transform of  $\phi(k)$  in order to obtain  $\phi(x)$  and then  $E(x)$ . The overall sequence is given in the figure below. The solution using a finite Fourier series starts from charge densities at the grid points, with values  $\rho(X_j)$ ,  $j = 0, 1, 2, \dots, N_G - 1$  for a total of  $N_G$  grid points. Letting the grid function  $G(X_j)$  be periodic,  $G(X_j) = G(X_j + L)$ , then the finite discrete Fourier transform is

$$G(k) = \Delta x \sum G(X_j) e^{-ikX_j}$$

with  $j$  running from 0 to  $N_G - 1$ . The inverse transform is

$$G(X_j) = \frac{1}{L} \sum G(k) e^{ikX_j}, \quad (\text{A.8})$$

sum running over  $-N_{G/2}$  to  $N_{G/2} - 1$  giving  $N_G$  a distinct value of  $G(X_j)$ . Thus with this application we can obtain the potential  $\phi(\mathbf{x})$  and electric fields  $E(\mathbf{x})$  at grid points.

### Programming with FFTW

For the purpose of simulation FFTW 3.0 library is freely available on the network. This library can be used to calculate real or odd, 1,2 or 3d transforms as per requirements. The following routine shows an example which has been used in the code for space charge calculation in cartesian coordinates.

```
#include <fftw3.h>
{
fftw_plan p;
double in[n],out[n];
p=fftw_plan_r2r_1d(n,&in[0],&out[0],FFTW_RODFT00,FFTW_ESTIMATE);
fftw_execute(p);
fftw_destroy_plan(p);
}
```

This is an example of an 1D real Fourier transform. The variable 'in[n]' can be set as  $\rho(X_j)$  and we get an output  $\rho(\mathbf{k})$  in the form of array 'out[n]'. The window has to be very carefully chosen to define boundary conditions. The real and odd function-Fourier transforms is useful for this purpose. The possibility of open boundary conditions is also available.

## A.2 Magnetic field measurements and simulation

Figure A.1 shows a schematic structure of toroidal segments. Due to the curved nature, the magnetic field along the central axis i.e. along the beam path inside was not possible to measure with a Hall probe. To compare simulations with measurements only fringing field outside the vessel was measured with the Hall probe movable along a straight line.

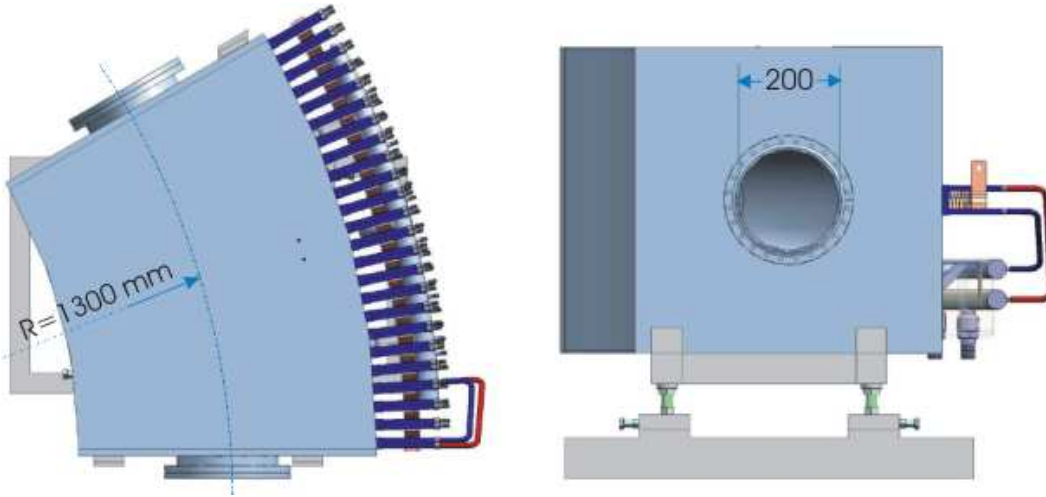


Figure A.1: Top view of the toroidal segment (on left) and lateral view on the right showing major and minor radius.

Figure A.2 shows one example of comparison between simulated and measured magnetic field. Only  $B_z$  component was measured along straight lines perpendicular to the end surface of segment, as shown in figure A.2(a). Figure A.2(b) shows a comparison for central line. A small deviation might have been caused due to an error in the angle. Hence the measured curve shows a larger deviation at the far ends. The least count error was  $0.1 \text{ mT}$ . The magnetic field simulation was estimated to be 90.4% confidence level. For these experiments low current (10 A) was used.

Figure A.3 shows a 3-dimensional plot of a magnetic field as a function of radial and a longitudinal distance. One can see, when observed carefully, the inner side has higher magnetic field than the outer. This is typical signature of curved magnetic field.

### Effect of shielding material

A solenoid was used for focussing a beam into toroidal segment (figure 4.27). The solenoid is shielded by ferromagnetic material like iron. The presence of ferromagnetic material affects the field distribution along beam line. The shielding material attracts the magnetic field lines, in accordance with the flux conservation principal. This leads to denser flux in proximity of beam line and reduction along the beam axis.

Figure A.4(a) shows the transverse component measured on the free side and material side. The material side shows lower magnetic field indicating increased

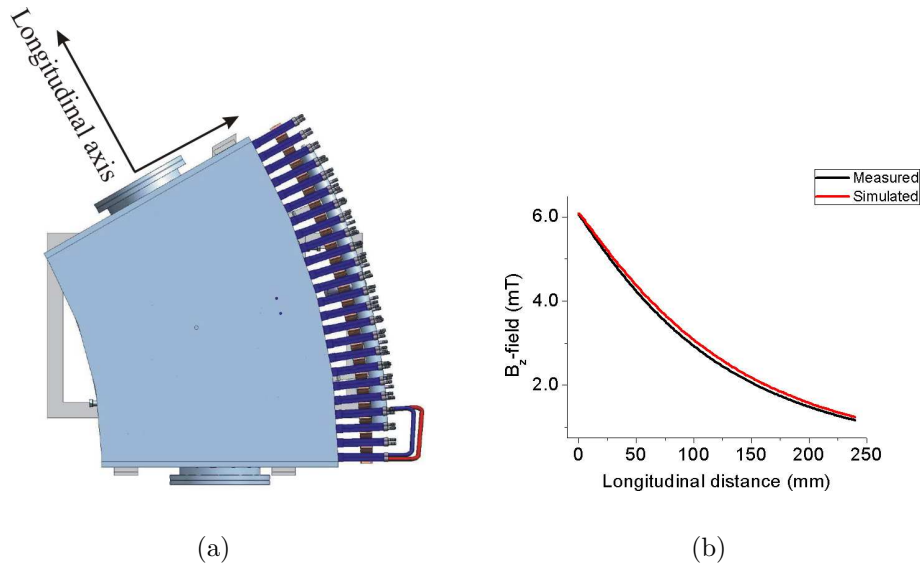


Figure A.2: Figure showing the longitudinal axis and a comparison between simulated and measured magnetic fields.

toroidal field component outside the vacuum vessel. The difference was plotted with 95% confidence limit as seen in figure A.4(b). Using CST it was simulated at maximum current of 480 A, the maximum of 0.468 T magnetic field is present on axis instead of 0.48 T.

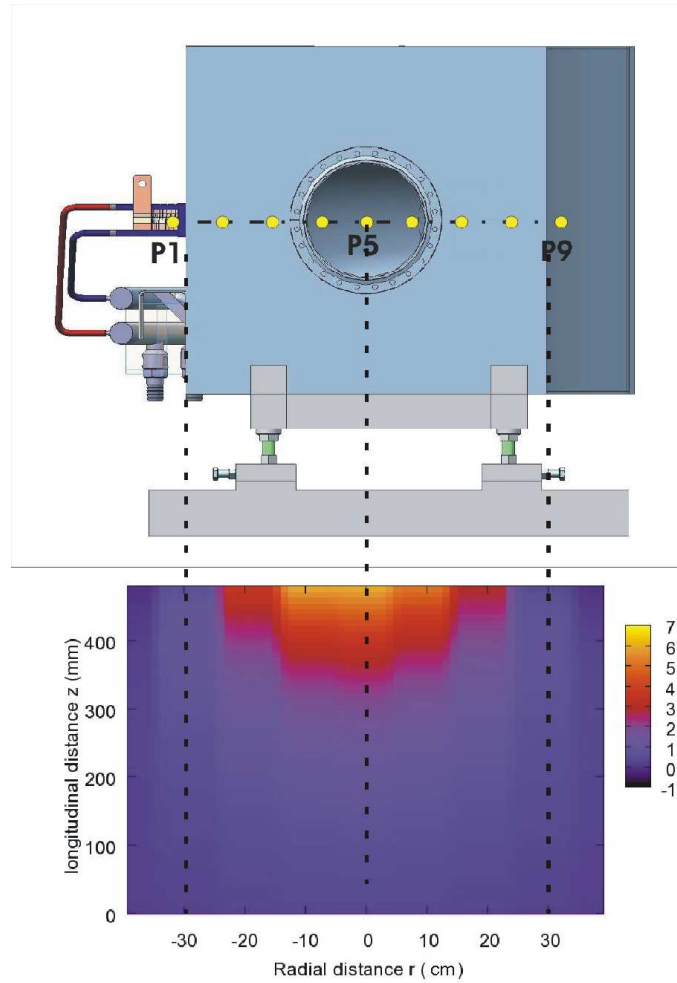


Figure A.3: Measured magnetic field (in *Gauss*) coded as a function of longitudinal and radial distance at current 10 *A*.

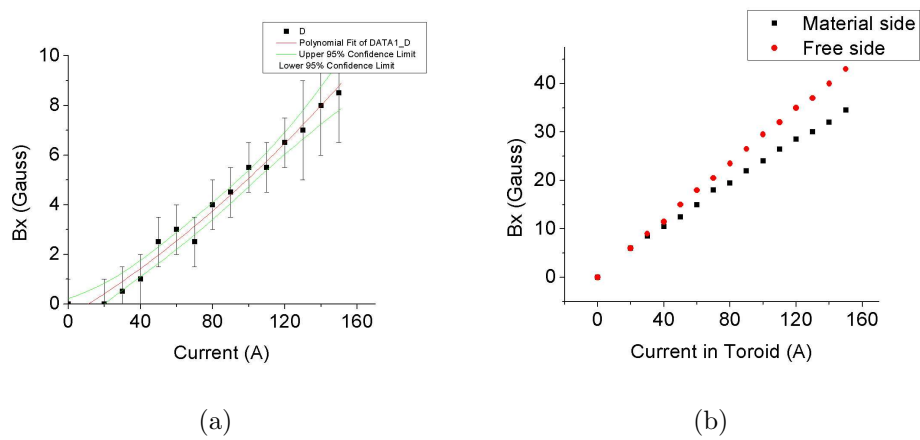


Figure A.4: Figure showing the longitudinal axis and comparison between simulated and measured magnetic field.

### A.3 Magnetic shielding of Turbo molecular pump

The ion source was mounted on a vacuum chamber which was installed with a turbo molecular pump (Pfeiffer TMU 520) at the bottom. A solenoid was mounted for focussing the beam and a toroidal magnetic segment was installed downstream. The toroidal segment was naked i.e. without magnetic shielding showing extended fringing fields. On the other hand, the solenoid is shielded with material. The functioning of the turbo pump is influenced by fringe fields. According to the user manual the maximum magnetic field of  $5\text{ mT}$  is allowed at the position of the turbo pump. In the presence of magnetic field, the eddy currents are induced in the rotor, which can be observed as increased power spent on rotating the pump. This leads to the heat generation or in the worst case damage.

In the presence of a toroidal segment only, a magnetic field of  $14\text{ mT}$  was simulated. Due to the presence of solenoid the magnetic field distribution changes at the turbo pump position. Figure A.5 shows a simulation for a magnetic field near the turbo pump region. Magnetic field due to toroidal segment was defined at maximum of  $0.6\text{ T}$ .

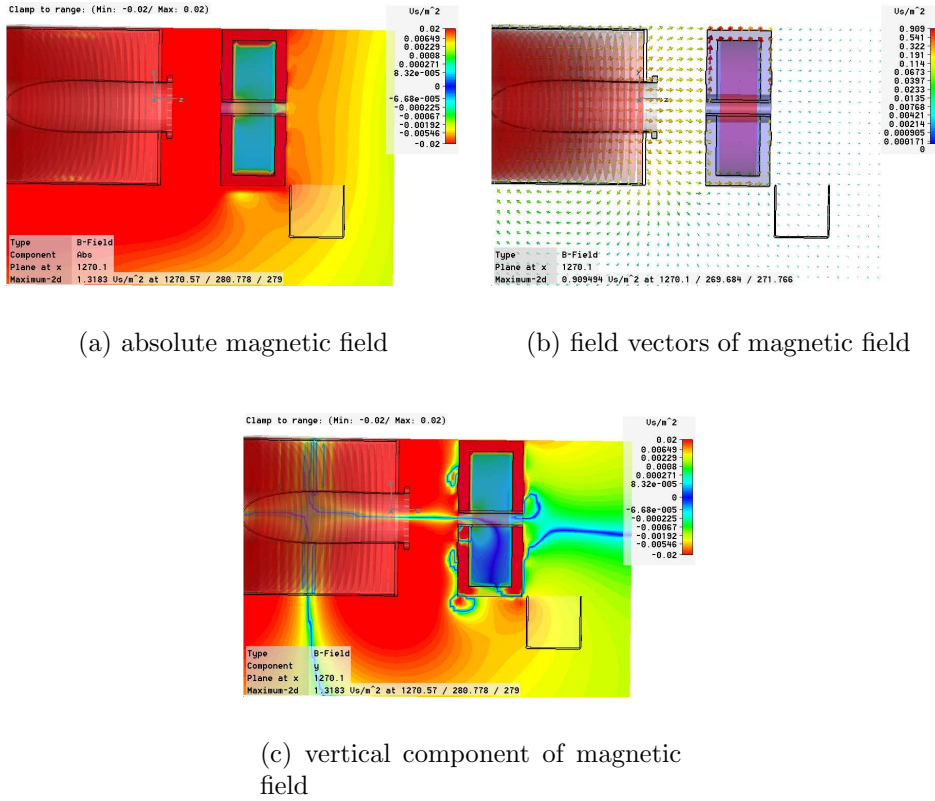


Figure A.5: Magnetic field configuration simulated at turbo pump position.

To shield the turbo pump from this magnetic field, a cylinder made of iron was simulated using CST. It was found that the iron cylinder with a base provides an effective shield than an open end cylinder. These two cases are compared in figure A.6.

For cylindrical shielding, the following formula can be applied to find the thickness of wall,

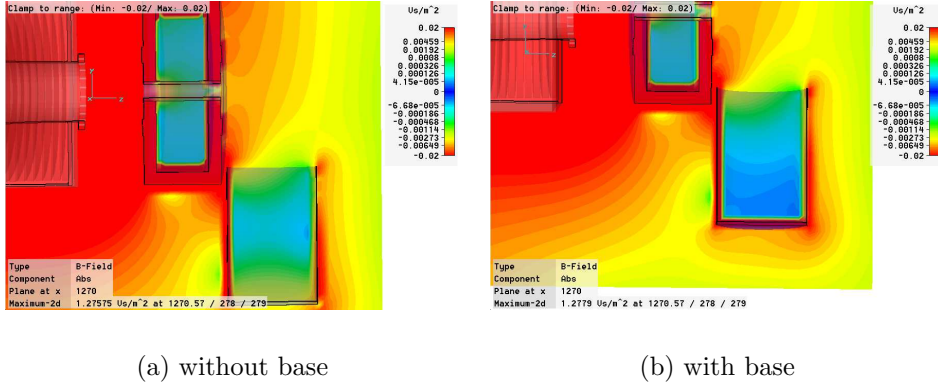


Figure A.6: Comparison of cylindrical shield without a base and with a base. Figure on the left shows symmetrical colour coded distribution in green-blue range near the centre of cylinder. Figure on the right shows more blue region, a region of lower magnetic field inside the cylinder.

$$d = D \frac{B_a}{B_s}, \quad (\text{A.9})$$

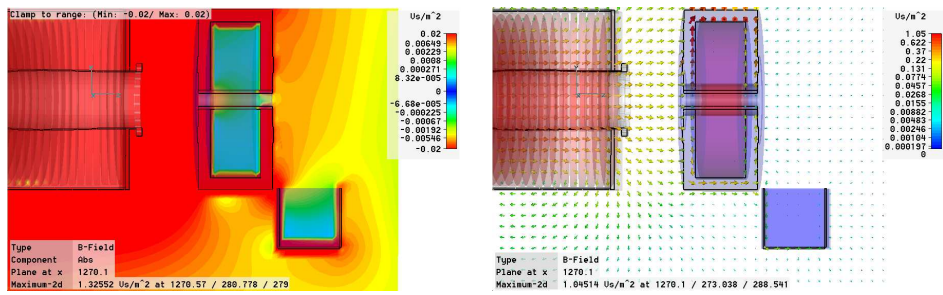
where  $d = \text{wall thickness}$ ,  $D = \text{cylinder diameter}$ ,  $B_a = \text{field to be shielded}$ ,  $B_s = \text{saturation field}$ . For 300 mm diameter, a thickness of 3 mm is required for steel (German word "baustahl" St 37) with a saturation field of 1.6 T.

For technical realization a rectangular box was designed. Figure A.7 shows the rectangular shield from iron. The magnetic field was expected to drop down to less than 1 mT at the pump position.

The shielding box had a thickness of 5 mm and a small hole in the bottom for a vacuum pipe, which has no noticeable effect on the shielding capacity.

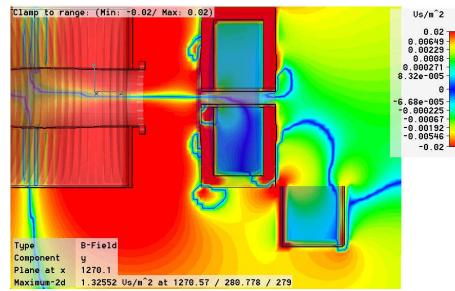
Figure A.8 compares the driver current in the turbo pump due to the toroidal magnetic field. As seen from figure, the increase in driver current in pump is noticeably lower after shielding.





(a) absolute magnetic field

(b) field vectors of magnetic field



(c) vertical component of magnetic field

Figure A.7: Magnetic field configuration simulated at turbo pump position with iron shield rectangular box.

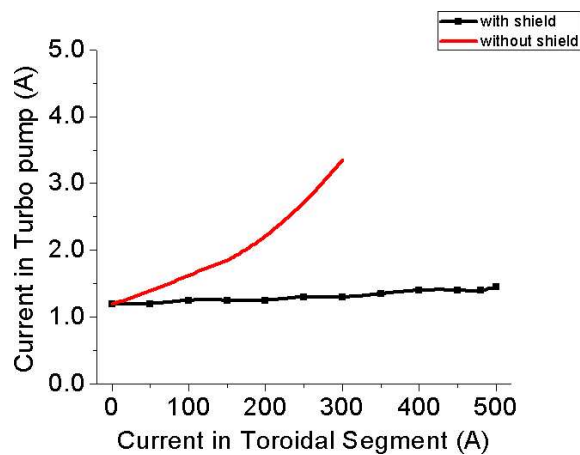


Figure A.8: Increased current in pump driver compared with shielding and without shielding box. 100 A current corresponds to 0.12 T magnetic field on axis of toroidal segment.

## A.4 Image calibration for optical measurements

For image detection from phosphor screen a digital camera was installed at a distance of  $27\text{ cm}$  from the screen. To calculate the length scale, a picture depicting parallel lines at  $5\text{ mm}$  distance was photographed with camera (figure A.9(a)). The plot shown in figure A.10(a), can be then produced by taking integral intensity in horizontal direction. One can then calculate the average distance between spikes which corresponds to  $5\text{ mm}$ . In the shown example  $1\text{ pixel}$  corresponds to  $0.3\text{ mm}$ . In the same way the vertical profiled can be taken to get average value.



Figure A.9: Photographs from the camera used for image calibration (a) for  $x - y$  pixel calibration, every line is  $5\text{ mm}$  apart in shown picture (b) to determine the centre and (c) to determine the tilt of the camera.

To determine the geometrical centre a thread with weight at one of the end was hung. And the second at horizontal position. At this intersection a black spot was photographed (figure A.9(b)). When the intensity profile is plotted, the dip in a profile plot is observed as seen in figure A.10(b). This gives the position of shifted origin.

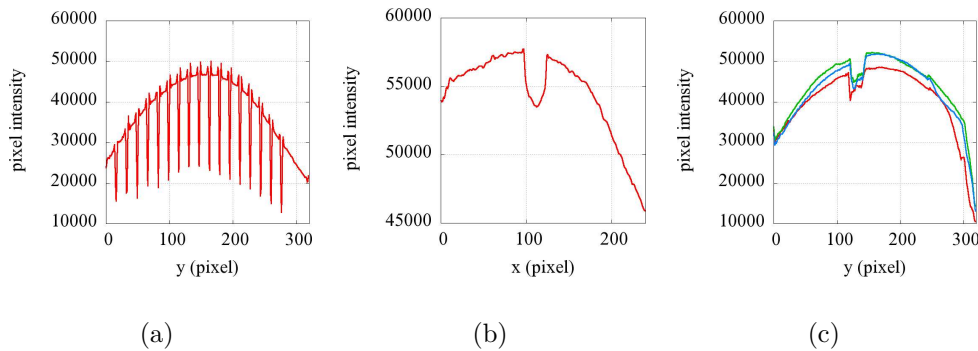


Figure A.10: (a) Integrated intensity plotted as a function of  $y$ -axis to find how many pixel corresponds to a  $\text{mm}$ , (b) integrated intensity plotted as a function of  $x$ -axis to determine centre of system, ( $y$ -axis was also plotted which is not shown here), and (c) integrated intensity plotted as a function of  $y$ -axis to find angle tilt of camera.

The tilt of the camera can be calculated by photographing horizontal lines with different angles (figure A.9(c)). The graph in figure A.10(c) shows sharp valley for red curve which corresponds  $5^\circ$  angle.

Using this information, the exact position and size of the ion beam was calculated.

## A.5 Photographs

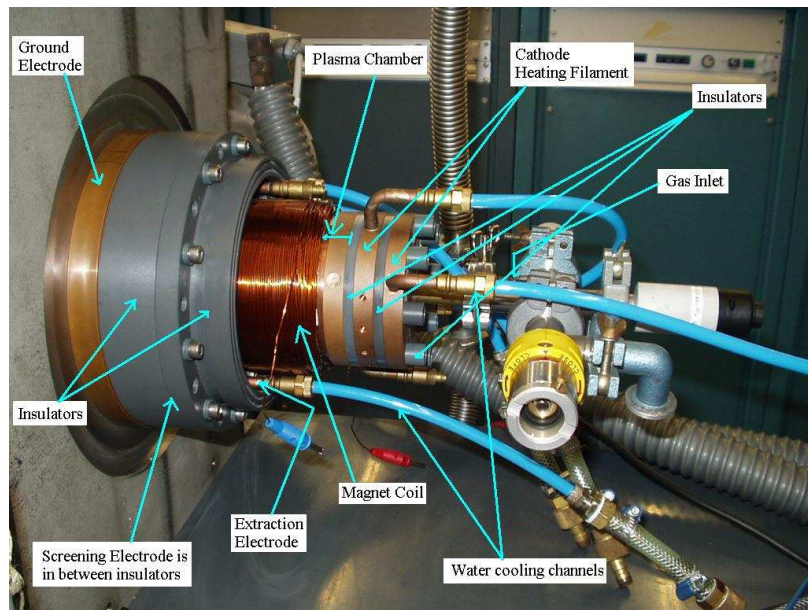


Figure A.11: Ion Source mounted on vacuum chamber.

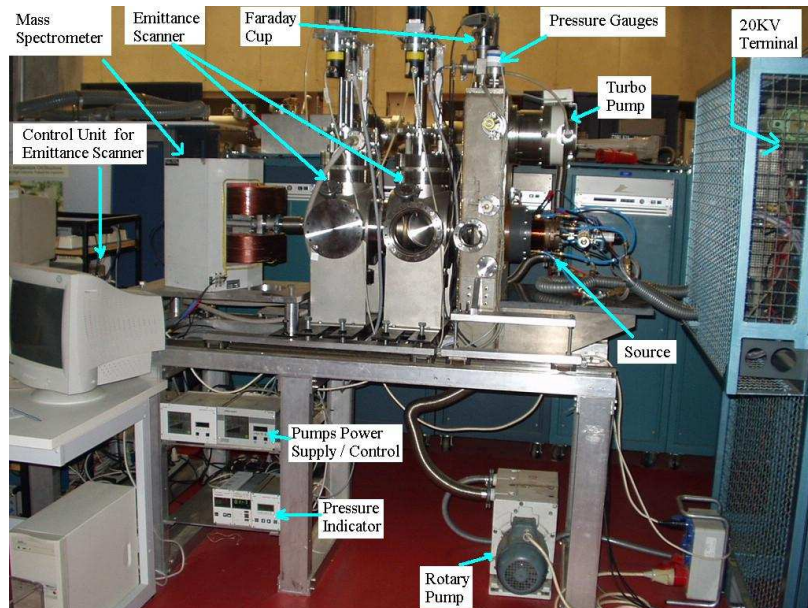


Figure A.12: Experimental setup used for characterization of ion source.

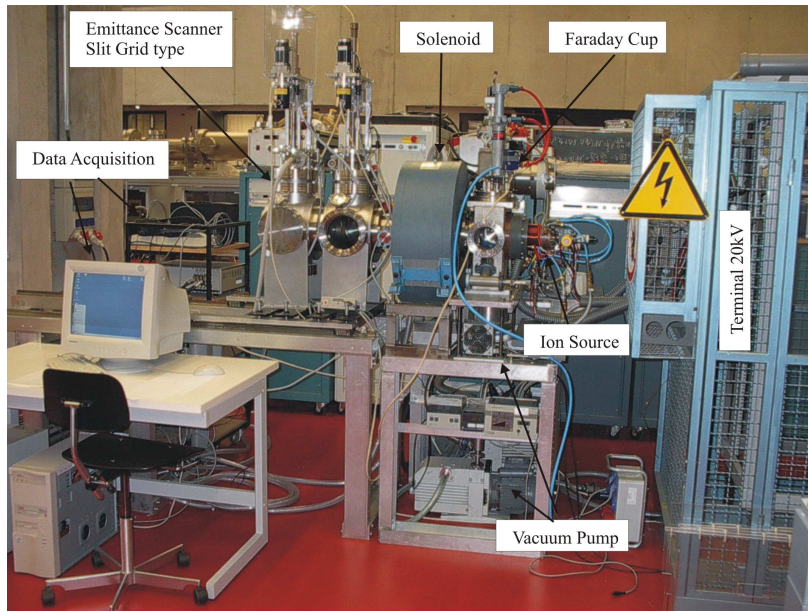


Figure A.13: Experimental setup used for transport through solenoid.

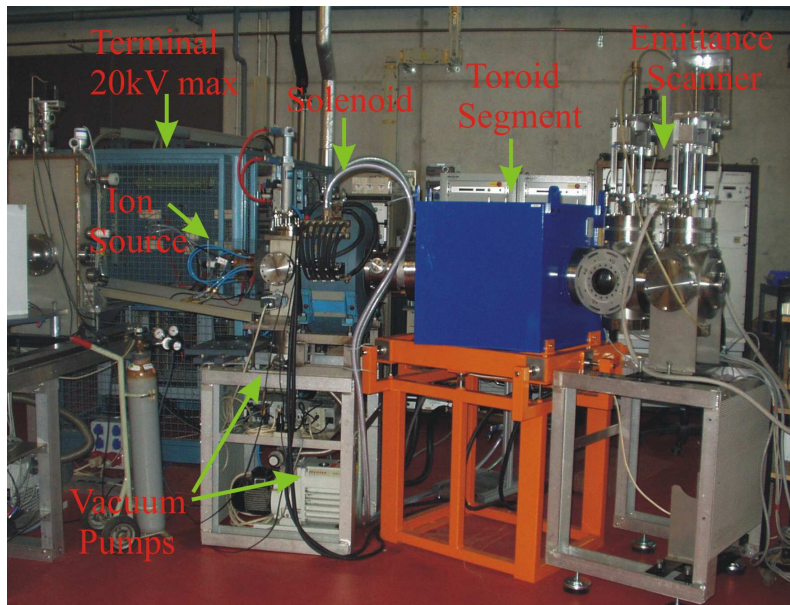


Figure A.14: Experimental setup used for transport through single toroidal segment.

# Bibliography

- [1] Martin Droba, et al. ,  
High Current Accumulator Ring,  
GSI Annual Report 2002 - HEDP.
- [2] Martin Droba, et al. ,  
High Current Ion Beams at Frankfurt University,  
Proc. EPAC04, Lucerne, p. 1198, 2004.
- [3] Lyman Spitzer,  
The stellarator concept,  
Phys. Flu., vol. 1, no. 4, 1958.
- [4] David J. Rose and Melville Clark  
Plasmas and controlled fusion,  
The MIT press 1961.
- [5] W. Bernstein, et al. ,  
Oscillations in the B-1 Stellarator,  
Phys. Flu., vol. 2, no. 6, p. 713, 1959.
- [6] W. Bernstein et al.,  
Kinematics of Ohmic Heated Plasmas in the B-1 Stellarator,  
Phys. Flu., vol. 3, no. 6, p. 1019, 1960.
- [7] W. Bernstein, et al.,  
"Runaway" electrons and cooperative phenomena in B-1 stellarator dis-  
charge,  
Phys. Flu., vol. 1, no. 5, p. 430, 1958.
- [8] Allen Boozer,  
Physics of magnetically confined plasmas,  
Rev. Mod. Phy., vol 76, p. 1071, 2004.
- [9] Allen Boozer,  
Stability of pure electron plasmas on magnetic surfaces,  
Phys. Plasmas, vol. 11, no. 10, p. 4709, 2004.
- [10] Allen Boozer,  
Density limit for electron plasmas confined by magnetic surfaces,  
Phys. Plasmas, vol. 12, 2005.
- [11] Thomas Pedersen and Allen Boozer,  
Confinement of nonneutral plasmas on magnetic surfaces,  
Phys. Rev. Lett., vol. 88, no. 20, May 2002.

- [12] T. Pedersen, et al.,  
Construction and initial operation of the Columbia Nonneutral Torus,  
Fusion Science and Technology, vol. 50, oct 2006.
- [13] T. Pedersen, et al.,  
Prospects for the creation of positron-electron plasmas in a non-neutral stellarator,  
J. Phys. B: At. Mol. and Opt. Phys. 36, 2003.
- [14] J. D. Daugherty and R. H. Levy,  
Equilibrium of electron cloud in toroidal magnetic fields,  
Phys. Fluids 10, p. 155, 1967.
- [15] Puravi Zaveri, et al.,  
Low-Aspect-Ratio toroidal equilibria of electron clouds,  
Phy Rev. Lett., vol. 68, no. 22, 1992.
- [16] S. N. Bhattacharya and K. Avinash,  
Stability of a toroidal non-neutral plasma with elongated cross-section to rigid displacements,  
Phys. Lett. A, 171, p. 367-372, 1992.
- [17] S. S. Khirwadkar, et al.,  
Steady state formation of a toroidal electron cloud,  
Phy Rev. Lett., vol. 71, no. 26, 1993.
- [18] T. M. O'Neil and R. A. Smith,  
Stability theorem for a single species plasmas in a toroidal magnetic configuration,  
Phys. Plasmas 1(8), 1994.
- [19] A. Mohri, et al.,  
Formation of a non-neutral relativistic-electron-beam ring in a toroidal magnetic field,  
Phys. Rev. Lett. vol. 34, no. 10, 1975.
- [20] H. Saitoh, et al.,  
Equilibrium of a non-neutral plasmas in a toroidal magnetic shear configuration,  
Rev. Sci. Instru., vol. 73, no. 1, 2002.
- [21] H. Saitoh, et al.,  
Stable confinement of toroidal electron plasma in an internal conductor device Prototype-Ring Trap,  
Phys. Plasmas 12, 2005.
- [22] M. R. Stoneking, et al.,  
Electron plasmas in a "partial" torus,  
Phys. Plasmas, vol. 9, no. 3, 2002.
- [23] T. Tanabe, et al.,  
Development of MUSES-ACR electron cooler,  
Proc. PAC99, New York 1999.

- [24] J. Dietrich and V. V. Parchomchuk,  
The proposed 2MeV electron cooler for COSY-JUELICH,  
Proc. EPAC06, Edinburgh 2006.
- [25] I. N. Meshkov,  
LEPTA project: generation and study of positronium in directed fluxes,  
Nuclear Instruments and Methods in Physics Research B 221, p. 168-173,  
2004.
- [26] Francis F. Chen,  
Introduction to Plasma Physics and Controlled Fusion,  
volume 1: Plasma Physics, Second Edition.
- [27] Richard Dendy,  
Plasma Physics An Introductory Course, edited.
- [28] Leon Brillouin,  
A Theorem of Larmor and Its Importance for Electrons in Magnetic  
fields,  
Phy. Rev., Vol. 67, 7 and 8, April 1945, p. 260.
- [29] R. W. Hockney and J. W. Eastwood,  
Computer Simulation Using Particles,  
Institute of Physics Publishing, Bristol and Philadelphia.
- [30] C. K. Birdsall and A. B. Langdon,  
Plasma Physics via Computer Simulations,  
Institute of Physics, Series in Plasma Physics.
- [31] R. Balescu,  
Transport Processes in Plasmas, Vol. 1 and 2  
North-Holland Publication.
- [32] Internet reference ,  
[mathworld.wolfram.com](http://mathworld.wolfram.com)
- [33] T. J. Stuchi,  
Symplectic Integrators Revisited,  
Brazilian Journal of Physics, vol. 32, no. 4, 2002, p. 958
- [34] Avinash,  
On toroidal equilibrium of non-neutral plasma,  
Phys. Flu. B 3, 1991, p. 3226,
- [35] P. Groß,  
Untersuchungen zum Emittanzwachstum intensiver Ionenstrahlen bei  
teilweiser Kompensation der Raumladung,

Dissertation zur Erlangung des Dokgrades der Naturwissenschaften  
vorgelegt beim Fachbereich Physik der Johann Wolfgang Goethe  
Universität, 2000

- [36] M. Reiser,  
Theory and Charged Particle Beams  
Wiley Series.
  
- [37] R. Hollinger,  
Entwicklung und Untersuchung einer Hochstrom-Ionenquelle zur Erzeugung intensiver, hochbillanter Protonenstrahlen,  
Dissertation zur Erlangung des Dokgrades der Naturwissenschaften  
vorgelegt beim Fachbereich Physik der Johann Wolfgang Goethe  
Universität, 2000
  
- [38] S. Humphries, Jr.,  
Charged Particle Beams,  
A Wiley-International Publication.
  
- [39] W. Bleakney,  
Ionization of hydrogen by single electron impact,  
Phys. Rev. vol. 35, May 15, 1930, p. 1180.
  
- [40] NIST online data tables,  
<http://www.nist.gov>
  
- [41] W. Bleakney,  
The Ionization of Hydrogen by single electron impact,  
Physical Review, Vol 35, p. 1180, May 15, 1930.
  
- [42] T. Morishita, et al.,  
High proton ratio plasma production in a small negative ion source,  
Review Scientific Instruments, vol 75, no.5, May 2004,p.1764-1766.
  
- [43] H. Zhang,  
Ion sources,  
Science press, Springer.
  
- [44] S. C. Leeman, et al.,  
First Measurement Results at the LEG Project's 100keV DC Gun Test  
Stand,  
Proc. EPAC06, Edinburgh 2006.
  
- [45] J. Beebe-Wang, et al.,  
Injection Carbon Stripping Foil Issues in the SNS Accumulator Ring,  
Proc. PAC01, Chicago, 2001.
  
- [46] I. Sakai, et al.,  
Laser Stripping Injection for the ESS Accumulator Ring, Proc. EPAC00,  
Vienna, 2000.



- [47] F. E. Mills, et al.,  
Multiturn Injection Techniques in the MURA 50-MeV Electron Accelerator ,  
Rev. Sci. Instr., vol. 35, no. 11, p. 1451, 1964.
- [48] G. Franchetti, I. Hofmann.  
Optimizing Multiturn Injection with Space Charge and Linear Coupling,  
Proc. EPAC00, Vienna, 2000.
- [49] T. H. Uesugi, et. al.,  
Study of Multiturn Injection at HIMAC Synchrotron, Proc. EPAC04,  
Lucerne, 2004.
- [50] I. Sakai, et al.,  
Positive-Ion Multi-turn Injection with Bi-waveform Fast Orbit-Bump Magnets, Proc. EPAC96, Sitges, Barcelona, 1996.
- [51] J. D. Daugherty, et al.,  
Experimentants on the Injection and Containment of Electron Clouds in a Toroidal Apparatus,  
Phys. Flu., vol. 12, no. 12, p. 2677, 1969.
- [52] P. Gilad, et al.,  
Injection and drift studies of high current relativistic electron beams in a toroidal-like system,  
Phys. Flu., vol. 18, no. 5, p. 607, 1975.
- [53] J. Berkery, et al.,  
A retractable electron emitter for the creation of unperturbed pure electron plasmas,  
Rev. Sci. Instru., vol. 78, 2007.
- [54] C. Nakashima, et al.,  
Injection of electron beam into a toroidal trap using chaotic orbits near magnetic null,  
Phys. Rev. E, vol. 65, 2002.
- [55] W. Clark, et al.,  
Experimentants on Electron Injection into a Toroidal Magnetic Field,  
Phys. Rev. Lett., vol. 37, no. 10, p. 592, 1976.
- [56] H. Himura, et al.,  
Experiments on Injecting Electrons Into Helical Magnetic Field Configuration,  
IEEE Transactions on Plasma Science, vol. 32, no. 2, p. 510, 2004.
- [57] J. Pozimski, O. Meusel,  
LINTRA ein Computerprogramm zur Berechnung des Strahltransportes teilkompensierter, hochperveanter Ionenstrahlen,  
GrakoNews 1/99, p. 33.

# Acknowledgements

Here I would like to express my deep gratitude towards all who helped and guided me during my doctoral thesis. I would like to thank all who offered me substantial help during these years.

I am grateful to Prof. Ratzinger for providing opportunity to do research and making available necessary funding. I would also like to thank him for entrustment on my research results.

I am grateful to Dr. Martin Droba for his full guidance during all my work years. I am grateful to Dr. Oliver Meusel for his guidance and assistance in experimental fields. I would like to thank for valuable training I received under them.

I pay my sincere gratitude to my colleagues D. Bänsch, L. P. Chau, P. Nonn, K. Schulte, R. Tiede, C. Wiesner, former colleagues G. Clemente, P. Schneider for regular handy help and providing good working environment.

I pay my sincere gratitude to Dr. Werner Noli for providing phosphor screens. The success of measurement with optical assembly can be attributed to him.

I would like to thank G. Hauser, S. Reploeg, J. Kölichhaus, W. Gass and other co-workers for support in production of the experimental component and their guidance in technical designing.

I would like to thanks Mrs. Harji for her help in administration fields.

Finally I would like to thank all the people who are directly or indirectly involved in the project work.

# List of Figures

1	Darstellung des geplanten Hochstromspeicherrings mit toroidalen segmenten. Gelb: Injektion, Grün: Experimental bereich. . . . .	ii
2	Schematische Darstellung des Injektionssystems für den geplanten Hochstromspeicherring (links) und des untersuchten Injektionsexperiments mit den zwei normalleitenden Toroidsegmenten (rechts). .	v
1.1	An example of a magnetic surface of the segmented figure-8 structure (top) and single particle trajectory (bottom). . . . .	2
2.1	Left: The generalized force and radius vector in top view. Right: The direction $\mathbf{v}_R$ of the $\mathbf{R} \times \mathbf{B}$ drift for positively charged particles. For electrons, force is in the opposite direction. . . . .	6
2.2	Vertical shift against the path length along a torus with $R_0 = 1.0 m$ at an energy of $6 keV$ . Initial $20 mm$ added for beam radius. The horizontal line represents maximum acceptable drift with respect to the vessel aperture. . . . .	6
2.3	Figure showing the difference between inner and outer radii of a torus. This results in a radial magnetic field gradient $\nabla B $ . . . . .	7
2.4	$\mathbf{E} \times \mathbf{B}$ drift for a single particle (left) and beam rotation caused by $\mathbf{E}_r$ from self field (right). . . . .	8
2.5	Figure-8 type ring showing the vertical drift compensation on either side. . . . .	10
2.6	Flow chart of a PIC scheme. . . . .	10
2.7	PIC charge distribution in cartesian. . . . .	11
2.8	Concentric circular toroidal coordinates. . . . .	13
2.9	PIC charge distribution in toroidal coordinates in 2-dimensional projection. . . . .	15
2.10	Three point scheme for discrete time evolution. . . . .	20
2.11	(a) Error due to number of grid points at constant particle number $N_p = 10000$ (b) Error due to number of particles at constant <i>gridpoints</i> = $50 \times 50 \times 50$ . . . . .	22
2.12	Time for a single time step calculation as function of particle number. . . . .	22
3.1	Scheme for simulation (left) and input phase-space distribution for mapping technique (right). . . . .	25
3.2	3-dimensional toroidal field distribution over the mesh (left) and graph of magnetic field strength in radial direction at middle plane of the segment (right). . . . .	25
3.3	Trace space (phase-space) for linear system. In this case phase space at output plane is not containing information of canonical momentum in magnetic fields. . . . .	26

3.4	Figure explaining to $v_\lambda$ factor. Both components of velocities, $v_\parallel$ and $v_\perp$ , are defined with respect to magnetic field lines at the position of particle. Hence the "guidance" property is integrated in 3-dimensional map. . . . .	26
3.5	The graph depicting "good beam" case. The figure on the right shows the ellipse definition for "good beam". . . . .	27
3.6	Explanation to histogram of $v_\lambda$ . The best case occurs when a maximum number of particles show $v_\lambda$ values below a given limit, and with an acceptable spread in $v_\lambda$ . . . . .	27
3.7	Left: Velocity ratio $v_\lambda$ as a function of energy at the toroid output plane (red curve)(see figure 3.1) with vertical position (blue) at output plane. Oscillations in curve are mainly due to gyration. Right: Vertical drift of proton beam plotted with Larmor radius as errorbars against beam velocity. . . . .	29
3.8	(a) An example of 3-dimensional particle beam (proton beam at 10 keV) transported through toroidal magnetic field of 0.6 T. Four focal points are seen along the beam path. (b) Density profile mapped on $x - z$ plane. Vertical drift of beam is indicated. (c) Density profile mapped on $y - z$ plane shows 30° arc along the beam path. . . . .	31
3.9	(a)Vertical position of the proton beam as a function of beam energy, (b) beam size in centimetre shows a dominance of a gyration motion, (c) transmission variation as function of energy, at output plane. . .	32
3.10	(a) Max. abundant $v_\lambda$ , (b) FWHM variation and (c) $v_f$ as function of energy for focused proton beam input. . . . .	32
3.11	Transmission and $v_f$ as function of ellipse angle. . . . .	33
3.12	The map of $v_\lambda$ against <b>input</b> trace space. The $x-$ axis is vertical axis. The blue region gives the acceptance for particular magnetic field, the beam energy is 10 keV. . . . .	33
3.13	Vertical drift (in mm) and transmission function (in %) as a function of toroidal magnetic field. . . . .	34
3.14	Map of $v_\lambda$ against <b>output</b> $x - y$ space. The blue region shows "good beam" at different magnetic fields with constant beam energy 10 keV. Ellipse injection angle was kept constant at 0°. . . . .	34
3.15	Simulated drift of beam (in mm), beam size (in cm) at <b>output</b> and transmission function (in %) variation as function of beam current at constant energy 10 keV and magnetic field 0.6 T. . . . .	35
3.16	Simulated drift (in mm) and beam size (in cm) as function of magnetic field for different currents. . . . .	35
3.17	Velocity factor as function of beam current at three different scales of beam current. (a) full scale, (b) (0, 10 mA) range, (c) (10, 80 mA) range, (d) (80, 160 mA) range. Parallel proton beam was injected in toroidal field of 0.6 T. . . . .	36
3.18	(a) Drift as a function of the magnetic field. Black line is the analytical curve whereas red points are simulated, (b) vertical position as function of energy for two different input phase-space. Red points are for the focused beam, whereas blue points are for the parallel beam. Magnetic field was 0.6 T. . . . .	37
4.1	Cross sectional view of the ion source. . . . .	38

4.2	Magnetic Field from coils on plasma chamber. . . . .	39
4.3	Circuit diagram and experimental test bench. . . . .	40
4.4	Top view of experimental test bench. . . . .	40
4.5	Slit and grid arrangement for emittance measurements (left). Twiss parameters and relationship with beam size and angle (right). . . .	41
4.6	(a) Graph showing the single specie of mass 4 <i>amu</i> (a shift in mass scale is due to calibration of mass 1 <i>amu</i> at 10 <i>keV</i> ), (b) Energy Spectra with energy spread $\pm 100$ <i>eV</i> , (c) the phase-space distribution measured using emittance scanner $\epsilon_{rms} = 3.94 \times 10^{-2} mm - mrad$ , and (d) beam profile along transverse direction. . . . .	42
4.7	(a) Current-Energy curve for $He^+$ beam, and (b) transmission curve showing matched case at 7 <i>keV</i> . . . . .	43
4.8	Effect of plasma <i>meniscus</i> on beam current. The concave shape in shown figure gives more current than convex. . . . .	43
4.9	(a) Beam current as a function of arc current ( $I_{arc}$ ), (b) beam current as a function of filling pressure ( $P$ ) (c) beam current as a function of arc voltage ( $V_{arc}$ ), and (d) beam current as a function of magnetic field maximum magnetic field on axis. . . . .	44
4.10	Variation of emittance and brightness as function of magnetic field showing the optimized case at 15.0 <i>mT</i> . . . . .	44
4.11	(a) Graph showing the three fractions of mass $m = 1, 2$ and 3 <i>amu</i> , (b) the phase-space distribution measured using emittance scanner $\epsilon_{rms} = 8.45 \times 10^{-2} mm - mrad$ , and (c) beam profile along radial direction. . . . .	45
4.12	Graph of relative occurrence of (a) $H^+$ , (b) $H_2^+$ , and (c) $H_3^+$ . . . . .	46
4.13	Graph of mass spectra of $H^+$ , $H_2^+$ , and $H_3^+$ at the position of island with respect to figure 4.12. Beam energy was held constant at 9.2 <i>keV</i> . . . . .	46
4.14	Graph of relative occurrence of proton fraction for different gas filling pressure at constant arc potential 80 <i>V</i> . . . . .	47
4.15	Graph of relative occurrence of proton fraction for different arc potentials at constant gas filling pressure $1.2 \times 10^{-2}$ <i>mbar</i> . . . . .	47
4.16	Schematic setup for solenoidal transport. . . . .	48
4.17	The phase-space distribution measured was transformed back till the aperture at extraction of source. And this back calculated distribution was used for forward transport through the solenoid. . . . .	49
4.18	(a) Simulated and (b) measured phase-space for $I = 150$ <i>A</i> corresponding to magnetic field of 0.3 <i>T</i> at energy of 8 <i>keV</i> beam energy. Off axis 18 <i>mrad</i> shift in output phase can be noticed. The neutral beam fraction was not simulated. (c) Overlapped distribution green is simulated and red the measured. (d) Corresponding beam envelope. . . . .	50
4.19	Beam radius and divergence dependence on energy and the plot at low energy. . . . .	51
4.20	Figure (a) shows the linear behavior of inverse beam radius as function of energy and (b) compares the measured beam radius with the simulations. Magnetic field was held constant at 0.3 <i>T</i> . . . . .	51
4.21	(a) Beam current in Faraday cup and beam size downstream of solenoid as function of arc current and (b) increased beam size as a function of beam current. Beam energy 9.2 <i>keV</i> and magnetic field of 0.3 <i>T</i> was used. . . . .	52

4.22	(a) Overlapped phase-space distribution simulated (red) and experimentally measured (green), (b) beam envelopes for different species. Red is $H^+$ , green is $H_2^+$ and blue is $H_3^+$ fraction. . . . .	52
4.23	Simulation scheme for transport through solenoid for input parameters for further experiments. . . . .	53
4.24	Beam size as a function of magnetic field for three different fractions (on left). The beam size as function of magnetic field for all fractions together. Beam energy 12 $keV$ was used. . . . .	53
4.25	Phase-space distributions 80 $cm$ downstream of solenoid showing the minima for the mixed beam. This distribution was calibrated for all energies and used further for simulation and measurements as a input distribution. Red is $H^+$ , green is $H_2^+$ and blue is $H_3^+$ fraction. The proton fraction is chopped off with respect to the scanner acceptance. . . . .	54
4.26	(a) Magnetic field distribution in between the region of solenoid and toroidal segment. It shows small effect of magnetic material of solenoid, creating valley. (b) Beam size downstream of solenoid as a function of toroidal magnetic field. The solenoidal field (0.3 $T$ ) and beam energy 12 $keV$ was constant. Only proton fraction was simulated. . . . .	54
4.27	Experimental setup for investigation of beam transport in a single toroidal segment. . . . .	55
4.28	The schematic diagram and formulae for analytical calculation. . . .	56
4.29	Analytical calculation for the beam diameter (colour-coded in metre) plotted as a function of energy and magnetic field. Blue points represent a beam waist. . . . .	57
4.30	(a) Fringe field measured and compared at 10A field (b) scaled magnetic field line which demonstrates the field lines between slit and grid of emittance scanner. . . . .	60
4.31	Grid-slit arrangement of an emittance scanner. The slit and grid moves vertically downward and cut the path of beam. The dimensions of the assembly are shown in figure. . . . .	60
4.32	Comparison between simulations and emittance scanner data. (a) input phase space distribution red $H^+$ , green $H_2^+$ , and blue $H_3^+$ fraction, (b) simulated output phase-space distribution showing halo particles, (c) measured phase-space distribution, (d) phase-distribution simulated by applying the emittance scanner limitations and encoded with velocity ratio $v_\lambda$ . In this example input parameters for the ion source were set to give negligible $H_2^+$ fraction, hence was not detected at output. . . . .	61
4.33	Beam size as a function of the magnetic field at energy 10 $keV$ (on left) and as a function of energy at a magnetic field 0.425 $T$ (on right). The arc length was about 1.2 $m$ . . . . .	62
4.34	An optical assembly: photograph showing a camera and its mounted position within an iron shielded case. Lower picture shows phosphor screen mounting along with a repeller electrode. The screen is located at an arc length of 0.886 $m$ from input plane. . . . .	63
4.35	Properties of image produced by optical assembly. . . . .	65
4.36	Experimental setup for measurements with optical assembly. The arc length was about 0.886 $m$ . . . . .	65

4.37	Results from beam measurements from Phosphor screen. Absolute vertical drift as a function of energy for two different magnetic fields.	66
4.38	Dependance of vertical drift and horizontal drift on magnetic field.	66
4.39	(a) Intensity on the Phosphor screen (colour-coded) as function of energy and magnetic field. (b) Averaged power density of the spot. These graphs can be compared with figure 4.29.	67
4.40	(a) Vertical drift (colour-coded) as a function of energy and toroidal magnetic field. (b) Horizontal drift (colour-coded) as a function of energy and toroidal magnetic field.	67
4.41	(a) Measured vertical drift (in arbitrary unit - Pixels) as function of magnetic field for with space charge (red) and without space charge (black). (b) Graph showing the difference (in arbitrary unit - Pixels) in both cases as a function of magnetic field.	68
4.42	(a) Measured beam size (in arbitrary unit - Pixels) as function of magnetic field for with space charge (red) and without space charge (black). (b) Graph showing the ratio as a function of magnetic field.	69
4.43	Figure showing simulated phase-space and measurements with emittance scanner and optical assembly.	69
4.44	The vertical $x$ -profile for intensity normalized to the peak of beam position. Red is the simulated curve, green is from the emittance scanner and blue is a measurement from an optical image. The geometric centre lies at $x = 45 \text{ mm}$	70
4.45	Figure showing measurements with phosphor screen and simulated distribution in $x - y$ plane. A typical image consist of a core with three fractions and a halo from $H^+$ particles.	70
4.46	The horizontal beam profile comparison. Green is the measured one and red is the simulated curve. The geometric centre lies at $x = 45 \text{ mm}$	71
4.47	(a) Figure showing comparison between simulated and measured vertical drift and (b) beam size comparison as a function of the magnetic field.	71
4.48	(a) Intensity as a function of solenoidal field, (b) variation of beam size as a function of solenoidal field, and (c) the vertical drift variation with solenoidal field strength.	72
4.49	(a) Intensity and (b) beam size as a function of repeller potential for beam energy $8 \text{ keV}$ .	73
4.50	Vertical drift and beam size as a function of beam current.	73
4.51	Figure on left shows spot of electron beam at $3 \text{ keV}$ , and on right shows $He^+$ beam. A drift of $2.8 \text{ mm}$ is shown with respect to this electron spot. Axis are shown with respect to camera tilt.	74
4.52	Path of secondary electrons produced on Phosphor screen.	74
5.1	Cross sectional view of the injection scheme with simulated magnetic field lines. Proton beams were injected along the auxiliary field.	76
5.2	(a) Particle loss of the injected beam as a function of toroidal magnetic fields. (b) Particle loss as a function of auxiliary magnetic field.	77
5.3	Operational parameter space for three different beam energies. The 'g' values are colour coded.	77

5.4	Top view of the injection system with real toroidal segments. . . . .	79
5.5	(a) Graph of $v_\lambda$ at the output plane as a function of distance between two segments at the beam energy of $10\text{ keV}$ . $480\text{ A}$ corresponds to $0.6\text{ T}$ magnetic field on axis. (b) Fall of magnetic field strength at the origin as a function of $D_{segments}$ . . . . .	80
5.6	Region of interest for injection beam and ring beam. . . . .	81
5.7	Parameter space for optimization of auxiliary field. (a) A lateral view of the injection system showing coils and its positioning in $x - z$ plain. For simulations the toroidal field was taken right to left with auxiliary field lines coming up vertically. (b) A top view of the scheme depicting a coil length, and positioning in $y - z$ plane. (c) The position of the injection beam. For every setting a new optimum position should be calculated using mapping technique. . . . .	82
5.8	Colour coded velocity ratio mapped on the $x - z$ input plane for two different inner coil <b>radii</b> . The toroidal field was set at maximum $0.6\text{ T}$ . The auxiliary coil field level was kept constant at $0.29\text{ T}$ , $l = 240\text{ mm}$ , $\Delta x_{coil} = 140\text{ mm}$ . . . . .	83
5.9	Colour coded velocity ratio mapped on the $x - z$ input plane for two different coil <b>lengths</b> . The toroidal field was set at maximum $0.6\text{ T}$ . The auxiliary coil field level was kept constant at $0.29\text{ T}$ . $r = 120\text{ mm}$ , $\Delta x_{coil} = 140\text{ mm}$ . . . . .	83
5.10	Colour coded velocity ratio plotted as a function of position for different magnetic fields. The toroidal field was set at maximum $0.6\text{ T}$ . Auxiliary coil was defined inner radius $0.1\text{ m}$ , length $240\text{ mm}$ and at the position $(x, y, z) = (0.14, 0.12, 0.0)\text{ m}$ . . . . .	84
5.11	Penetration depth of the beam into the toroid aperture at different auxiliary field levels with $B_{tor} = 0.6\text{ T}$ . . . . .	85
5.12	Acceptance of the injected beam for the given system. (a) $v_\lambda$ plotted on the $x - z$ plane, (b) $v_\lambda$ plotted on the $x - x'$ . The blue region is good beam region. Both plots are on different scale. . . . .	86
5.13	(a) $v_\lambda$ plotted as a function of the beam current, and (b) transmission plotted as a function of the beam current. . . . .	86
5.14	Effect on $v_\lambda$ with changes in the beam energy. With the condition $v_\lambda < 0.1$ , acceptable energy range of $9.3\text{ keV} - 10.8\text{ keV}$ can be estimated, which is quite large against typical beam parameters. . . . .	87
5.15	Velocity factor $v_f$ plotted for horizontal and vertical shift in the auxiliary coil position. . . . .	87
5.16	(a) A kicker system for injection to move the beam towards the ring axis, and (b) demonstration of $\mathbf{E} \times \mathbf{B}$ force with drift motion in $y$ -direction. . . . .	88
5.17	Left: At the output the beam gets a kick and rotates around $B_z$ at an angle $\Delta\theta$ . Right: Dependence of output pitch angle ( $\Delta\theta$ ) of the beam on the plate length, which can also be expressed by a corresponding $v_\lambda$ . . . . .	90
5.18	Scheme used to study the beam transport in kicker section. . . . .	90
5.19	Effect of a plate length variation on the output angle (in <i>degree</i> ), drift and emittances ( $E = 12.5\text{ kV/m}$ ). . . . .	91
5.20	Effect of energy variation on the vertical drift and on the emittances. Potential $1000\text{ V}$ , plate width of $80\text{ mm}$ and length of $150\text{ mm}$ were held constant. . . . .	91



5.21	Effect of potential on the drift and output phase of the beam. Plate length of 150 mm and plate distance 80 mm were kept constant. . .	92
5.22	Effect of beam current on the vertical drift and the phase at output. A 10 keV proton beam was injected with plate length $l = 150$ mm and potential $V = 1000$ V. . . . .	92
5.23	Effect of kicker plates on the ring beam. Approximately beam is shifted through 45 mm distance in vertical direction. In this case plate length was $l = 150$ mm and the height was 40 mm defined with potential $V = 1000$ volt. . . . .	93
5.24	The simulation scheme for a transport along two segments. The simulated beam paths are shown in the figure. The $x$ -axis is perpendicular to the plane of paper with direction coming out. . . . .	94
5.25	(a) Output $x - y$ distribution for two beams with colour coded $v_\lambda$ . (b) Velocity factor $v_f$ (arbitrary units) plotted as a function of longitudinal arc position. Both beams have the same energy of $W_{beam} = 10$ keV. . . . .	94
A.1	Top view of the toroidal segment (on left) and lateral view on the right showing major and minor radius. . . . .	99
A.2	Figure showing the longitudinal axis and a comparison between simulated and measured magnetic fields. . . . .	100
A.3	Measured magnetic field (in Gauss) coded as a function of longitudinal and radial distance at current 10 A. . . . .	101
A.4	Figure showing the longitudinal axis and comparison between simulated and measured magnetic field. . . . .	101
A.5	Magnetic field configuration simulated at turbo pump position. . . . .	102
A.6	Comparison of cylindrical shield without a base and with a base. Figure on the left shows symmetrical colour coded distribution in green-blue range near the centre of cylinder. Figure on the right shows more blue region, a region of lower magnetic field inside the cylinder. . . . .	103
A.7	Magnetic field configuration simulated at turbo pump position with iron shield rectangular box. . . . .	104
A.8	Increased current in pump driver compared with shielding and without shielding box. 100 A current corresponds to 0.12 T magnetic field on axis of toroidal segment. . . . .	104
A.9	Photographs from the camera used for image calibration (a) for $x - y$ pixel calibration, every line is 5 mm apart in shown picture (b) to determine the centre and (c) to determine the tilt of the camera. . . . .	105
A.10	(a) Integrated intensity plotted as a function of $y$ -axis to find how many pixel corresponds to a mm, (b) integrated intensity plotted as a function of $x$ -axis to determine centre of system, ( $y$ -axis was also plotted which is not shown here), and (c) integrated intensity plotted as a function of $y$ -axis to find angle tilt of camera. . . . .	105
A.11	Ion Source mounted on vacuum chamber. . . . .	106
A.12	Experimental setup used for characterization of ion source. . . . .	106
A.13	Experimental setup used for transport through solenoid. . . . .	107
A.14	Experimental setup used for transport through single toroidal segment. . . . .	107

# List of Tables

2.1	Beam Transport properties at low energies for 0.6 $T$ in 30° sector with $R_0 = 1.3 m$ . . . . .	9
2.2	Beam Transport properties at high energy (150 $keV$ ) for higher magnetic fields in 30° sector with $R_0 = 1.3 m$ . . . . .	9
3.1	Proton motion along the 30° toroid at 10 $keV$ beam energy . . . . .	28
3.2	Proton motion along the 30° toroid at constant magnetic field of 0.6 $T$ . . . . .	29
4.1	Physical properties of Solenoid . . . . .	48
4.2	Physical properties of Toroidal Segment . . . . .	55
4.3	Longitudinal velocities at different energies. . . . .	56
4.4	Gyro-period for different species at different magnetic fields. . . . .	57
4.5	Vertical drift at different energies for different magnetic fields, all numbers in $mm$ . . . . .	58
4.6	Number of oscillations (phase) at different energies for different magnetic fields. . . . .	59
5.1	Parameters for injection coil . . . . .	81

**Ninad Shrikrishna Joshi**

**Nationality : Indian**

Date of birth : 04 September 1980

Contact Information (Current):

Institut für Angewandte Physik

J. W. Goethe Universität

Max-von-Laue Str. 1,

Frankfurt am Main.

Email: ninad4980@rediffmail.com

joshi@iap.uni-frankfurt.de



## **Academics:**

- 1986-96            Primary Schooling (10 years)  
                         Sanmitra Mandal Vidyamandir
- 1996-98            1996-98 Junior College (2 years)  
                         Sathaye College, State of Maharashtra
- 1998-2001        Bachelor of Science (Major Physics)  
                         Sathaye College, University Mumbai
- 2001-03            Indian Institute of Technology (Bombay)  
                         *Frequency Resolved Optical Gating*  
                         Adviser: Prof. B. P. Singh  
                         Topic: Laser physics, Optics
- 2004-06            Graduiertenkolleg (GRAKO) Physik und  
                         Technik von Beschleunigern  
                         Adviser: Prof. Dr. U. Ratzinger
- Since 2007        Research fellow  
                         IAP, J. W. Goethe University  
                         Adviser: Prof. Dr. U. Ratzinger  
                         Topic: Charged Particle Beam dynamics,  
                         Accelerator Physics, Plasma Physics

## **Additional projects**

Summer Project 2002 on Non-linear dynamics

Adviser: Prof. Gangal ( University Pune)

Diploma in computer hardware 2000

1 year part time course (Jetking Computer Hardware and Networking Institute)

## Teaching Assistance:

Assistance in Practical Course during 2005-07

## Awards

State Scholarship 1991-96

Medal in mathematics external state exam

Certifications in external state examinations in Mathematics, English,  
Sanskrit during 4 years schooling

## Computer Programming:

C, C++, FORTRAN (1 semester course) OS: Linux, Windows

## Publications

- [1] Beam Simulation in Toroidal Magnetic Fields Ninad Joshi, GrakoNews 1/04, p. 20.
- [2] High Current Beam upto 150 keV at Frankfurt, A. Ushakov, M. Droba, N. Joshi, U. Ratzinger, GSI Scientific Report 2004, ACCS-OPD-12, p. 320.
- [3] Status of Accumulator Ring Simulation, M. Droba, O. Meusel, N. Joshi, U. Ratzinger, GSI Plasma annual report 2004, AC-04, p. 20.
- [4] Beam Simulation in Toroidal Magnetic Field, N. Joshi, M. Droba, U. Ratzinger, GSI Plasma annual report 2004, AC-05, p. 21.
- [5] Injection Scheme for Magnetostatic Ion Storage ring, Ninad Joshi, GrakoNews 05/06, p. 23.
- [6] Planned Installations and Experiments at Frankfurt High Current Injector, M. Droba, L. Chau, N. Joshi, O. Meusel, U. Ratzinger, M. Heil, GSI Scientific Report 2005, ACC-R+D-07, p. 137.
- [7] Design Studies on Novel Stellarator Type High Current Storage Ring, M. Droba, N. Joshi, et. al., Conference Proc EPAC 2006, p. 297-299.
- [8] Design Studies on High Current Storage Ring, CSC report 2006.
- [9] Status of Magnetostatic Ring Studies, M. Droba, N. Joshi, O. Meusel, U. Ratzinger, High Energy Density with Intense Ion and Laser Beams annual report 2006, AC-02, p. 38.
- [10] Beam Transport in Toroidal Magnetic field, N. Joshi, M. Droba, O. Meusel, U. Ratzinger, High Energy Density with Intense Ion and Laser Beams annual report 2006, AC-03, p. 39.
- [11] Status of experiments with transport in toroidal magnetic field, GSI, High Energy Density Matter report 2007.
- [12] Beam transport in toroidal magnetic field, N. Joshi, M. Droba, et. al., Conference Proc EPAC 2008.
- [13] Beam transport experiments in toroidal magnetic field, N. Joshi, et. al., High Energy Density Matter report 2008.

- [14] One nanosecond bunch compressor for intense proton beams, L. P. Chau, N. Joshi, et. al., Conference Proc EPAC 2008, p. 3578-3580.
- [15] Characterization of volume type ion source for  $p$ ,  $H_2^+$ ,  $H_3^+$  beams, N. Joshi, et. al., Nuclear Instruments and Methods in Physics, accepted in press, published online *DOI* : 10.1016/j.nima.2009.05.008.
- [16] Chopper for Intense Proton Beams at Repetition Rates up to 250  $kHz$ , C. Wiesner, N. Joshi, et. al., Conference Proc PAC 2009.